

Dissertation der Fakultät für Physik der
LUDWIG-MAXIMILIANS-UNIVERSITÄT MÜNCHEN

The role of metavinculin in molecular mechanotransduction



vorgelegt von
Carleen Kluger
aus Gräfelfing

München, den 27. Oktober 2016

Dissertation der Fakultät für Physik der
LUDWIG-MAXIMILIANS-UNIVERSITÄT MÜNCHEN

The role of metavinculin in molecular mechanotransduction



vorgelegt von
Carleen Kluger
aus Gräfelfing

München, den 27. Oktober 2016

Erstgutachter: Prof. Hermann Gaub

Zweitgutachter: Prof. Tim Liedl

Tag der mündlichen Prüfung: 07. Dezember 2016

Tag der Abgabe: 27. Oktober 2016

Zusammenfassung

Das Molekül Vinkulin überträgt mechanische Kräfte in Integrin-basierten Adhäsionsstrukturen und verbindet dadurch das Aktinzytoskelett mit Talin. Eine muskelspezifische Spleißvariante namens Metavinkulin, die sich von Vinkulin durch einen 68 Aminosäuren langen Einschub in der Schwanzdomäne unterscheidet, wurde mit Kardiomyopathien in menschlichen Patienten in Verbindung gebracht. Die Expression von Metavinkulin, kann zudem durch externe Kräfte reguliert werden.

Um die Rolle beider Isoformen bei der Kraftübertragung an Adhäsionsstrukturen zu verstehen, wurden sie mithilfe biochemischer und biophysikalischer Methoden verglichen. Hierfür wurde eine Zelllinie verwendet, die weder Vinkulin noch Metavinkulin exprimiert. Damit es möglich ist die Kräfte im Bereich von Piconewton (pN), welche über diese Proteine wirken, zu messen, wurden genetisch codierte Kraftsensoren etabliert, die auf dem Prinzip des Förster-Resonanzenergietransfers (FRET) beruhen.

Die hierfür verwendeten Linkerpeptide sind durch Einzelmolekülmethoden kalibriert und man kann das FRET-Signal in fokalen Adhäsionen lebender Zellen auswerten, indem man die Lebensdauer der beteiligten Fluorophore bestimmt. Die Ergebnisse der vorliegenden Studie zeigen, dass Metavinkulin einen Teil der Funktionen von Vinkulin übernehmen kann, es aber Unterschiede bei den mechanischen Eigenschaften gibt: in Fokalen Adhäsionen ist Metavinkulin immobilisierter als Vinkulin, es zeigt eine erhöhte Wechselwirkung mit dem Protein Talin-1 und im Mittel wirken geringere Kräfte über Metavinkulin als über Vinkulin.

Abstract

Vinculin is a force bearing molecule at integrin-mediated adhesion structures, which links the F-actin cytoskeleton to talin. A muscle specific splice isoform called metavinculin, which differs from vinculin by a 68 amino acid insert in the tail region, has been linked to cardiomyopathies in human patients and shows force-dependent expression levels.

To understand their role in regulating mechanotransduction at focal adhesions, I directly compared both isoforms in a cell line depleted of vinculin using a combination of biochemical and biophysical techniques. In order to measure the piconewton ($10^{-12}N$) (pN) forces acting across these proteins, I established a variety of genetically encoded Förster resonance energy transfer (FRET)-based tension sensors.

The linker peptides are calibrated by single molecule methods and I use fluorescence lifetime imaging microscopy (FLIM) to evaluate the fluorescence signal from focal adhesions of living cells. I find that metavinculin can compensate for the loss of vinculin but propagates mechanical forces differently: it is more immobilized in focal adhesions (FAs) as compared to vinculin, it displays stronger interaction with talin-1 and metavinculin bears lower forces per molecule.

Contents

1	Biological background	1
1.1	Motivation	1
1.2	Force transduction at cellular adhesion sites	2
1.2.1	Molecular mechanotransduction and mechanosensing	2
1.2.2	Integrin-mediated adhesions to the extracellular matrix (ECM)	2
1.2.3	The integrin-talin-actin linkage	4
1.3	Biological function of vinculin and metavinculin	5
1.3.1	Structure and regulation of vinculin and metavinculin	6
1.3.2	Major binding and interaction partners of vinculin and metavinculin	7
1.3.3	Role of vinculin and metavinculin during actin bundling and polymerization	8
1.3.4	Recruitment to FAs and regulation of force transduction	10
1.3.5	Tissue specific localization and regulation of metavinculin	10
1.3.6	Involvement of vinculin and metavinculin in physiology and disease	11
1.4	Summary of biological background	13
2	Biophysical and theoretical background	15
2.1	Genetically encoded FRET-based tension sensors	15
2.1.1	Principle of FRET measurements	16
2.2	Calibration of linker peptides	16
2.2.1	Theoretical description of linker peptides	18
2.2.2	Introduction of tension sensor modules into the protein of interest	18
2.2.3	Live cell measurements using time-correlated single photon counting (TCSPC)-FLIM	19
2.3	Mechanical manipulation of the cellular environment	21
2.3.1	Linear elasticity theory in the context of traction force microscopy (TFM) and cell stretching	21
2.3.2	Analysis of cellular traction forces	22
2.3.3	Modulation of substrate stiffness and micropatterning	22
2.3.4	Cell stretching	23

3	Aims of the thesis	25
4	Experimental Methods	27
4.1	Biochemical methods	27
4.1.1	Preparation of protein lysates for SDS-PAGE	27
4.1.2	Co-Immunoprecipitation using magnetic beads	27
4.1.3	One-dimensional SDS-PAGE and Western blotting	28
4.1.4	Purification of <i>Shigella</i> invasin (IpaA)	31
4.1.5	Production of hypotonic cell lysates	32
4.1.6	Ultracentrifugation assay for F-actin binding	32
4.2	Cell culture methods	34
4.2.1	Handling of mouse embryonic fibroblast and telomerase immortalized human myometrial cells	34
4.2.2	Generation of a clonal vinculin knockout cell line	35
4.2.3	Transient transfection of cDNA constructs using Lipofectamine	35
4.2.4	Retroviral infection using the Phoenix cell system	35
4.3	Molecular biological methods	36
4.3.1	General remarks on cloning of cDNA constructs	36
4.3.2	Protocol for normal, overlap extension and mutagenesis PCR	37
4.3.3	DNA digestion, gel electrophoresis, extraction, ligation and transformation	39
4.3.4	Cloning of vinculin and metavinculin constructs	42
4.3.5	Cloning and insertion of tension sensor constructs	42
4.4	Biophysical methods	43
4.4.1	Handling of micropatterns	43
4.4.2	Production of soft substrates for TFM	44
4.4.3	Fabrication of PDMS chambers for cell stretching	46
4.5	Microscopy methods	47
4.5.1	Characterization and spectra of used fluorophores	47
4.5.2	Preparation of dishes and handling of cells for live cell microscopy	47
4.5.3	Time-correlated single photon counting (TCSPC)-fluorescence lifetime imaging microscopy (FLIM)	48
4.5.4	Fluorescence recovery after photobleaching (FRAP) on micropatterns	48
4.5.5	Imaging of substrates for TFM	49
4.5.6	Immunofluorescence staining	50
5	Data analysis	51
5.1	Image analysis and feature extraction	51

5.1.1	Analysis of cell and focal adhesion (FA) size and shape	51
5.2	Evaluation of TCSPC-FLIM data	52
5.2.1	Set-up of import routines and data structure	52
5.2.2	Fitting of lifetime curves and definition of FRET efficiency	53
5.2.3	Analysis of FLIM data	53
5.2.4	Statistical testing and considerations of measurement errors	55
5.3	Analysis of biophysical data	56
5.3.1	Fitting of FRAP curves	56
5.3.2	Particle image velocimetry (PIV) and Fourier transform traction cy- tometry (FTTC)	57
6	Results	59
6.1	Establishment and characterization of vinculin and metavinculin expressing cell lines (vinc ^{-/-})	59
6.1.1	Stable expression of vinculin and metavinculin in vinculin knockout fibroblasts	59
6.1.2	Metavinculin localizes to FA and rescues spreading defect caused by vinculin deletion	59
6.1.3	Fluorescence recovery after photobleaching (FRAP) reveals increased stability of metavinculin in FA	63
6.2	Analysis of metavinculin interaction partners	65
6.2.1	Mass-spectrometry identifies changes in interaction with talin	65
6.2.2	Co-immunoprecipitation confirms increased affinity of metavinculin for talin	66
6.2.3	Actin binding upon activation by IpaA is similar for vinculin and metavinculin	67
6.2.4	Summary of biological characterization of cell lines	68
6.3	Establishment and characterization of FRET-based biosensor constructs in living cells	69
6.3.1	Control probes for lifetime measurements in living cells	69
6.3.2	Size and dynamics of FA is not affected by insertion of tension sensor (TS) module	71
6.3.3	Mean force across metavinculin tension sensor (MTS) is decreased on glass and elastic soft substrates (ESS)	72
6.3.4	Control measurements show functionality of TS constructs	73
6.3.5	Force across vinculin tension sensor (VTS) can be increased by addi- tional vinculin or metavinculin protein	75

6.3.6	Affinity between head and tail regulates tension across vinculin and metavinculin	76
6.3.7	Mutation of the gelsolin homology motif in the metavinculin insert increases force across MTS	77
6.3.8	Summary of tension sensor measurements	79
6.4	Probing interactions of cells with their mechanical environment	80
6.4.1	TFM of vinculin and metavinculin expressing cells	80
6.4.2	Combining TCSPC-FLIM with uniaxial cell stretching	82
7	Discussion	83
7.1	The role of vinculin and metavinculin in FAs	83
7.1.1	Generation and characterization of new vinculin knockout cells	83
7.1.2	Comparison of metavinculin localization to predictions from <i>in vitro</i> studies	83
7.1.3	Changes in metavinculin interaction partners and binding affinities	84
7.1.4	Interpreting the decreased turnover of metavinculin at FA	85
7.1.5	Influence of posttranslational modifications on metavinculin function	87
7.2	Evaluation of genetically encoded biosensors using TCSPC-FLIM	87
7.2.1	Fluorophore calibration measurements and analysis of intermolecular FRET	87
7.2.2	Measurement of FRET signal from FA of living cells	88
7.3	Factors contributing to force transduction across TS constructs	89
7.3.1	Total amount of protein and turnover rates	90
7.3.2	Association with the F-actin cytoskeleton	91
7.3.3	Effects of the head-tail interaction (HTI) on force transduction	92
7.3.4	Implications of reduced force transduction across metavinculin	92
8	Outlook	93
8.1	Future directions in the analysis of molecular biosensors	93
8.1.1	Measurements using linker peptides with different force regimes	93
8.1.2	Extending measurements to three-dimensional substrates	93
8.1.3	From whole cell analysis to force measurements at the adhesion level	94
8.2	Linking FA mechanotransduction to protein translation and alternative splicing	95
9	Summary	97
10	Supplementary Material	99
10.1	Directory of used chemicals and antibodies	99
10.1.1	Materials for biochemistry	99

10.1.2	Materials for cell culture	100
10.1.3	Materials for molecular biology	101
10.1.4	Materials and equipment used for microscopy	101
10.1.5	Materials used for biophysical experiments	103
10.2	Directory of oligonucleotides and cloned constructs	104
10.2.1	Oligonucleotides	104
10.2.2	Cloned cDNA constructs	107
11	Nomenclature of molecular mechanotransduction	109
	Abbreviations	110
	List of Tables	115
	Bibliography	118

1 Biological background

1.1 Motivation

Mechanical forces and even their absence shape the human body: extensive physical exercise leads to muscle hypertrophy while exposure to zero-gravity results in muscle atrophy and osteoporosis. While bodybuilders or astronauts consciously expose themselves to extreme mechanical loads, many patients suffer from diseases caused by defective responses of their body to normal mechanical stimuli [1]. One prominent example are heart diseases, e.g. dilative and hypertrophic cardiomyopathies [2], which can result from defective mechanotransduction across the integrin-talin-vinculin linkage [3].

Here, I present a study which analyzes the role of the focal adhesion (FA) protein vinculin and its muscle specific splice variant metavinculin. Mutations in metavinculin [4-7] and alterations of the vinculin or metavinculin expression levels [8, 9] have been linked to cardiomyopathies in human patients.

Recently, Förster resonance energy transfer (FRET)-based genetically engineered biosensors made it possible to directly measure forces in the piconewton ($10^{-12}N$) (pN) range across these proteins in living cells [10]. The study presented here combines these so-called tension sensors with traction force microscopy (TFM), ultracentrifugation assays, cell stretching, micropatterning, fluorescence recovery after photobleaching (FRAP), and biochemical analysis methods, like mass spectrometry or Western blotting, to describe differences between vinculin and metavinculin and unravel their role in mechanotransduction at integrin-based adhesions.

1.2 Force transduction at cellular adhesion sites

1.2.1 Molecular mechanotransduction and mechanosensing

Cells can convert mechanical stimuli into biochemical signals to regulate e.g. adhesion, migration, proliferation and differentiation [11]. Examples for such stimuli include substrate rigidity, shear flow, gravitational pressure or contractile forces [12]. While concepts from physics such as elasticity, strain, viscosity, shear stress, and tension are well-defined, the nomenclature of mechanobiology is ambiguous. Vocabulary like sensing, feeling or touching, which originally refers to processes of the mammalian somatosensory system, is often used to describe mechanotransductive processes in non-neuronal cells. To enable in-depth discussion some central terms will be clarified in the appendix (section 11), for further reading please refer to [13–16].

Mechanotransductive processes range over multiple time-scales from seconds to weeks or even years and occur on the molecular, single-cell as well as on tissue level (Fig. 1.3 B). Compared to the speed of purely biochemical signaling which is limited by diffusion rates, mechanotransduction enables rapid (< 0.3 s) propagation of signals, e.g. activation of the kinase Src, across the pre-stressed cytoskeleton [17]. Early observations indicated that the composition of the extracellular matrix (ECM) can regulate gene expression [18] and later it was demonstrated that substrate rigidity can drive stem cell lineage differentiation [19].

One major goal of mechanobiology is to identify mechanosensors which change their conformation, binding affinities or post-translational modification (e.g. phosphorylation) as a response to mechanical stimuli. The most prominent examples identified so far are talin and vinculin at cell-matrix adhesions and cadherins at cell-cell junctions [10, 20, 21].

1.2.2 Integrin-mediated adhesions to the ECM

Adhesion to surrounding matrix proteins is one of the prerequisite for the formation of multicellular organisms and tissue structures. In early interference microscopy observations, dark regions closer to the substrate were described as 'feet' of the cell [22]. Today, it is well established that clustering of the transmembrane proteins α - and β -integrin at those sites generates a physical link to the substrate [23]. There are 18 α and 8 β -integrins in mammals, which can be combined to 24 different obligate heterodimers in a cell-type dependent fashion. The intracellular C-terminal domains of integrins act as a scaffold for up to 300 other adhesion and signaling proteins which indirectly or directly bind to them to form the so-called adhesome [24]. Based on their morphology, location, and protein composition

adhesions are classified as focal complex (FX), FA or fibrillar adhesion and are divided into stable and transient structures. During cell migration on two-dimensional surfaces nascent adhesions of about $0.5 \mu\text{m}^2$ form at the cell periphery and mature into streak-like structures with a length of $2 - 10 \mu\text{m}$ (Fig. 1.1 A & 1.2 A).

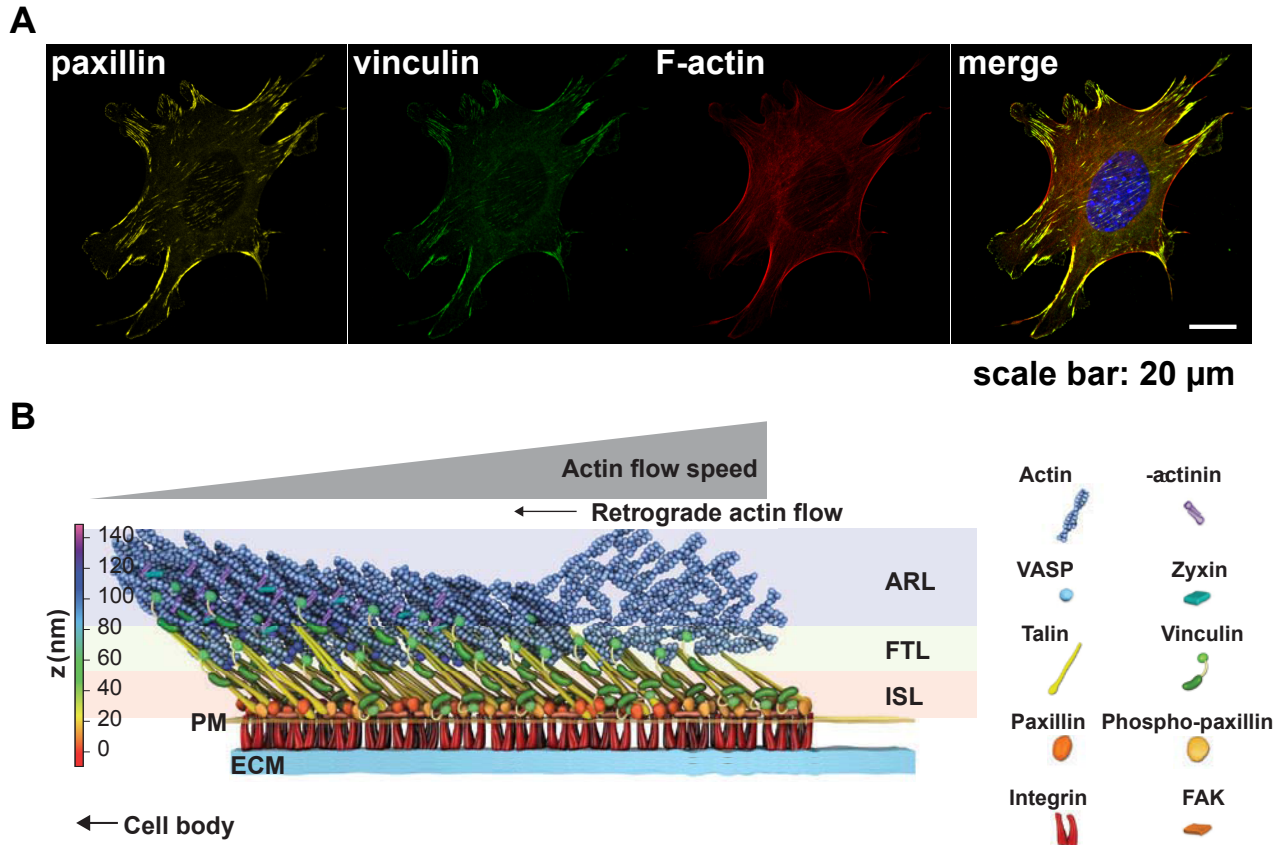


Figure 1.1: Composition of FAs **A.** Immunostaining of a fibroblast on fibronectin (FN) coated glass slide. Focal adhesion proteins vinculin (green) and paxillin (yellow) co-localize with the F-actin cytoskeleton (red) at adhesion structures. FX can be observed as punctae at the cell periphery, while mature FA form at the end-points of stress fibers. **B.** New superresolution techniques like iPALM lead to a better understanding of the 3D organisation of FA. Illustration of the current model for different layers from [25]: FA are divided into an integrin signaling layer (ISL) at $0 - 30\text{nm}$ above the plasma membrane, force transduction layer (FTL) at $30 - 60\text{nm}$ and the actin regulatory layer (ARL) at $> 60\text{nm}$.

The maturation of adhesions is depends on tension generated by the acto-myosin network. Both, inhibition of Rho-associated protein kinase (ROCK) and truncation of the talin rod domain, lead to small residual adhesion structures with reduced levels of vinculin [20]. Superresolution techniques, namely three-dimensional interferometric photoactivation localization microscopy (iPALM), revealed the nanoscale organization of FA and its subdivision into integrin signaling layer (ISL at $0 - 30\text{nm}$ above the plasma membrane), force transduction layer (FTL at $30 - 60\text{nm}$) and actin regulatory layer (ARL $> 60\text{nm}$) [25] (Fig. 1.1 B).

A central view which has evolved during the last years and influences our understanding

of FA structure and function is the molecular clutch hypothesis [25]. Proteins within FAs engage with the retrograde actin flow, leading to the generation of mechanical tension within FAs and traction forces at the outside of cells [27]. This process is very dynamic and still poorly understood. However, it has been recognized that FA clutches crucially depend on protein kinetics: while slip-bonds shorten FA lifetime, catch-bonds strengthen under force and lead to stabilization [28] (Fig. 1.2 B).

1.2.3 The integrin-talin-actin linkage

Activation of integrins, through binding of the talin phosphotyrosine binding (PTB) domain to the cytoplasmic tail of β -integrin, is important for both inside-out, and outside-in signaling at FAs [29]. Binding of the talin tail region with the F-actin cytoskeleton provides a link necessary for cellular rigidity sensing and direct force transduction, which is isoform specific and regulated by vinculin [20, 30]. Functional integrin-talin-actin linkage is a pre-requisite for the proper maturation of FA [20].

Both, talin-1 and talin-2 consist of an N-terminal globular head containing a 4.1 protein, ezrin, radixin, moesin (FERM) domain (47 kDa), and a C-terminal rod (220 kDa) consisting of 13 helical bundles (R1-R13), which can unfold under force to expose up to 11 putative

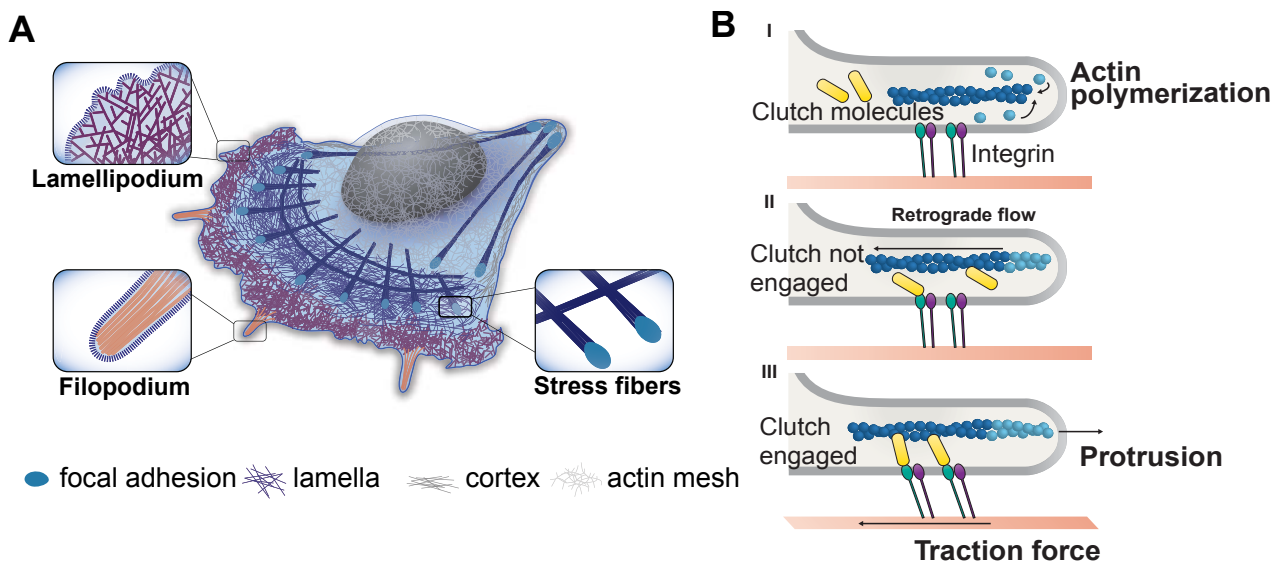


Figure 1.2: Engagement of actin flow at adhesion sites **A.** Filamentous actin can form stress fibers or parallel and cross-linked filaments in different cell compartments. At FAs actin retrograde flow is slowed down and stress fibers are linked to the substrate. The protruding edge of the cell consists of the lamellipodium and filopodia which form extended membrane protrusions [26]. **B.** Proposed mechanism of a molecular clutch: actin polymerization takes place in the lamella where transmembrane protein integrin provides a tether to the ECM (I). A multitude of molecular clutch proteins (e.g. vinculin, talin, α -actinin) bind to either integrins or the cytoskeleton which both serve as a scaffold for multiple FA proteins (II). Upon engagement the F-actin flow can be locked, leading to forward protrusion which is balanced by traction force on the surface (III). Image and model taken from [25].

vinculin binding sites (VBSs) (Fig. 1.5 C) [31]. Data from atomic force microscopy (AFM) studies, *in vitro* reconstitution and structural mutations showed that actomyosin-generated force across the talin rod domain unfurls these cryptic VBSs in a sequential manner (Fig. 1.3 A & 1.5), making it the most prominent molecular strain gauge at FA sites [30, 32, 33].

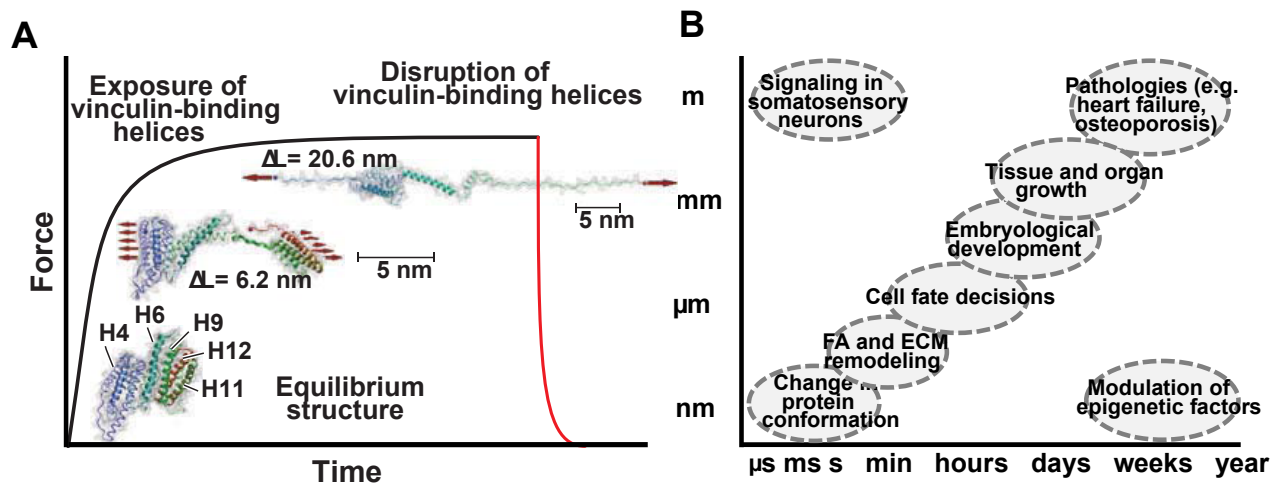


Figure 1.3: Extension of molecular bonds under force **A.** Talin is the most prominent example of a FA mechanosensor which opens up vinculin binding sites under force. Exceeding a threshold force leads to breaking of the bond and results in disruption of vinculin binding helices (taken from [34]). **B.** Mechanotransduction occurs on various time- (μs to years) and length-scales (nm to m). Most processes follow a scaling law with fast events like change in protein conformation on short time and length-scales whereas other processes (e.g. organ growth or development of pathologies) require longer times and manifest in larger size. This is not a universal law as for example somatosensory signaling which is very fast can expand over meters, whereas modulation of epigenetic factors in the genome is a molecular process which can take years.

1.3 Biological function of vinculin and metavinculin

Since its discovery in 1979 [35] vinculin has been ascribed roles ranging from tumour progression [36] and apoptosis [37] to stem-cell differentiation [38], local mRNA translation [39, 40], and facilitation of bacterial entry [41]. Additional to the ubiquitously expressed vinculin, a splice isoform called metavinculin is expressed in smooth (30 – 40 % of total protein) and skeletal muscle (5 – 25% of total protein) with expression levels depending on muscle type, differentiation state and mechanical stimulation of tissue (Tab. 1.1) [42–44]. Here, I want to focus on vinculin’s importance for mechanotransduction at integrin-mediated adhesion structures where it provides a force-bearing linkage to the actin cytoskeleton [10] and compare it to its splice variant metavinculin. While there is an extensive literature on vinculin function and regulation [30, 45, 46], only few comparative studies about metavinculin exist [44, 47, 48].

1.3.1 Structure and regulation of vinculin and metavinculin

Full-length vinculin contains 1066 aa, has a molecular mass of 117 kDa and consists of five domains (D1-D5) which are arranged into a globular head (D1-D4) and a tail domain (D5 or Vt, consisting of 5 amphipathic α -helices H1-H5) linked by a proline-rich strap [49–51] (Fig. 1.4 A-C). Alternative splicing of Exon 19 generates a 68 aa insert in the tail region at aa 883-884, which is flanked by a KWSSK motif, resulting in the isoform metavinculin [52, 53]. The C-terminal half (aa 29-68) of the metavinculin insert, contains the only tyrosine and is conserved across all analyzed vertebrate species [53]. Crystal structures revealed that the metavinculin insert replaces the first α -helix H1 of the vinculin tail domain (Vt) and its N-terminal extended coil by a new α -helix H1', while helices H2-H5 remain unchanged [54] (Fig. 1.4 D-F).

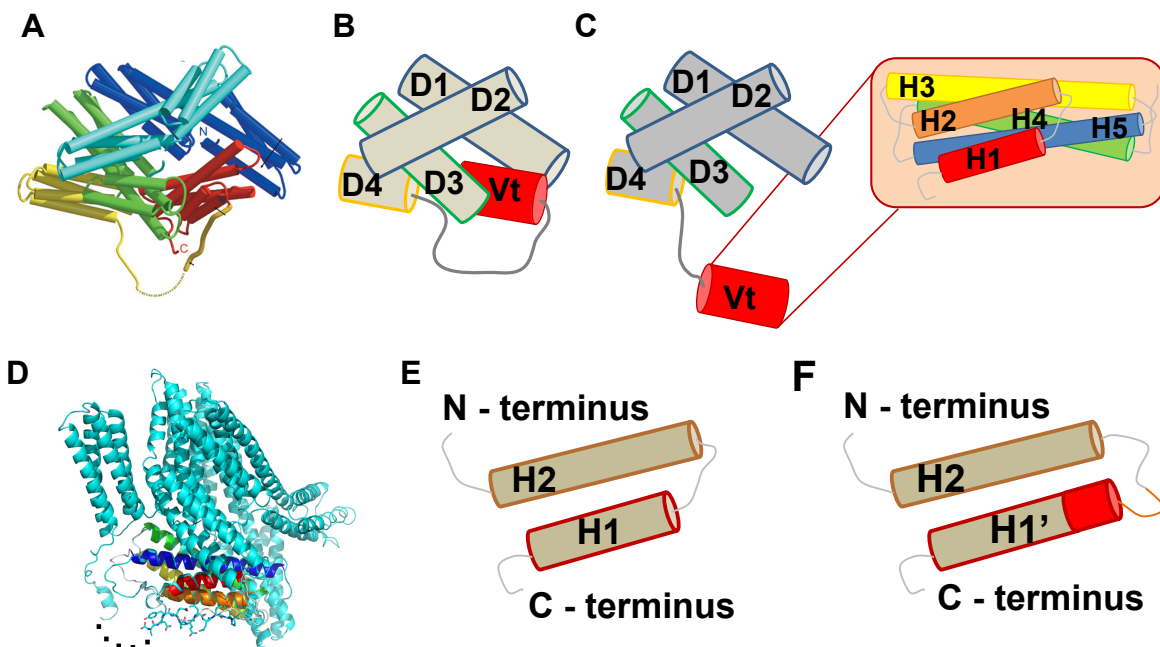


Figure 1.4: Structure and regulation of vinculin A. Crystal structure of vinculin according to [49] B. Schematic illustration of vinculin head (Vh: D1-D5) and tail (Vt) domains in the closed conformation C. Release of head-tail interaction (HTI) leads to an open conformation of vinculin. The tail domain consists of 5 helices (H1-H5) which are connected by flexible linker regions. Image is based on the crystal structure from [55] D. Overlay of crystal structures from Vt (residues 879–915; PDB entry 1rkE) and metavinculin tail domain (MVt) (residues 947–983; cyan). Helices of the Vt are color-coded as shown in C. [54]. E. Domains H1 and H2 of vinculin tail F. The 68 amino acids (aa) long insert of metavinculin replaces the helix H1 by a longer helix H1'. The strap region is elongated.

Association between head and tail domain of vinculin which is mediated by two high affinity interactions (D1-Vt with $K_d = 10^{-7}M$, D4-Vt with $K_d = 10^{-2}M$), leads to an inactive or autoinhibited state [56] (Fig. 1.4 B). It is not clear whether one or two binding partners are necessary to release this head-tail interaction (HTI) (Fig. 1.4 C) but its importance for vinculin localization and function has been demonstrated using various mutants (e.g. head-tail interaction (HTI) (N773A/E775A) and T12 (D974/K975/R976/R978A)) and a

FRET activation sensor [25, 36, 57]. The affinity of the vinculin head domain (Vh) for MVt ($K_d = 3 \cdot 10^{-7}M$) is significantly less than for Vt ($K_d = 5 \cdot 10^{-8}M$) [44].

Early studies suggested that both vinculin and metavinculin form complexes of up to six molecules [50]. More than 30 years later it is still not clear whether and how oligomerization is needed for cellular functions of vinculin. Multiple studies state the importance of vinculin dimerization for F-actin bundling and suggested that metavinculin has to form a heterodimer with vinculin in order to be activated [44, 54]. Upon binding to the lipid phosphatidylinositol 4,5-bisphosphate (PIP₂) vinculin seems to undergo a conformational change which promotes oligomerization of three tail molecules [55].

Phosphorylation has been identified as one of the key mechanisms in the regulation of vinculin localization, activation and function. Abelson (Abl) kinase phosphorylates vinculin at position Y822 specifically in cell-cell contacts after application of force to E-cadherin [58]. Tyrosine phosphorylation at position Y100 and Y1065 is regulated by the Src kinase and has been shown to affect generation of traction force, cell spreading [59, 60] and is needed for contraction of smooth muscle cells [61]. Serine phosphorylation of S1033 and S1045 is mediated by the protein kinase C alpha (PKC α) kinase and also has been implicated in vinculin activation and regulation of force transmission [62]. A recent study compares the effects of phosphorylation and HTI mutants on strain energy, cellular stiffness and turnover rates [63].

1.3.2 Major binding and interaction partners of vinculin and metavinculin

Vinculin serves as a scaffold or adapter protein [64] at FA sites and can recruit other proteins in a force-dependent manner [65]. The head region of vinculin binds to talin, α -actinin, PKC α , *Shigella* invasin (IpaA), α - and β -catenin; proteins of the vinexin family, vasodilator-stimulated phosphoprotein (VASP), Arp2/3 and ponsin bind to the linker region and the vinculin tail binds paxillin, F-actin and PIP₂ [66] (Fig. 1.5 A). Metavinculin shows higher affinity than vinculin for the RNA-binding protein Raver-1, which it can bind even in its closed state [40]. Interactions of MVt with F-actin and PIP₂ have been studied *in vitro* [44], but many details about metavinculin binding partners in the cell are lacking.

Vinculin binding to talin is highly regulated and isoform specific. The talin-1 rod contains at least 11 cryptic vinculin binding sites which open up after stretch-induced conformational changes [31, 32, 67, 68] and keep talin in a vertically extended conformation in FAs [25] (Fig. 1.5 B). Recent data from our lab revealed that mechanically engaged vinculin increases

force across talin and showed that only talin-2 can recruit vinculin in the absence of F-actin binding [20].

Interaction with PIP₂ is supposed to regulate oligomerization properties of vinculin and activation of metavinculin [44, 48, 69]. Lipid binding mutants showed severe defects in cell spreading, adhesion turnover and motility [48, 55, 69].

1.3.3 Role of vinculin and metavinculin during actin bundling and polymerization

In the absence of an activating agent, vinculin does not co-sediment with actin [70] as the binding site is masked by head-tail interaction (HTI) [71]. Upon activation it appears to

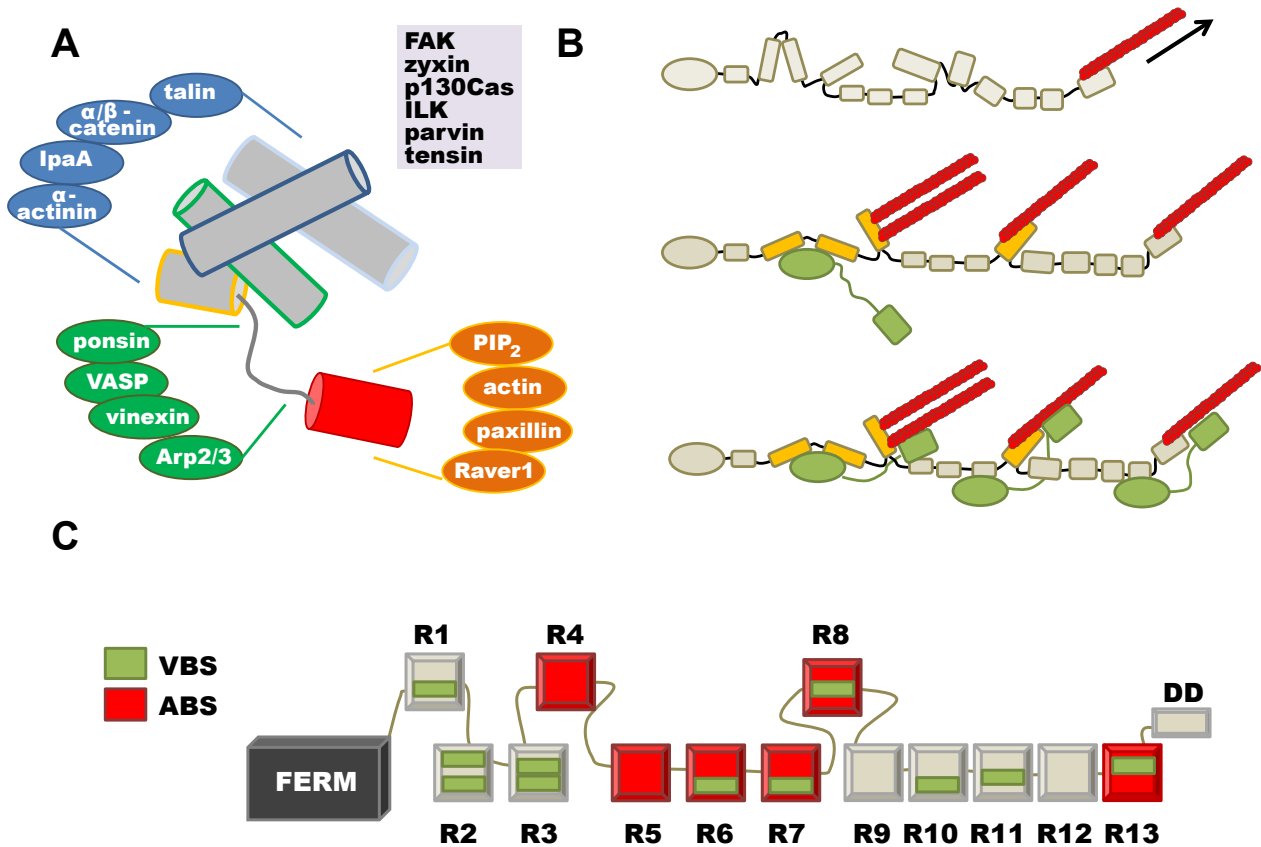


Figure 1.5: Interaction partners of vinculin and metavinculin **A.** Interaction partners of vinculin which bind to head (blue), linker (green), and tail (orange) region of vinculin. The gray insert shows proteins which interact indirectly with vinculin. Inspired by [64] **B.** Model of talin stabilization by vinculin. Actin (red) binding to the talin rod unfurls domains R2-R3 which contain vinculin binding sites. Domains of the talin rod which change their conformation upon actin binding are depicted in yellow. Vinculin (green) is activated upon binding to talin. Further recruitment of actin leads to incorporation of multiple vinculin molecules which lock talin in an unfolded state and stabilize it in FA. Image is based on the model from [30] **C.** Position of actin and vinculin binding sites (ABS in red, VBS in green) in the talin rod domain according to [30]. Most binding sites are masked in the inactive talin and unfold after application of pN forces.

undergo a complex interaction: it was shown to promote actin nucleation [72], barbed end capping [73], but also de-polymerization [74] as well as actin bundling via its C-terminal hairpin (aa 1061-1066) [75, 76].

The original model of Janssen et al. [77] which suggested binding of actin to helices H2 and H3 of Vt has been challenged by the discovery of new actin-binding deficiency mutations (I997A and V1001A) located on helix H4 [78] (Fig. 1.6 A,B). Actin speckle microscopy showed that these mutations were not able to slow down actin retrograde flow at FA [27].

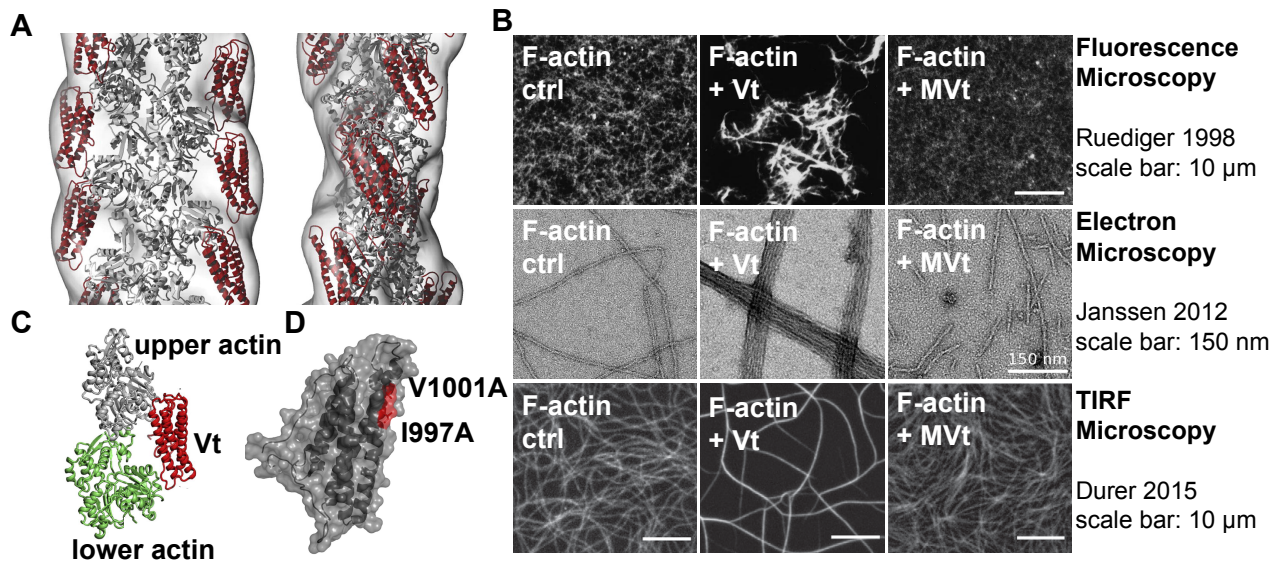


Figure 1.6: Interaction of (meta)vinculin with actin **A**. Janssen model: 3D reconstruction of actin filaments (gray) decorated with Vt (red) (rotated by 90°, 2 nm resolution) from [77] **B**. Three different *in vitro* experiments marking the different levels of MVt and Vt interaction with F-actin. Fluorescence microscopic analysis revealed bundling activity of Vt and showed finer networks for a mixture of actin and MVt [75]. The enhanced precision of electron microscopy suggested a role for MVt [79] in severing actin filaments, however, real-time total internal reflection microscopy (TIRF) revealed a more complicated mechanism in which differences in actin stability and persistence length between Vt and MVt tune actin interaction [80]. **C**. Vinculin tail (red) binding to actin monomers (upper: gray, lower: green). **D**. Proposed actin binding surface (red) in the vinculin tail domain (gray) which can be disrupted using point mutations V1001A or I997A. Crystal structures from [77, 78].

Our understanding of how the MVt insert affects F-actin organization has been growing with the introduction of new experimental techniques (Fig. 1.6 B). Early co-sedimentation studies observed a decreased F-actin bundling activity for MVt constructs *in vitro*, leading to highly viscous F-actin networks [75]. More recent electron microscopy (EM) studies claimed that MVt can sever actin filaments in a process supposedly mediated by a domain with 47% sequence homology to the severing protein gelsolin [79]. This view has now been challenged by the observation, that MVt does not possess a strong severing activity in real-time TIRF experiments [80]. Indeed, it seems that MVt merely tunes the flexibility of actin filaments

which makes them more susceptible to breakage [80]. How vinculin and metavinculin interact with actin in the crowded cytoplasm of living cells remains unknown.

1.3.4 Recruitment to FAs and regulation of force transduction

According to our definition (Tab. 1.2.1) vinculin is both, a mechanosensor and a mechanotransducer, which is involved in passive as well as active mechanotransduction. Knockout of vinculin leads to defective cell spreading, but increases speed of random migration, consistent with the idea that vinculin acts as a molecular clutch to slow down the actin retrograde flow at FAs [27].

Interestingly, cells depleted of vinculin still assemble large FAs and expression of a Vh construct even increases their size. While some experiments show, that loss of vinculin leads to 20 – 30 % reduction in traction force [27, 81], others observe similar traction levels for vinculin depleted cells [38].

The recruitment of full-length vinculin depends on tension generated by the actomyosin network. Inhibition of ROCK (e.g. by Y-27632) leads to disappearance of vinculin from FAs while a Vh construct remains in the small adhesion sites and even stabilizes talin [65]. Some proteins like vinexin are recruited to adhesion sites only upon vinculin activation [57].

With the development of a new genetically encoded vinculin tension sensor (TS) [10] it is now possible to map distribution of FRET efficiencies and relate them to cell shape, FA morphology, FA dynamics, traction force and the geometry of individual stress fibers [82–84]. The emerging picture shows complex multi-modal relationships between these quantities, which are explained by computational models [83] and one study even proposes compression of the vinculin TS [84]. However, due to the high noise level of all experiments which determine FRET ratios from intensity-based methods, special care has to be taken with the interpretation of these results [82].

1.3.5 Tissue specific localization and regulation of metavinculin

Metavinculin is expressed in muscle tissue and has been shown to be involved in myogenesis [42]. However, correlations between metavinculin to vinculin ratio and muscle type, differentiation state or muscle load are complex (Tab. 1.1). Quantification of relative amounts of metavinculin in human tissue showed that metavinculin is highest in smooth and fast skeletal muscle (20 – 30 %) and low in slow skeletal muscle [85, 86]. More recent studies suggest, that this could be directly linked to different fiber types: positive metavinculin

Muscle type	Method	Vinculin	Metavinculin	Ref.
rat soleus (slow skeletal muscle)	hind-limb suspension	+	de novo expression	[88]
rat soleus (slow skeletal muscle)	FAK overexpression	unchanged	++	[88]
rat EDL (fast skeletal muscle)	hind-limb suspension	+	unchanged	[88]
human vastus lateralis	bed rest	unchanged	+	[89]
human vastus lateralis	resistance training	unchanged	++	[89]
mouse tibialis anterior	chronic stimulation	++	-	[90]
mouse tibialis anterior	denervation	++	-	[90]
lamb LTL	sainfoin vs. alfalfa feeding	unchanged	++	[91]
human myometrium	pregnant vs. non-pregnant	total vinculin doubled		[92]

Table 1.1: (Meta)vinculin expression in muscle

staining is observed in fast glycolytic muscle fibers, while it is absent from slow oxidative and fast oxidative glycolytic fibers [87].

During development the amount of metavinculin in human aortic smooth muscle cell (SMC) increases about 7-fold from a 9 – 10 weeks old fetus to a 6 month old child and is rapidly lost when aorta SMC are taken into culture [53]. Furthermore, it has been shown, that metavinculin levels can be altered by muscle loading in humans (Fig. 1.7 D) [89], hindlimb suspension in mice [88] and even change of food source in lambs [91]. De novo expression of metavinculin in rat soleus muscle after hind-limb suspension has been explained by a possible switch from slow to fast muscle type [88]. Interestingly, overexpressing focal adhesion kinase (FAK) in soleus muscle fibers lead to a significant increase of metavinculin, but left vinculin levels unchanged [93].

1.3.6 Involvement of vinculin and metavinculin in physiology and disease

Homozygous knockout of vinculin is embryonically lethal at E10.5 due to severe heart defects [94]. Heterozygous vinculin knockout [95] and cardiac-myocyte specific excision of the vinculin gene [8] both lead to heart failures. The deletion of exon 20 in a mouse model, results in actin binding deficiency [96].

Overexpression of vinculin in *Drosophila melanogaster* induces cardiac remodeling and increased life-span by 150 %, indicating a role in maintaining healthy heart structure [97]. A more regular myofilament lattice induced by vinculin overexpression is thought to reinforce the cortical cytoskeleton (Fig. 1.7 A,B). On the other hand, reduced vinculin expression is observed at intercalated disks during obstructive hypertrophic cardiomyopathy (HCM)

in the human heart and in atherosclerotic tissue [4, 98]. Even before the onset of dilated cardiomyopathy (DCM) vinculin deficient heart tissue showed an increased lattice spacing of myofilament cross-sections and for $\text{vinc}^{+/-}$ myocytes a significant decrease of stiffness was observed [9].

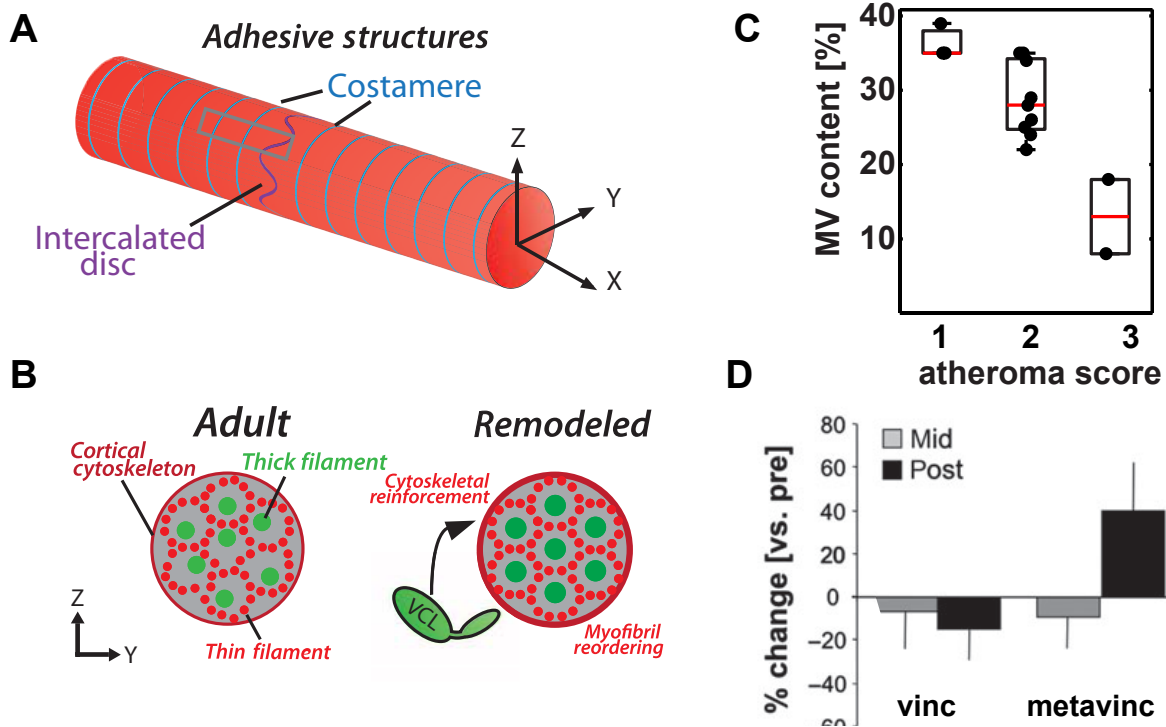


Figure 1.7: Expression of (meta)vinculin in heart, vasculature and muscle tissue **A.** Cardiac myocyte structure showing position of cell-cell junctions called intercalated discs and cell-matrix junctions which are referred to as costameres. **B.** Proposed model for vinculin in maintaining cytoskeletal stability in ageing humans or animals. Myofibrils are reordered upon overexpression of vinculin into a more symmetric myofilament lattice, which can withstand higher forces [97]. **C.** With increasing severity of disease defined by the atheroma score, metavinculin content of atherosclerotic lesions drops. Data taken from [98] **D.** Change of vinculin and metavinculin content in human vastus lateralis before and after bedrest for 34 days [89].

To date, two missense mutations in the metavinculin insert (A934V, R975W) and one aa deletion (L954) have been found in patients with both HCM and DCM; two point mutation are common to both vinculin and metavinculin (L277M, K815R) [4–7] and metavinculin deficiency was linked to idiopathic DCM [99]. Besides cardiomyopathies, metavinculin also might be involved in atherosclerosis as expression levels correlate with severity of plaque formation (Fig. 1.7 C) [85, 98].

1.4 Summary of biological background

FAs provide a major hub for signaling, generate mechanical linkages between the cell and its surrounding and at the same time anchor and regulate the cytoskeleton. Vinculin is only one, albeit a very important, player in FA dynamics involved in shaping local interactions, e.g. with talin or F-actin, as well as regulating the function of organs like the heart. The 68 aa muscle-specific metavinculin insert in the tail domain has already been described more than 35 years ago and experimental evidence for its relevance is accumulating, while little progress has been made in understanding metavinculin's molecular function. I presented existing findings on metavinculin's role in F-actin bundling and disease.

Understanding isoform-dependent regulation of proteins provides a more general insight into how biological structures deal with varying mechanical stimuli and force ranges in different tissues. It is beyond the scope of this thesis to link molecular function to tissue specific gene expression, however, it should be kept in mind that direct pathways between mechanotransduction at FA and signaling to the nucleus exist.

2 Biophysical and theoretical background

The challenge to perform biophysical experiments in living cells can be divided into two parts: providing reproducible, well-defined mechanical or biochemical stimuli and - even more intricate - developing methods for a reliable read-out of parameters. These methods should minimally disturb the system and be robust enough to generate significant results in the presence of biological noise. Linking measured values to physical quantities requires a theoretical description of biological properties and relies on additional calibration experiments.

Here, I present a biosensor technology to measure pN forces across single proteins and introduce the theoretical background which is important for its application, but also for the general description of mechanobiological properties of single cells. On the single protein level, statistical theories which account for the occupation of different states, like the worm-like chain (WLC) model, need to be employed. We use the fact, that this nanoscale description of protein conformation is an adequate input for the Förster equation and can be used for the description of single-molecule calibration experiments of our biosensors.

On the other hand, biophysical experiments like TFM, cell stretching or the use of micropatterns and elastic substrates are described. Elasticity theory is a powerful tool which can be used to quantify both, the deformation of flexible substrates and of the whole cell or the cytoskeleton, under the assumption of small linear deformations. Together, these experimental methods and the read-out by FRET-based TSs provide a framework for the comparative study of vinculin and metavinculin.

2.1 Genetically encoded FRET-based tension sensors

A current review lists the generation of FRET-based protein stretch sensors as one of the milestones in the history of mechanotransduction research [16]. Here, I want to discuss their implementation for live cell measurements in FA proteins and show both, advantages and limitations, of their evaluation with time-correlated single photon counting (TCSPC)-fluorescence lifetime imaging microscopy (FLIM).

2.1.1 Principle of FRET measurements

The rate of FRET between two light-sensitive molecules (e.g. organic dyes, fluorophores) depends on their separation distance r , orientation κ and the overlap integral J between the normalized donor fluorescence intensity F_D and the extinction coefficient $\varepsilon_A(\lambda)$ of the acceptor [100]. Transfer of energy from the donor molecule D to the acceptor A is non-radiative and its efficiency can be calculated as

$$E = \frac{R_0^6}{r^6 + R_0^6} \quad (2.1)$$

with the Förster distance R_0 which is constant for a given $D - A$ pair and given as

$$R_0^6 = \frac{0.9 \ln(10) \kappa^2 Q_D}{128 \pi^5 N_A n^4} \int_0^\infty F_D(\lambda) \varepsilon_A(\lambda) \lambda^4 d\lambda \quad (2.2)$$

with quantum yield Q_D , refractive index n and Avogadro's number N_A [100]. For experimental measurements the relation between FRET efficiency E and donor intensity I or lifetime τ in presence (I_{DA} , τ_{DA}) or absence (I_D , τ_D) of the acceptor is often described as

$$E = 1 - \frac{I_{DA}}{I_D} \quad (2.3)$$

$$E = 1 - \frac{\tau_{DA}}{\tau_D} \quad (2.4)$$

This simplification is only true under the assumption of a fixed distance between D and A . For this study the FRET-pairs venus/monomeric Cherry (mCherry) and genetically truncated version of yellow fluorescent protein (YFP) (YPet(s))/mCherry with a Förster radius of approximately 5.8 nm were used.

2.2 Calibration of linker peptides

A tension sensor module consists of a linker peptide which is flanked by two fluorophores or organic dye molecules at a distance of 2 – 5 nm, leading to a high initial FRET (Fig. 2.1 A). Upon stretch the dye molecules are separated and FRET efficiency decreases. Calibration of the linker peptide or even the whole TS module via single-molecule measurements or

theoretical modeling defines a direct relationship between the applied force in the pN range and the extension of the linker in nm or the FRET efficiency E [20].

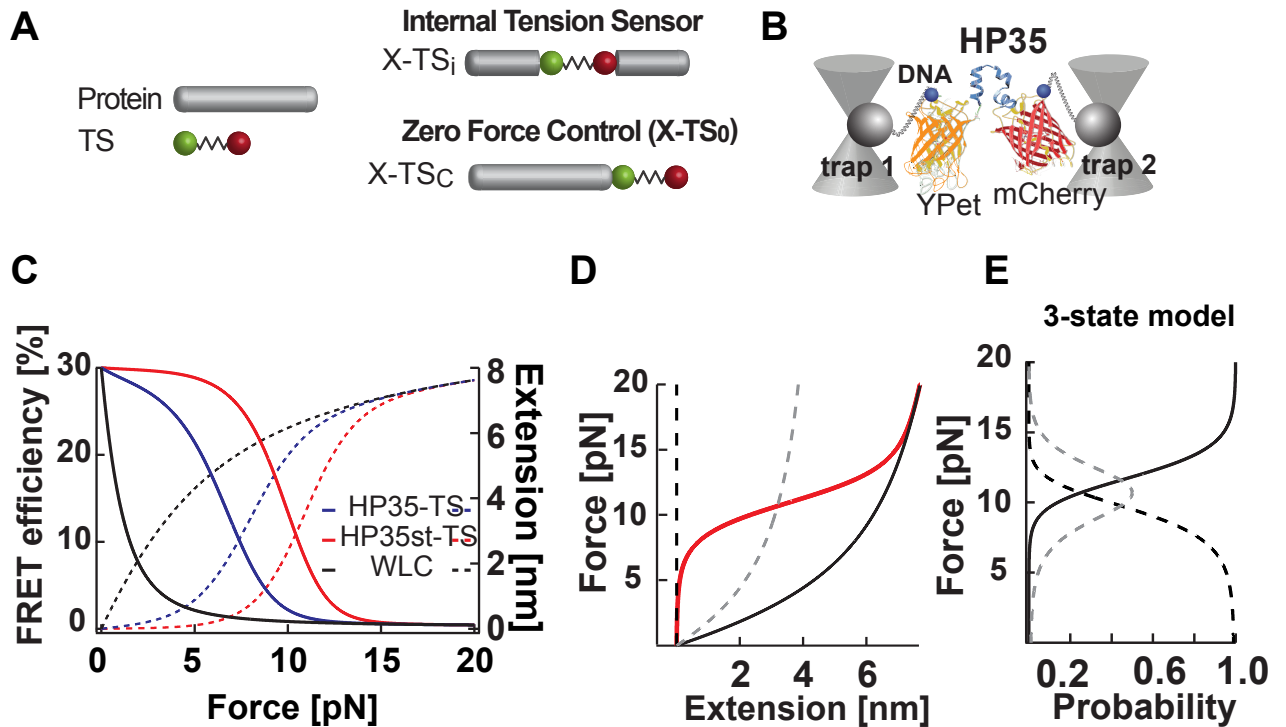


Figure 2.1: Calibration of peptides for tension sensor measurements A. Illustration of TS modules used for internal sensors and zero-force control as depicted in [101] B. Two laser traps are used to calibrate the villin headpiece peptide (HP35) linker peptide. DNA was attached on each site of the purified HP35 construct, which consists of two fluorophores (YPet(s) and mCherry) and a linker, using cysteins. Figure taken from [20]. C. Curve of FRET efficiency vs. force for modelled curves of HP35 and stable. Fits were performed using a WLC model with three states. D. Contributions of unfolded (black), folded (black dashed) and semi-folded (gray dashed) states to the force-extension curve of the HP35 linker peptide. The average protein extension as a function of force is depicted in red. E. Probability distribution for the occupation of different states depending on force. B. - E. Taken from [20].

For this study two calibrated peptides have been used: an amino-acid motif from the spider silk protein flagelliform consisting of eight *GPGGA* repeats (F40) being sensitive to forces in the range of 1 – 6 pN [10] and a villin headpiece peptide (HP35) which can be tuned by a double point mutation (HP35st) between force ranges of 6 – 8 pN or 9 – 11 pN [20]. While the flagelliform linker had been calibrated via fluorescence force spectroscopy using two organic dyes (Cy3 and Cy5) to determine the force-FRET efficiency relation [10], the force spectroscopy for the HP35 was performed using the original fluorophores YPet(s) and mCherry and two laser traps for direct measurement of the extension length [20].

Force sensing elements which have been used by other groups include α -helices [102], spectrin repeats [102], and PEG polymers tethered to surfaces [103]. For a complete review please refer to [101].

2.2.1 Theoretical description of linker peptides

The reaction of an entropic spring to an external force F can be modeled by a basic WLC model which assumes a rigid behavior at short distance and flexible behavior at length scales larger than the persistence length l_p . To maximize its entropy a polymer peptide will maintain a conformation with an end-to-end distance significantly smaller than the contour length. We can write this down as Hamiltonian operators for the entropic part and the external force F

$$\mathcal{H} = \mathcal{H}_{entropic} + \mathcal{H}_{external} = \frac{1}{2} k_B T \int_0^{l_0} l_p \cdot \left(\frac{\partial^2 \mathbf{r}(s)}{\partial s^2} \right)^2 - xF \quad (2.5)$$

An interpolation formula which states that forces are in the order of $F \sim k_B T / l_p$ can be used as a fit for experimentally derived force-extension relations [104]

$$F(x, l_p) = \frac{k_B T}{l_p} \left(\frac{1}{4(1 - x/l_p)^2} - \frac{1}{4} + \frac{x}{l_p} \right) \quad (2.6)$$

With the Förster radius and the fluorophore separation distance the mean FRET efficiency E can be linked to a given force F . Based on experimentally observed force-extension curves a model of the distribution of single folding states can be derived. For n states it is given in a general form as

$$E_{FRET}(F) = \sum_{i=1}^n E_{FRET}(x_i(F)) \cdot p_i(F) \quad (2.7)$$

with the probability $p_i(F)$ for a given state i with extension $x_i(F)$ (note: $\sum_i p_i(F) = 1$). The most simple case is a direct transition between a completely folded and unfolded state, however, the assumption of intermediate states (e.g. folding of sub-domains) might be necessary to fully explain protein behavior. For calibration measurements of the linker peptide HP35 a 3-state WLC model with folded, unfolded and partially folded states accurately reproduces experimental data (Fig. 2.1 D,E) [20].

2.2.2 Introduction of tension sensor modules into the protein of interest

The calibrated tension sensor module can be introduced into a protein of interest and analyzed *in vitro*, in living cells or even inside living organisms [101]. To access whether a certain protein bears mechanical force in a specific cellular context or upon stimulation by external forces, a suitable insertion site, which maintains protein functionality, has to be

limitation	examples
structural	FRET upon conformational change, alteration of domain structure, intermolecular FRET, oligomerization, cleavage of fluorophores, incomplete folding or labeling
biological	impaired localization, change in binding partners, altered dynamics, too high or too low expression level, cell cycle arrest
photophysical	variable chromophore orientation, limitations by shot noise and signal-to-noise ratio, effects of pH or temperature dependence

Table 2.1: Factors disturbing live cell tension sensor experiments

determined. Usually unstructured regions between protein domains, like the proline-rich linker in vinculin, are well suited for TS module insertion.

Besides structural integrity, maintenance of biological function is crucial and has to be well tested. Rescue of cells with a TS construct after knockout of the target protein is recommended to avoid effects of overexpression and test biological function. Table 2.1 and publications from our group [10, 101, 105] list additional potential confounding factors, additional control experiments need to be tailored to each individual system and protein of interest.

2.2.3 Live cell measurements using TCSPC-FLIM

Confocal laser scanning microscopes (LSMs) can be used to evaluate fluorescence signal from fluorophores inside living cells. As discussed before, FRET is expressed as a change in donor intensity or lifetime (eq. 2.4). Both quantities are used to determine FRET efficiency in biological samples: intensities can be mapped by approaches like ratiometric FRET, donor- or acceptor photobleaching, whereas lifetimes are determined by FLIM [100].

In contrast to intensity-based methods, FLIM is independent of fluorophore concentration over a wide range. Donor and acceptor are always linked in TS constructs, however, not all fluorophores might be completely folded. While unfolded donor molecules do not appear in the measurement, incomplete folding of the acceptor leads to measurement of donor lifetime only. FLIM can be measured in time or frequency domain by exciting the sample either with single laser pulses shorter than the lifetime (e.g. 10 – 100 fs) or intensity modulated light

(frequency domain FLIM) [106]. Photon arrival times are measured by a TCSPC detector with parallel photomultiplier (PMT) detectors.

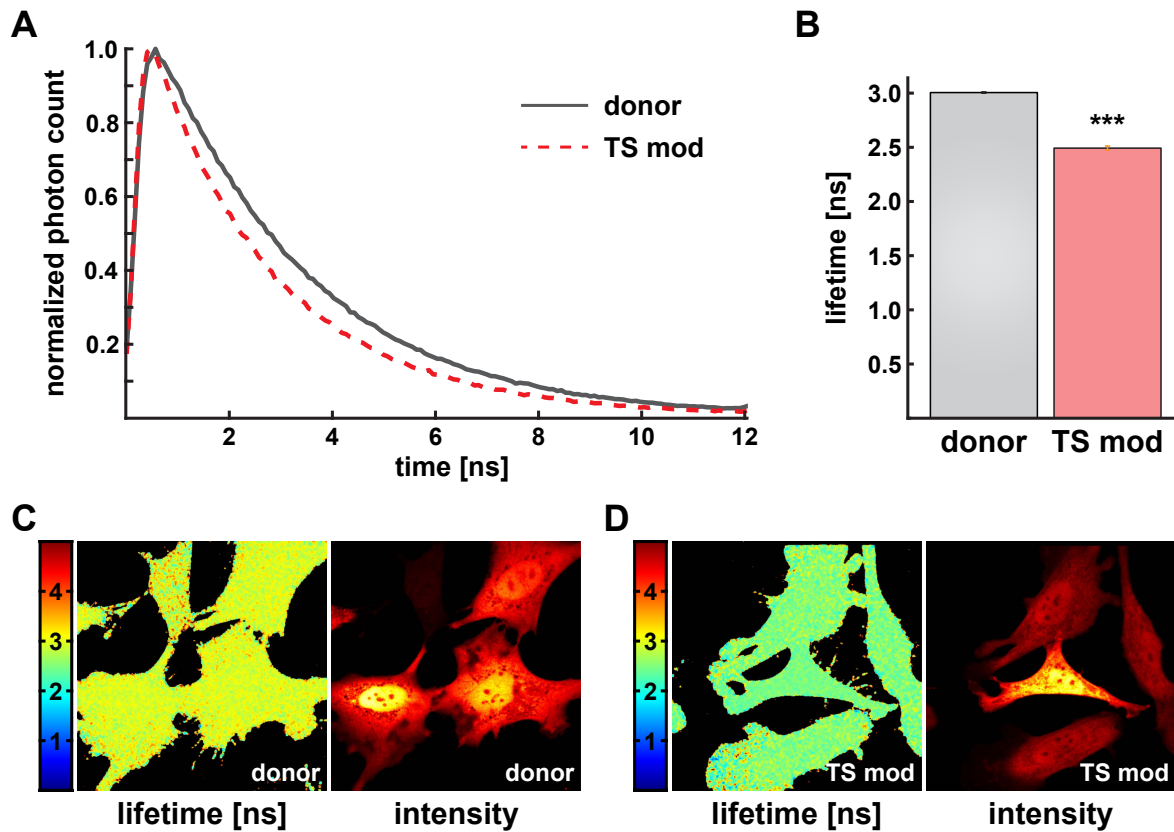


Figure 2.2: Measurement of FRET in living cells using TCSPC-FLIM **A.** Experimental photon count curves from lifetime measurements of donor fluorophore (venus) and TS construct (F40). Both curves were normalized to maximum count. **B.** Mean lifetime over ten experiments, error bars indicate standard error of the mean (SEM). A significant decrease in the lifetime of donor in presence of the acceptor can be seen in the TS construct. **C. & D.** Lifetime of donor and TS construct calculated as a function of position. Note that FLIM measurements not depend on intensity and dim or bright areas fluorescence image yield the same values for lifetime. All images taken from [105].

2.3 Mechanical manipulation of the cellular environment

2.3.1 Linear elasticity theory in the context of TFM and cell stretching

Next, some general concepts from linear elasticity theory which are important for the interpretation of both TFM and cell stretching experiments will be introduced. We only consider isotropic, incompressible elastic materials (Poisson ratio $\nu \approx 0.45$ for polyacrylamide (PAA) and $\nu \approx 0.5$ for PDMS), which retain linear behavior as long as small deformations $\varepsilon \ll 1$ are applied. For well-spread adherent cells, e.g. fibroblasts on FN coated PAA substrates, algorithms which assume an infinitely large thickness and neglect forces normal to the surface can be employed [107]. The displacement vector field $\mathbf{u} = \mathbf{x}' - \mathbf{x}$ describes the transformation between the initial state \mathbf{x} and the deformed state \mathbf{x}' , where \mathbf{x} is a vector with components (x, y, z) , referred to by indices i, j, k . As discussed above, for small strains a linearization applies and the strain tensor ε can be written in component notation as [108]

$$\varepsilon_{ij} = \frac{1}{2} \left(\frac{\partial u_i}{\partial x_j} + \frac{\partial u_j}{\partial x_i} \right). \quad (2.8)$$

Each component of the stress tensor σ_{ij} can be written as (δ_{ij} : Kronecker delta)

$$\sigma_{ij} = \frac{E}{1 + \nu} \left(\varepsilon_{ij} + \frac{\nu}{1 - 2\nu} \varepsilon_{kk} \delta_{ij} \right). \quad (2.9)$$

The relationship between the stress tensor σ and the strain tensor ε depends on the material properties Poisson ratio $\nu = -\frac{\varepsilon_{yy}}{\varepsilon_{xx}} = -\frac{\varepsilon_{zz}}{\varepsilon_{xx}}$ and Young's modulus $E = \frac{\sigma}{\varepsilon}$. While the Poisson ratio describes the coupling between different dimensions, the Young's modulus quantifies the substrate stiffness and is given in units of Pascal ($1 \text{ Pa} = 1 \frac{\text{N}}{\text{m}^2}$); the shear modulus G can be calculated from the Young's modulus E as $G = \frac{1}{2} \frac{E}{1 + \nu}$. The elastic modulus E scales with the length-scale of interactions as $\frac{1}{r^2}$, leading to large differences in its value for different materials (diamond $\approx \text{TPa}$, rubber $\approx \text{MPa}$, cells $\approx 10 \text{ kPa}$) [109]. In the context of biomechanics of the cytoskeleton or the ECM most interactions are in the range of $10 - 500 \text{ nm}$ and typical elastic moduli are between $0.1 - 50 \text{ kPa}$. To calibrate experimental systems the position of fiducial markers (e.g. fluorescent beads) or regular patterns is tracked after the application of known forces [110]. Substrate stiffness can be measured via AFM, film stretching under gravity or bulk rheology [111].

2.3.2 Analysis of cellular traction forces

Seeding of cells on two-dimensional elastic substrates generates deformations, which can be visualized by tracking the movement of embedded fluorescent beads [112] (Fig. 2.3 B). Other methods to map cellular traction force include measurements of substrate wrinkling, and micropillar deflection [34, 113, 114] (Fig. 2.3 A,C). It is also possible to estimate the force generated by integrin via the extension of TS tethered to the surface [115] (Fig. 2.3 D).

Areas of large traction coincide with positions of FA and forces are positively correlated with FA size within single cells [113, 114]. Typical stresses per FA across different cell types are in the range of $1 - 5 \text{ nN}/\mu\text{m}^2$ [116]. Interestingly, increasing FA size does not automatically strengthen attachments, as higher actin flow rates are associated with FA enlargement [27]. Recent experiments show that spread area alone regulates tension of adherent cells and claim an independence of cell geometry or total number of FA [117].

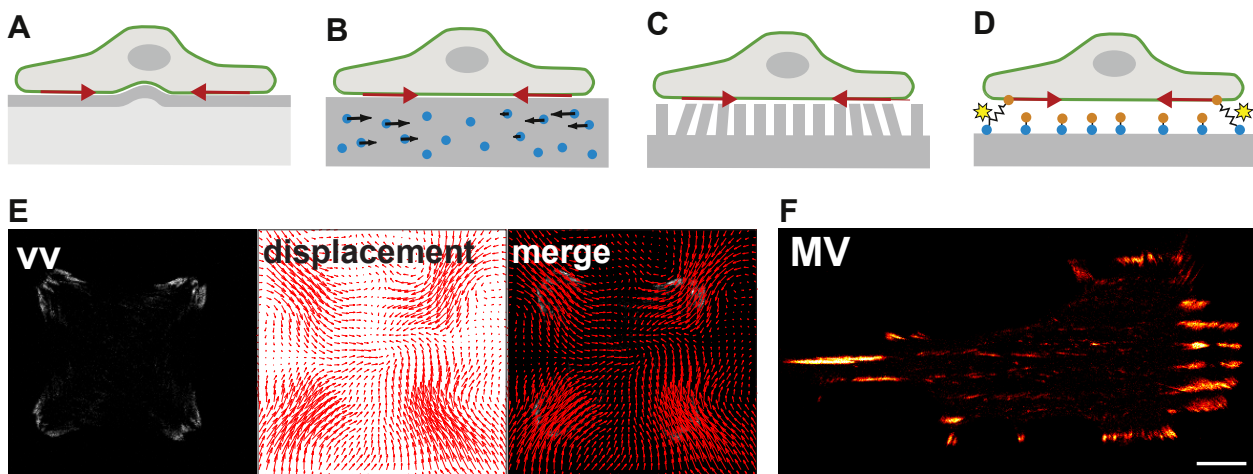


Figure 2.3: TFM and micropatterning A.-D.: Different approaches to measure cellular traction forces [108]: **A.** wrinkling of the substrate, **B.** tracking of beads embedded in soft substrates, **C.** micropillar arrays or **D.** tension sensor constructs tethered to the surface. **E.** Fibroblast with vinculin-venus (VV) on cross shaped of micropatterns of $40 \mu\text{m}$ width on 8 kPa PAA, red arrow indicate traction field calculated by Fourier transform traction cytometry (FTTC) **F.** Vinculin knockout fibroblast with metavinculin-venus (MV) stained FA on parallel pattern of $5 \mu\text{m}$ spacing and $1 \mu\text{m}$ width, scale bar $10 \mu\text{m}$.

2.3.3 Modulation of substrate stiffness and micropatterning

Cell morphology can be influenced by choice of ECM coating ligand (e.g. FN, collagen, poly-L-lysine (PLL)), substrate stiffness and micropatterning approaches which restrict the accessible surface. Micropattern geometries use lines or dots, which restrict FA position, but allow normal cell spreading or regularly shaped areas (e.g. circles, squares, triangles) that

restrict spreading and allow free FA formation, as well as combinations of both [118]. Cells will only be able to adhere when integrin cluster spacing is not exceeding a threshold of $50 - 100 \text{ nm}$ [119].

Stiffness can experimentally be tuned between 100 Pa and 10^9 Pa on glass surfaces [111]. However, the typical threshold for efficient spreading is around 500 Pa , as many cell types will not be able to generate sufficient forces to adhere on softer substrates and round up [120, 121]. Some surface ligands like PLL allow cells to adhere to a substrate without spreading and mimic behavior on soft substrates. Rigidity sensing enables cells to follow stiffness gradients in a process called durotaxis and can be regulated by expression of different integrin subtypes or talin isoforms [20, 121].

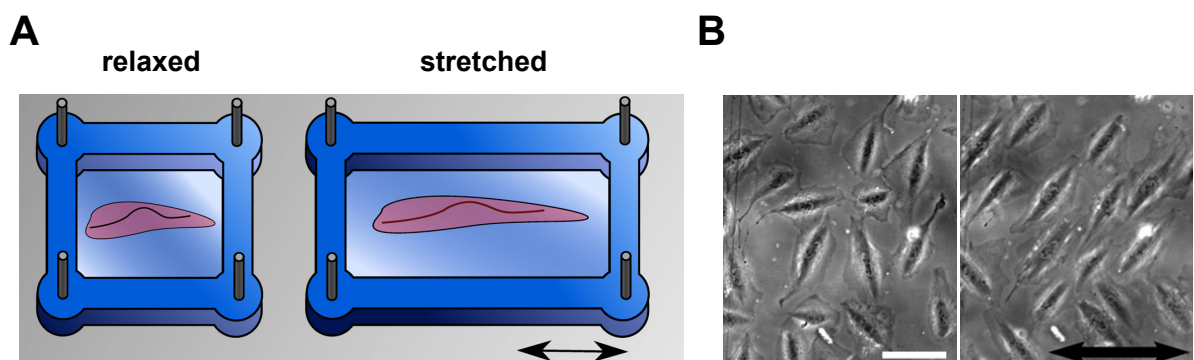


Figure 2.4: Stretching of cells on elastic substrates **A.** Schematic illustration of a uniaxial cell-stretcher consisting of a polydimethylsiloxane (PDMS) chamber, which can be elongated using a motorized positioning stage. Cells are seeded on top of the coated PDMS experience the stretch and reorient their shape and cytoskeleton accordingly. Taken from [124] based on the original publication [110]. **B.** Reorientation of fibroblasts seeded on FN coated PDMS (6 h of 10 % stretch at 1.2 Hz). Scale bar $40 \mu\text{m}$, arrow indicates axis of largest principal stretch. Image taken from [123].

2.3.4 Cell stretching

In the human body cells are constantly stretched and compressed as a result of muscle activity or changes in hydrostatic pressure. Stretching is for example very prominent in heart tissue or in myometrium during labor, where it can be described as clearly distinct stretch and relaxation cycles with a defined frequency. To study the response of single cells to external stretch, transparent flexible substrates are either deformed transiently or stimulated periodically. Both, uniaxial and cyclic stretches are used to mimick naturally occurring deformations (e.g. FlexCell or devices described in [110, 122]). Live cell imaging and immunostaining can be used to quantify reorientation of the cytoskeleton and FAs, following stress of different frequency or magnitude [110, 123]. Experimental data shows that cell morphology follows changes in the actin cytoskeleton with a temporal delay and maintains an angular orientation which can be described by theoretical modeling [110].

One prediction was, that cells should orient their cytoskeleton towards the direction of minimal strain, which can be calculated from the transversal shrinkage factor $k = -\frac{\varepsilon_{yy}}{\varepsilon_{xx}}$ using the main components of the strain tensor ε which has already been defined in section 2.3.1 and can be experimentally measured as described in [110]. However, a recent study shows that it is necessary to introduce an additional parameter which accounts for cell's elastic anisotropy [123]. Minimizing intercellular shear stress also seems to be important in the context of collective cell migration where forces are shared at cell-cell junctions [125].

3 Aims of the thesis

The central role of vinculin in cell adhesion, FA dynamics and intracellular force transduction is broadly recognized. However, the role of its splice variant metavinculin remains obscure. Therefore, this thesis analyzes the role of metavinculin with respect to cell adhesion and intracellular force propagation. A better knowledge about mechanotransduction across metavinculin also helps to understand how mechanical misregulations in diseases like cardiomyopathy or atherosclerosis could evolve. The specific aims are:

Aim 1) Comparison of vinculin and metavinculin expressing cell lines

To distinguish the effects of vinculin and metavinculin on FA morphology and cell spreading, fluorescently tagged constructs will be compared in a cell line depleted of both isoforms. This model system is also suited to analyze differences in protein dynamics and interaction partners.

Aim 2) Generation and characterization of FRET-based tension sensors (TSs) for vinculin and metavinculin

Genetically encoded FRET-based TS serve as a tool to measure the pN forces transduced via a protein. Vinculin has already been identified as a mechanotransducer in FA and I plan to generate a metavinculin TS to compare differences between both isoforms. To evaluate the signal of FRET-TS in living cells, a measuring and data analysis routine for fluorescence lifetime imaging microscopy (FLIM) has to be set up.

Aim 3) Comparative analysis of force transduction across vinculin and metavinculin by insertion of mutations and changes in cellular environment

In the last step, I want to analyze point mutations which affect the F-actin interaction and the HTIs of vinculin and metavinculin. Mechanical manipulation of the environment can for example be achieved by uniaxial stretching of the substrate or change in substrate stiffness. To measure whether metavinculin expression has an influence on active mechanotransduction, traction force microscopy (TFM) will be implemented.

4 Experimental Methods

4.1 Biochemical methods

4.1.1 Preparation of protein lysates for SDS-PAGE

Adherent cells were trypsinized, seeded out in a 6-well at 90% confluency and left to attach in the incubator for 120 *min* (37 °C, 5% CO₂). After a fast washing step with phosphate buffered saline (PBS) cells were lysed in 400 μ l lysis buffer (Tab. 4.1) for 10 *min* on ice. For analysis of phosphorylated proteins a phosphatase inhibitor cocktail was added to the lysis buffer.

Washing steps for detached cells involved 5 *min* of centrifugation at 300 *g*, the lysis buffer was directly added to the pellet. During the last 3 *min* of the lysis cells were detached with a cell scraper and centrifuged at 13.000 *g* for 10 *min* at 4 °C. The supernatant was transferred to a fresh tube.

Protein concentration was determined with a bicinchoninic acid (BCA) protein assay kit (Novagen User Protocol TB 380 Rev. D0111 JN). The reaction was incubated for 30 *min* at 37 °C and absorbance at 562 *nm* was measured with a plate reader (Tecan Sunrise microplate reader, Mannedorf Switzerland). Intensity values were background corrected and fitted with a custom written MATLAB program and adjusted to final concentrations of either 0.3 *mg/ml* or 1 *mg/ml*. After adding 4 *x* Laemmli buffer (Tab. 4.2) samples were denatured for 5 *min* at 95 °C and either cooled to room temperature (RT) on ice for immediate loading to a sodium dodecyl sulfate (SDS)-polyacrylamide gel electrophoresis (SDS-PAGE) gel or stored at –20 °C.

4.1.2 Co-Immunoprecipitation using magnetic beads

For co-immunoprecipitations a 10 *cm* culture dish densely covered with cells was lysed in 400 μ l lysis buffer (Tab. 4.1). To avoid breakdown of protein complexes all steps were performed fast on ice or in the cold room. After the centrifugation step the cell lysate was

Lysis buffer

150 mM	NaCl
50 mM	Tris pH 7.6
1%	Triton-X-100
1-2 tablets/10 ml	protease inhibitor cOmplete Ultra
1 tablet/10 ml	phosphatase inhibitor PhosSTOP

Table 4.1: Lysis buffer

Laemmli 4 x pH 6.8

250 mM	Tris-HCl pH 6.8
20 %	glycerol
4 %	SDS
0.02 %	bromphenol blue
4 %	β -mercaptoethanol

buffer containing β -mercaptoethanol was stored at -20°C

Table 4.2: Laemmli buffer

incubated with 50 μl of Anti-HA-Tag or Anti-GFP-Tag Micro Beads (μMACS Epitope Tag Protein Isolation Kit # 130-091-122 or #130-091-125, Miltenyi Biotec). Magnetic beads were washed as described in the general protocol from Miltenyi Biotec using lysis buffer instead of Wash Buffer 1.

4.1.3 One-dimensional SDS-PAGE and Western blotting

To separate proteins according to size, SDS-PAGE was applied. While pre-made gels (BioRAD Laboratoires GmbH, MiniProtean TGX Precast Gels, 10 % or 4 – 15 % gels 10 wells with 30 μl , Cat. No. 456-1083 or 456-1033) proved adequate for fast testing of protein amounts, self-made PAA gels had a higher quality and were better suited to separate bands of similar height and quantify expression levels. After washing and assembly of glass molds ammonium persulfate (APS) and N,N,N',N'-tetramethylethylenediamine (TEMED) were added to the stacking gel (Tab. 4.4) and it was thoroughly mixed and carefully pipetted between the glass plates. The gel was allowed to polymerize for at least 45 *min*, covered with a layer of isopropanol. After removing the isopropanol layer a separating gel (Tab. 4.5) was poured on top and a 10-well comb was inserted. Up to 30 μl of denatured protein sample, corresponding to a total of 1 – 5 μg of protein was loaded into the wells of the gel. Suited markers were used (e.g. prestained SDS-PAGE protein marker 6.5 – 200 *kDa* Liquid mix from SERVA Electrophoresis, PageRuler PLUS Prestained Protein Ladder 10 – 250 *kDa*

Thermo Scientific). Self-made PAA gels were run in SDS-PAGE running buffer (Tab. 4.3) at 120 V until the end of the stacking gel and turned up to 160 V; pre-made gels were run according to manufacturers recommendations, but no higher than 200 V to avoid excessive heating.

SDS-PAGE running buffer 10 x

30.3 g	Tris
144 g	glycine
5 ml	20% SDS
add to 1 l	ddH ₂ O

Table 4.3: Running buffer

Stacking gel 5 %

3.4 ml	ddH ₂ O
630 μ l	1.5 M Tris-HCl pH 6.8
830 μ l	30% PAA
40 μ l	10% SDS
	for polymerization
40 μ l	10% APS
4 μ l	TEMED

Table 4.4: Stacking gel

Separating gel 10 %

4.0 ml	ddH ₂ O
2.5 ml	1.5 M Tris-HCl pH 6.8
3.3 ml	30% PAA
100 μ l	10% SDS
	for polymerization
100 μ l	10% APS
10 μ l	TEMED

Table 4.5: Separating gel

Next, proteins were transferred to a polyvinylidene difluoride (PVDF) membrane by western blotting. Activation of the membrane was achieved by short soaking with methanol and equilibration in 4 °C blotting buffer. For protein transfer, a sandwich consisting of three foam sponges and a Whatman paper on each side was assembled and soaked in blotting buffer (Tab. 4.6). Inside the sandwich the PAA gel was positioned on top of the PVDF membrane, with the gel oriented towards the cathode and the membrane towards the anode.

A voltage of 100 V for 1.5 h or 20 V overnight (o/n) was applied to the transfer apparatus, which was kept at 4 °C with a cool pack of ice and constant stirring.

SDS-PAGE blotting buffer 10 x

800 ml	1 x SDS-PAGE running buffer w/o
	SDS
200 ml	methanol

Table 4.6: Blotting buffer

The sandwich was disassembled and rinsed with Milli-Q filtered water (ddH₂O) and TBS-T 4.7. For blocking of unspecific binding sites the membrane was covered with 5% skimmed milk in tris buffered saline (TBS) polysorbate 20 (Tween20) (TBS-T) and left to shake at RT for 45 min. Primary antibodies were diluted according to Tab. 10.5. and incubated 1 h or o/n in either 5% skimmed milk or 5% BSA. After washing three times 5 min with TBS-T the secondary antibodies were left to incubate for 1.5 h at RT, followed by a washing step. Detection of chemiluminescence signal was enabled by soaking the membrane in a 1 : 1 mixture of luminol and peroxide (Immobilion Western, Millipore Corporation, Billerica USA, Cat. No. WBKLS0500) for 5 min in the dark. The signal was detected using an ImageQuant LAS-4000 (Luminescent Image analyzer, GE Healthcare Bioscience) with typical exposure times ranging from 8 s to 3 min.

To enable parallel analysis of multiple different proteins, the membrane was either cut into appropriate pieces prior to incubation with the first antibody or stripped after the chemiluminescence analysis. For antibodies from different species, a mild stripping buffer (Tab. 4.8) was used. The membrane was incubated twice for 10 min in stripping buffer, washed two times for 10 min in PBS and two times for 5 min in TBS-T. The membrane was blocked and incubation with antibodies proceeded as described before.

TBS buffer 10 x pH 7.4

80 g	NaCl
23.4 g	Tris-HCl pH 7.4
	approx. 16 ml HCl

for TBS-T add 1 ml Tween 20 to 1 l TBS

Table 4.7: TBS buffer

Mild stripping buffer

15 g	glycine
1 g	SDS
10 ml	Tween 20

add up to 1 l ddH₂O and adjust to pH 2.2

Table 4.8: Mild stripping buffer

4.1.4 Purification of IpaA

The bacterial entry protein IpaA was purified for use in actin ultracentrifugation experiments according to the protocol used by [57]. To start a bacterial culture, 1 μ l of pGEX vector plasmid with IpaA complementary deoxyribonucleotide acid (DNA) (cDNA) was transfected into 50 μ l competent BL-21 cells. A single clone was picked and a starter culture of 20 ml was grown o/n and 8 ml of this culture were used to let 200 ml bacteria in lysogeny broth (LB) medium grow to an optical density (OD) of 1 at 600 nm. At this point 0.5 mM IPTG were added for induction and bacteria were kept on 37°C for 3 h. Coomassie control staining revealed a clear band corresponding to IpaA (70 kDa) with a GST-tag (26 kDa) at around 100 kDa (Fig. ?? C). Cells were pelleted and lysed in 3 ml binding buffer by sonicating at least three times for 30 s with 30 s rest on ice in the cold room (phenylmethylsulfonyl fluoride (PMSF) is not stable and stocks of 10 – 100 mM in isopropanol were kept at 4 – 8°C). After centrifugation at 10.000 g for 10 min an insoluble pellet, containing the GST-tagged IpaA formed at the bottom of the tube and was resuspended in binding buffer for washing. Sonication and centrifugation were repeated twice until the final pellet was solubilized in binding buffer containing 6 M urea. Dialysis o/n at 4°C against 1 M urea in 5 l dialysis buffer containing 10% glycerol was necessary for refolding of IpaA and followed by at least 2 h dialysis against storage buffer. Before usage, dialysis tubes (Membra-Cell MC18 Cat. No. 300589260) were cut into pieces of 3 cm and boiled for 5 min with 20 μ l 0.5 M EDTA in 2 ml ddH₂O. The solution was discarded and washed three times for 5 min with ddH₂O. After repeating boiling and washing once more, dialysis tubes were boiled in ddH₂O for 10 min and stored at 4°C. For the dialysis, the tubes were handled with sterile forceps and assembled using 5 ml dialysis capsules (Micro Dialysis Capsules QuixSep). Prior to usage, storage buffer was exchanged to hypotonic F-buffer 4.12 using a PD-10 desalting column (Amersham Biosciences Cat. No. 17-0851-01).

Binding buffer

500 <i>mM</i>	NaCl
200 <i>mM</i>	Tris-HCl pH 7.9
0.1 %	Triton-X
5 <i>mM</i>	imidazole
2 <i>mM</i>	PMSF
1 <i>x</i>	protease inhibitor cOmplete Ultra

Table 4.9: Binding buffer

Dialysis buffer

150 <i>mM</i>	NaCl
10 <i>mM</i>	Tris-HCl pH 7.5
10 <i>mM</i>	EDTA
1.0 %	β -mercaptoethanol
0.02 %	NaN ₃
10 %	glycerol

Table 4.10: Dialysis buffer

4.1.5 Production of hypotonic cell lysates

Two 10 *cm* culture dishes of confluent phoenix (human embryonic kidney 293 (HEK 293)) cells were transfected with 20 μ g DNA (section 4.2.4) and grown for 3 days with daily change of medium. As cells were super-confluent they could be detached by pipetting rigorously with 10 *ml* PBS, even without extra addition of EDTA. They were spun down at 1.000 *g* for 5 *min* at 4 °C and resuspended in 2 *ml* ice-cold hypotonic F-buffer. Cells were treated for at least 3 *min* with a glass homogenizer (Dounce) and centrifuged at 16.000 *g* for 10 *min* in the cold-room. The supernatant was aliquoted into 400 μ l and stored at –80 °C for multiple weeks.

4.1.6 Ultracentrifugation assay for F-actin binding

All steps involving protein lysates were done on ice or in the cold-room at 4 °C. Lysates with and without IpaA were prepared according to Tab. 4.13 and Tab. 4.14. Actin from rabbit muscle at a concentration of 1 *mg/ml* in ddH₂O (Sigma Cat. No. A 2522) was used. As a control, 30 μ l of each sample was denatured with 10 μ l 4 *x* Laemmli buffer for 5 *min* at 95 °C. The rest of the mixture was kept on ice for 30 *min* and centrifuged in a Beckmann TLA-45 centrifuge for 30 *min* at 125.000 *g*. For each sample 45 μ l of supernatant were denatured with Laemmli buffer. All remaining supernatant was sucked off carefully using a pipett tip

Storage buffer

150 <i>mM</i>	NaCl
10 <i>mM</i>	Tris-HCl pH 7.5
0.1 <i>mM</i>	EGTA
0.1 <i>mM</i>	EDTA
1.0 %	β -mercaptoethanol
0.02 %	NaN ₃
15 %	glycerol

Table 4.11: Storage buffer

Hypotonic F-buffer

20 <i>mM</i>	Tris-HCl pH 7.5
2 <i>mM</i>	NaCl
0.2 <i>mM</i>	EGTA
0.5 <i>mM</i>	DTT
0.02 %	NaN ₃
2 <i>x</i>	protease inhibitor cOmplete Ultra

Table 4.12: F-buffer

and the remaining pellet was resuspended in 50 μ l 1 *x* Laemmli buffer. For each fraction (total, supernatant and pellet) 20 μ l were loaded on a PAA gel and analysed by western blotting as described in section 4.1.3. Depending on protein concentration, the lysates had to be diluted 1 : 5 or 1 : 10 to avoid over-exposure during western blot analysis.

Mixture containing no IpaA (total 400 μ l)

20 μ l	KCl (1 M)
20 μ l	ATP (10 <i>mM</i>)
16 μ l	actin
200 μ l	hypotonic lysate
144 μ l	hypotonic F-buffer

Table 4.13: Lysate without IpaA

Mixture containing IpaA (total 400 μ l)

20 μ l	KCl (1 M)
20 μ l	ATP (10 mM)
16 μ l	actin
200 μ l	hypotonic lysate
44 μ l	hypotonic F-buffer
100 μ l	IpaA

Table 4.14: Lysate with IpaA

4.2 Cell culture methods**4.2.1 Handling of mouse embryonic fibroblast and telomerase immortalized human myometrial cells**

Standard cell culture conditions were achieved by an incubator permanently kept at 37 °C and 5 % CO₂. For mouse embryonic fibroblasts (MEF), Dulbecco's Modified Eagle Medium (DMEM) supplemented with 10 % fetal bovine serum (FBS) and 1 x streptomycin/penicillin (s/p) (growth medium) was used; for human myometrial cells a mixture of 1 : 1 of DMEM and Ham's F12 nutrient mixture was used. Cells were regularly split using 1 ml of trypsin for a medium cell culture flask after washing with 10 ml PBS. Approximately 5 min were enough for the cells to detach before resuspension in pre-warmed growth medium. To store cells for a longer period of time, they were resuspended in cold freezing medium (Tab. 4.15), aliquoted to 1.5 ml in cryo tubes and immediately transferred to a -80 °C freezer from where they could be transferred to a liquid nitrogen tank after full freezing. Cells thawed in a water bath at 37 °C and immediately transferred to pre-warmed growth medium. To remove dimethylsulfoxide (DMSO), cells were pelleted by centrifugation of 300 g for 5 min and resuspend them in growth medium.

Freezing medium

70 %	growth medium
10 %	DMSO
30 %	FBS

Table 4.15: Freezing medium

4.2.2 Generation of a clonal vinculin knockout cell line

Our lab received isolated fibroblastoid cells from genetically modified mice, in which the vinculin gene were flanked by two loxP sites (named $\text{vinc}^{f/f}$) (originally generated by Clare Waterman and Ingo Thievensen). Immortalization of mouse embryonic fibroblasts (MEFs) was achieved by adenoviral transduction of the SV40 large T-antigen. To generate clones, cells were seeded at a low density in a 10 *cm* cell culture dish and grown until separated clusters of multiple cells appeared. They were picked under a cell culture hood using a light microscope and directly transferred to 96-wells with trypsin for 5 – 10 *min*. After detachment, cells were transferred into a 24-well with 1.5 *ml* growth medium and split into small cell culture flasks. Clonal cell lines were analyzed by light microscopy and the cells with fastest growth rate which showed large FA and cell size (clone No. 2) were used for all further experiments ($\text{vinc}^{f/f}$). To generate vinculin knockout cells the $\text{vinc}^{f/f}$ cells were transduced with Cre recombinase and sorted by fluorescence-activated cell sorting (FACS). Single clones were picked as described before. The clone with the most similar morphological features to the original $\text{vinc}^{f/f}$ cell line was selected (clone No. 2-2) and is hereafter called $\text{vinc}^{-/-}$.

4.2.3 Transient transfection of cDNA constructs using Lipofectamine

To transfect fluorescent constructs into $\text{vinc}^{-/-}$ cells, the Lipofectamine 2000 Reagent was used (Invitrogen, Cat. No.11668-019). Target cells were seeded in a 6-well at 70 – 90 % confluency and were allowed to adhere for at least 2 *h* before medium was changed to 2 *ml* growth medium without s/p. For each sample 250 μl Opti-MEM were mixed with 10 μl Lipofectamine 2000 reagent. A second tube containing 250 μl Opti-MEM and 4 μg of the desired cDNA was prepared. Both tubes were left to incubate in the cell culture hood for 5 *min* before they were mixed and incubated for another 20 *min*. The total mixture of 500 μl was added dropwise to the cells. After 6 *h* the medium was changed to normal growth medium containing antibiotics. Cells were analyzed within 24 – 48 *h* after transfection.

4.2.4 Retroviral infection using the Phoenix cell system

For many applications, especially biochemical analysis, transiently transfected cells are unsuitable and a stable expression is needed. Our system of choice was the Phoenix (HEK 293) cell line which has been described in [126]. Prior to infection two 10 *cm* cell culture dishes of phoenix cells were seeded at 80 % confluency for each construct in growth medium which was exchanged to 7 *ml* growth medium containing 3.5 μl 50 *mM* of the lysosome

inhibitor chloroquine before transfection. The plasmid DNA was precipitated using calcium chloride (CaCl_2) and mixed dropwise with HBS while vortexing according to Tab. 4.16. After 8 h medium on the Phoenix cells was changed to 7 ml fresh growth medium. On the next day, the retroviral supernatant was collected and 8 μl of polybrene are added, medium on Phoenix cells is exchanged to fresh growth medium. The supernatant was sterile filtered and added to previously seeded target cells. Medium exchange and addition of supernatant were repeated three more times at approximately 12 h. After the infection, cells were sorted for high expression levels using FACS with a FACSAria cell sorter IIu (BD Biosciences). Gates were chosen to ensure equal mean expression level for different cell lines. Alternatively, infected cells can be challenged by puromycin treatment for 72 h at a concentration of 2 $\mu\text{g}/\text{ml}$ in growth medium.

Phoenix cell infection mixture

20 μg	plasmid DNA
61 μl	CaCl_2
add to 500 μl	ddH ₂ O

add 500 μl 2 x HBS while vortexing

Table 4.16: Phoenix infection mix

HBS pH 7.0

280 mM	NaCl
50 mM	Hepes
1.5 mM	$\text{Na}_2\text{HPO}_2 \times 2 \text{H}_2\text{O}$

add up to final volume ddH₂O

Table 4.17: HBS

4.3 Molecular biological methods

4.3.1 General remarks on cloning of cDNA constructs

Before cloning, a strategy for each construct was designed using the virtual cloning software Lasergene (DNASTAR) and plasmid maps were used throughout the whole process to control for fragment sizes and to check sequencing results. Each cloning step involved digestion of DNA by suited enzymes (New England Biolabs GmbH (NEB)) and dephosphorylation of the vector followed by gel electrophoresis and extraction from agarose gel. The extracted

DNA was ligated, transformed into competent *Escherichia Coli* (*E. Coli*) cells and single clones were picked from bacterial plates and checked by control digestion and sequencing.

DNA fragments were either amplified by Polymerase Chain Reaction (PCR) as described in section 4.3.2 or subcloned directly by enzymatic cutting of an existing DNA. As a vector either the pBlueskript (pBSK) vector or modified versions of the pLPCX vector were used. Those modifications included alterations of the multiple cloning sites (pLPCXmod cloning site 5'-BglIII-ApaI-HindIII-EcoRI-BamHI-XhoI-NotI-3'), deletion of the NotI cutting site (pLPCXmod Δ N) or deletion of the cytomegalovirus (CMV) promoter (modified pLPCX (pLPCXmod) Δ CMV). Plasmid DNA from sources outside the lab also was contained in pEX, pLL and pCAG vectors, but those were not used directly for cloning.

4.3.2 Protocol for normal, overlap extension and mutagenesis PCR

PCR is a standard method to modify DNA, e.g. by insertion of digestion sites, stop codons or mutations. Controlled temperature gradients are used to denature DNA strands and amplify pieces between so-called primers, which consist of short oligonucleotide strands that bind specifically to the DNA strands. In general, the protocol for touchdown-PCR (Tab. 4.19) with a PCR mix (Tab.4.18) containing primers, dNTPs, template DNA and Pfu Ultra polymerase was used.

PCR mix

5 – 20 ng	template DNA
5 μ l	10 x reaction buffer
4 μ l	dNTP (2.5 mM)
2 μ l	forward primer (5 pmol)
2 μ l	reverse primer (5 pmol)
1 μ l	Pfu Ultra polymerase
add to 50 μ l	ddH ₂ O

Table 4.18: PCR mix

For tension sensor and control constructs, it was necessary to create an insertion, in the middle of the cDNA by overlap extension PCR. Two products A and B were generated by two independent PCRs and are purified on an agarose gel and used as input for a third PCR. In addition to the standard forward (F) and reverse (R) primers forward (Fi) and reverse (Ri) insertion primers coding for the insertion fragment and 25 – 35 nucleotides down- or upstream of the insertion site were generated. For PCR A primers F and iR are used, for

Touchdown PCR

Step	time	temperature	
1	3 min	95 °C	initial denaturation
2	20 s	95 °C	denaturation
3	20 s	68 °C	primer annealing
4	15 s/kbp	72 °C	elongation
5	20 s	95 °C	denaturation
6	20 s	60 °C	primer annealing
7	15 s/kbp	72 °C	elongation
8	5 min	72 °C	final elongation
9	∞	4 °C	store

Steps 2-4: repeat 8 times, always reduce annealing temperature by 1 K
Steps 5-7: repeat 30 times

Table 4.19: Touchdown PCR

PCR B primers iF and R are used at standard concentrations. The final PCR C uses primers F and R as well as both products A and B as templates according to Tab. 4.20.

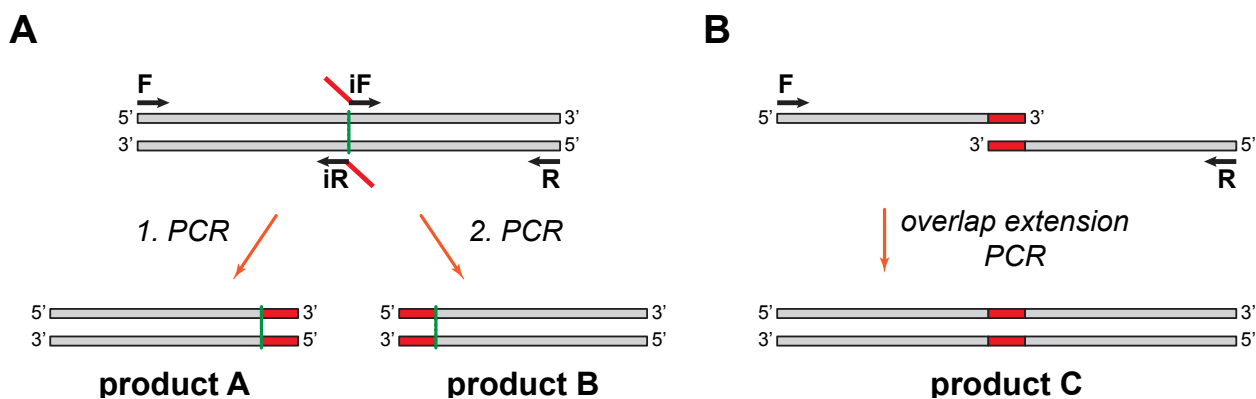


Figure 4.1: Schematic view of overlap extension PCR To generate tension sensor constructs an overlap extension PCR was used. Strands of cDNA are shown in gray and the resulting modified sequence is shown in red. **A.** In the first step two different PCRs generate product A and B by using the indicated primers. **B.** The overlap extension PCR fuses both products to the final outcome (C) which contains the modified sequence. In case of tension sensor cloning this is the insert for the linker. Figure taken from [105].

To introduce or correct mutations, we used site directed mutagenesis according to instructions of the QuikChange II kit (Agilent Technologies, Cat. No. 200523). Primers were designed according to manufacturers guidelines and 125 ng of each were added to the PCR mix. A modified PCR program has to be used as circular and not linearized DNA is amplified and compared to the touchdown PCR a longer elongation time but no temperature reduction is needed (Tab. 4.22). The final PCR product was cooled for 2 min on ice and 1 μ l of the restriction enzyme DpnI was added to each reaction tube, mixed, and incubated for

PCR mix overlap

5 – 20 ng	template DNA
5 μ l	10x reaction buffer
4 μ l	dNTP (2.5 mM)
2 μ l	forward primer (5 pmol)
2 μ l	reverse primer (5 pmol)
1 μ l	DNA template A (50 ng/ μ l)
1 μ l	DNA template B (50 ng/ μ l)
1 μ l	Pfu Ultra polymerase

add to 50 μ l ddH₂O

Table 4.20: Overlap PCR

1 h to digest the parental supercoiled and methylated double stranded DNA (dsDNA). For transformation, 1 μ l was added to 50 μ l of cooled competent cells and left to incubate on ice for 30 min followed by 45 s heat-shock in a water bath at 42 °C and 2 min on ice. 500 μ l of pre-heated LB were added to the transformation reaction and incubated at 37 °C for 1 h with constant shaking. The entire transformation reaction was split and 250 μ l were plated on ampicillin containing bacterial plates. The final plasmid had to be completely sequenced as the PCR reaction could have introduced mutations in the insert as well as into the backbone. For sequencing 15 μ l of ddH₂O containing 1 μ g and 2 μ l of primer (10 pmol) were sent to MWG Biotech.

QuikChange mutagenesis PCR mix

5 – 50 ng	template DNA
5 μ l	10x reaction buffer
4 μ l	dNTP (2.5 mM)
125 ng	oligonucleotide primer 1
125 ng	oligonucleotide primer 2
1 μ l	Pfu Ultra polymerase

add to 50 μ l ddH₂O

Table 4.21: QuikChange PCR mix

4.3.3 DNA digestion, gel electrophoresis, extraction, ligation and transformation

Cutting sites for restriction enzymes were either present in the cDNA of our constructs or could be inserted via normal or overlap extension PCR. Digestion mix contained cutting

QuikChange mutagenesis PCR

Step	time	temperature	
1	30 s	95 °C	initial denaturation
2	30 s	95 °C	denaturation
3	1 min	68 °C	primer annealing
4	1 min/kbp	72 °C	elongation
5	∞	4 °C	store

Steps 2-4: repeat 12 times for point mutation, up to 18 times for multiple amino acid changes

Table 4.22: QuikChange PCR

enzymes and DNA in the appropriate buffer (Tab. 4.23). Incubation times and temperatures were determined by the Double Digest Finder tool from New England Biolabs website (<https://www.neb.com/tools-and-resources/interactive-tools/double-digest-finder>). For some enzymes with very different properties like *ApaI* and *NotI* two sequential digests lead to better results than one double digest. In case of only a single enzyme digest and to enhance ligation efficiency the vector DNA was dephosphorylated by incubating it two times 30 min at 37° with 1 µl calf-intestinal-phosphatase (CIP).

Digestion mix

1 – 2 µg	DNA
3 µl	10 x reaction buffer (enzyme specific)
1.5 µl	20 x bovine serum albumin (BSA) (2 mg/ml)
1 µl	enzyme A (10.000 units/ml)
1 µl	enzyme B (10.000 units/ml)
add to 30 µl	ddH ₂ O

Table 4.23: Digestion mix

After digestion and desphosphorylation, DNA was immediately loaded onto an agarose gel to separate DNA from enzymes and avoid unspecific effects. Electrophoresis gels were prepared by dissolving 1% agarose in tris-acetic acid-EDTA (TAE) buffer (Tab. 4.24) and boiling it in a microwave for 2 min at 900 W. The gel was cooled down to 50 – 60 °C, 3,8-diamino-5-ethyl-6-phenylphenanthridiniumbromid (ethidium bromide) was added and it was poured into molds with a 10-well comb. DNA was mixed with 10x loading buffer (Tab. 4.25) and 15 µl of 1 kb DNA standard (NEB, Cat. No. N3232) was used as reference. Gels were run at 80 – 120 V for 20 – 40 min. DNA with intercalated ethidium bromide was visualized on a Mini BenchTop UV Transilluminator (UVP, Cat. No. M-10E95-0180).

10 x TAE buffer

242 g	Tris
57.1 ml	acetic acid
100 ml	EDTA (0.5 M, pH 8.0)
add to 1 l	ddH ₂ O

Table 4.24: TAE buffer**Loading buffer**

52 %	glycerol
60 mM	EDTA
0.1 %	bromphenol blue
0.1 %	xylene cyanol
0.2 %	orange G
add to 50 ml	ddH ₂ O

Table 4.25: Loading buffer

DNA bands of desired sizes were cut out with a razor blade and transferred to Eppendorf tubes. For extraction of DNA from agarose gels, the mi-Gel Extraction Kit (metabion, Cat. No. mi-GEL50), which is based on binding of DNA to silica-based membranes in chaotropic salts, was used according to the standard protocol. Purified vector and insert were ligated at a ratio of 1 : 3 for 1 h at RT (Tab. 4.26). Amount of vector and insert was estimated from intensity of bands, normalized by DNA size.

Ligation mix

0.01 – 0.03 ng	vector DNA (e.g. 1 μ l)
3 x molar excess	insert DNA
1.5 μ l	T ₄ DNA ligase buffer
1 μ l	T ₄ DNA ligase
add to 15 μ l	ddH ₂ O

Table 4.26: Ligation mix

DNA was transformed into competent bacteria, 6 μ l of ligase mix were added to 60 μ l of freshly thawed competent XL-1 cells and incubated on ice for 20 min. Bacteria were heat shocked at 42 °C for 45 s followed by 2 min on ice. 700 μ l pre-warmed LB medium free of antibiotics was added and the mixture was incubated at 37 °C for 1 h with gentle shaking before plating 500 μ l on bacterial plates (15 g of agar for 1 l of LBamp). After o/n incubation at 37 °C single colony clones were picked and transferred into 3 ml LBamp medium in

bacterial growth tubes and grown shaking at 37 °C until they reached the required optical density after 8 – 16 h.

Lysogeny broth (LB) medium

10 g	NaCl
10 g	tryptone-peptone
5 g	yeast extract
add to 1 l	ddH ₂ O

Table 4.27: LB medium

Plasmid DNA was isolated from *E. Coli* cells to check for positive clones by control digest or sequencing. To generate stocks of DNA for later use in transfection, 200 ml LBamp were grown o/n. To prepare small amounts of DNA, I used a mi-Plasmid Miniprep Kit (metabion AG, Cat. No. mi-PMN50) while large amounts for later use in cell culture were generated using a Midi/Maxiprep Kit (NucleoBond Xtra plasmid purification, Macherey-Nagel Cat. No. 74010.50). Bacteria were be stored for longer times by adding 600 µl of 86 % glycerol to 500 µl of fresh bacteria and freezing it to –80 °C.

4.3.4 Cloning of vinculin and metavinculin constructs

To generate fluorescently tagged constructs of vinculin and metavinculin, we used human vinculin cDNA (Accession number BG284191, Clone ID: IRATp970Go639D) and changed mutations (E142K, C636G and A901P) with a QuikChange Mutation Kit (section 4.3.2). Insertion sites (5' ApaI/3' XbaI) were generated by PCR and vinculin cDNA (1-1066) was cloned into a pBSK vector. To insert the metavinculin tail an oligonucleotide encoding amino acids 874-1134 was synthesized (MWG Biotech) and cloned in using 5' AvrII/3' XbaI sites. All C-terminal fluorophores (venusA206K, mCherry, enhanced blue fluorescent protein (EBFP)) were amplified by PCR with (5' XbaI/3' NotI) sites and cloned into pBSK-vinculin or -metavinculin. The 5' ApaI/3' NotI sites were used to move the constructs into a modified pLPCX (pLPCXmod) vector to generate the final constructs vinculin-venus (VV), metavinculin-venus (MV), vinculin-mCherry (VC), metavinculin-mCherry (MC), vinculin-EBFP (VB), metavinculin-EBFP (MB).

4.3.5 Cloning and insertion of tension sensor constructs

We choose the proline rich linker region in the middle of vinculin and metavinculin and inserted tension sensors or internal fluorophores between aa 883 and aa 884. To this end we

generated a pBSK with a modified multiple cloning site (MCS) lacking NotI (5'-ApaI-XhoI-Sall-ClaI-EcoRI-BamHI-XbaI-3') and cloned in a linker containing a 5'Sall and a 3'NotI site by overlap extension PCR using primers C30 and C31. The linker construct was transferred into pLPCXmod and internal fluorophores and tension sensor peptides venus-flagelliform peptide (F40)-mCherry and YPet-HP35-mCherry were inserted using '5XhoI/NotI3' sites which lead to destruction of the Sall site. For activation sensor constructs the tail of vinculin or metavinculin and a fluorophore was amplified by PCR and added to constructs with internal fluorophores via 5'NotI/NotI3'. Cardiomyopathy related mutations Arg975Trp, Ala934Val, the HTI mutations (N773A, E775A) and other point mutations were generated by QuikChange Mutagenesis. To introduce mutations of multiple amino acids, as in the case of metavinculin DDY945NTL, overlap extension PCR was applied.

4.4 Biophysical methods

4.4.1 Handling of micropatterns

During this project two different kinds of micropatterns were used: cross-shaped PEG-coated micropatterns fabricated by Dr. Julien Polleux and commercially available triangular patterns (CYTOOchips Y-M-FN, Cat. No. 10-011-10-18). Both were printed by photolithography onto 20 x 20 mm boro-silicate glass. Custom made patterns had to be coated before use with 10 µg/ml FN o/n at 4 °C. Glass slides were mounted, facing with the micropattern upwards, onto plastic microscopy dishes with a hole in the bottom of 15 mm diameter, using a two-component dentist glue (Picodent Twinsil, Cat. No. 200 2.1) mixed at a ratio of 1 : 1 immediately before use. The glue was only attached to the rim of glass slides and they were left to dry for at least 20 min at RT. Non-confluent cells were trypsinized and seeded onto the dishes in DMEM supplemented with 10% FBS where they attached and started to spread after approximately 30 min. Adherence on custom made patterns was in general not as specific as on commercial ones and we used DMEM supplemented with only 1% FBS to prevent cells from extensive formation of ECM. After 6 – 8 h cell started to migrate from custom-made patterns whereas they remained seated on cytoo-micropatterns even after o/n seating. However, it is advisable to image cells within 4 – 6 h after seeding as they will start to divide on the micropattern.

4.4.2 Production of soft substrates for TFM

I prepared soft substrates of varying stiffnesses and embedded fluorescent microspheres for use in TFM. They were either coated homogeneously with FN or micropatterns were transferred onto the gel. The main steps involved in this process are activation of coverslips surface, preparation of hydrophobic slides, preparation of PAA gels and activation of the PAA surface or embedding of micropatterns. The protocol has been modified based on [111] and a protocol from the MBL summer course 2007 by Gardel, Vesna and Jacobson.

To clean cover slips (#1.5, 25 mm, Menzel, Cat. No. CB00250RA1), they were stirred with soap in distilled water (dH₂O) for 30 min, rinsed with dH₂O and washed three times 30 min with dH₂O. Finally, they were rinsed with EtOH and stored in 100 % EtOH. Before use, cover slips were flamed and placed into a teflon rack. The rack was put in a beaker with 2 % 3-aminopropyltrimethoxysilane diluted in 200 ml dH₂O and stirred for 10 min. For activation of cover slips by amination, the racks were rinsed multiple times with dH₂O and incubated with 500 ml dH₂O for 10 min. Racks were removed with a tweezer and remaining water drops were blown away. Cover slips were dried at 37 °C for 30 min and cooled down to RT. Racks were immersed in 0.5 % glutaraldehyde solution in 200 ml PBS and stirred for 10 min on a shaker. As before, cover slips were washed with three changes of dH₂O and left in a fresh beaker for 10 min. Cover Slips were dried at RT, again with prior removal of big water drops. It is advisable to prepare large amounts of slides at once (e.g. 20 - 40) as they can be stored in a dust free environment for up to one week or in a dessicator for up to two months.

Hydrophobic cover slips were prepared immediately before PAA polymerization. Cover slips were flamed and placed in a teflon rack. To make them hydrophobic, single slides were dipped in a beaker filled with 50 ml of water repellent Rain-X solution (Rain-X, Cat. No. 80222200). Excess solution was removed with a Kimwipe, the cover slip was then immersed in ddH₂O and dried again with a fresh Kimwipe. In case of stains, the procedure was repeated. Hydrophobic cover slips were distributed on an even surface for preparation of PAA gels.

For PAA gels of different final Young's modulus E the acrylamide to bis-acrylamide (bis-AA) ratios were altered according to Tab. 4.28. Exact stock solutions for 8 kPa and 15 kPa PAA gels are shown as examples in Tab. 4.29 and 4.30. Each time 445 μ l of PAA stock solution were degased in a vacuum chamber for 20 min. I added 52 μ l ddH₂O containing fluorescent

beads (e.g. 10 μl FluoSpheres Carboxylate-Modified Microspheres 0.2 μm or 3 μl FluoSpheres Carboxylate-Modified Microspheres 0.04 μm , Cat. No. F8806 and F8789) to the PAA gel and mixed it on a wheel.

For polymerization of PAA gels 0.5 μl TEMED and 2.5 μl fresh 10% APS were added to the stock solution, mixed and 15 μl liquid PAA gel solution was pipetted immediately onto the hydrophobic slides. Aminated cover slips were placed on top and left to polymerize in the dark for 20 *min*. Hydrophobic slides were detached carefully with a razor blade. All slides with holes, damages or uneven PAA surface were discarded. Slides with PAA can be stored up to several days in a 6-well with 3 *ml* ddH₂O on top in the dark at 4 °C.

In order to cross-link FN on PAA surfaces they need to be functionalized. I used ultraviolet (UV) induced cross-linking of sulfo-SANPAH. A fresh vial of sulfo-SANPAH (Fisher Scientific, Cat. No. 10474005) was equilibrated to RT to avoid moisture condensation and powder was resuspend in 2 *ml* DMSO. Aliquots of 2 *mg* (80 μl) were shock-frozen in liquid nitrogen and stored at -80 °C.

Due to the low stability of sulfo-SANPAH the next steps were performed at 4 °C. Excess water was removed from PAA slides with a Kimwipe. One aliquot containing 2 *mg* of sulfo-SANPAH was diluted in 920 μl cold ddH₂O and 200 μl were immediately pipetted onto each slide. Gel surfaces were exposed to strong UV light for 5 *min* at a distance of 8 *cm* (Hanau Quarzlampe Typ 5261 Fluotest UV 210 W). A brief washing step in a 500 *ml* beaker filled with ddH₂O removed excess sulfo-SANPAH.

Drops of 50 μl of 1 *mg/ml* FN solution were pipetted onto stretched parafilm and a cover slip was placed on top to react o/n at 4 °C. Residual water was removed from the glass surface which was mounted with the PAA gel facing upwards onto a microscope dish (35 *mm*) with a hole in the bottom (20 *mm*) using two-component glue. A drop of PBS was placed on top of the PAA gel to avoid drying. Next, dishes were filled with growth medium and cells were seeded at 50% confluency for 4 – 6 *h*. Immediately before acquisition medium was changed to 1 *ml* imaging medium.

To generate PAA gels with regularly shaped micropatterns we used either commercial (CYTOOchips Y-M-FN, Cat. No. 10-011-10-18) or custom-made (courtesy of Dr. Julien Polleux) glass slides coated with FN (section 4.4.1). To transfer the FN, micropatterned glass slides were added on top of the PAA gel during polymerization, thus avoiding both the amination and the cross-linking step.

Young modulus and PAA ratios

E(kPa)	PA %	bisAA %
5.0	4	0.3
6.5	5	0.15
8.0	5	0.225
15.3	8	0.15
21.0	8	0.225

Table 4.28: PAA ratios

Stock solution for 8 kPa PAA gel

625 μ l	40 % acrylamide
562.5 μ l	2 % bis-acrylamide
3.262 ml	ddH ₂ O

adding up to a total of 4.450 ml

Table 4.29: PAA 8kPa

4.4.3 Fabrication of PDMS chambers for cell stretching

PDMS stretch chambers with 50 kPa stiffness were fabricated in collaboration with the group of Prof. Rudolf Merkel from Forschungszentrum Jülich [110]. Chambers from PDMS (Sylgard 184 Elastomere Kit, VWR Cat. No. 634165S) are produced by filling liquid basis oil and cross-linking reagent into polystyrol molds and curing it in an oven. Handling of unpolymerized PDMS is only possible with clean room gloves (Kimtech, G2993) as dirt particles from conventional latex gloves interfere with the polymerization. Touching the polished surface at the inner part of polystyrol molds with sharp objects will immediately lead to scratches and they can only be cleaned with a Kimwipe soaked in isopropanol.

A mixture of 1 : 40 cross-linker and basis oil was weighed with a high-precision scale using approximately 5 g of PDMS per chamber. Both ingredients were mixed thoroughly with a plastic spatula for 5 min and degased in a glas vacuum chamber for 20 min. The mixture was poured into cleaned molds and excess PDMS was removed. Cross-linking took place in an bench-top incubator adjusted to 60 ± 0.1 °C for 16 ± 1 h. Chambers were cooled down for 30 min before they were carefully removed from the mold and stored for up to four weeks. Before use stretch-chambers were coated o/n with 550 μ l of 10 μ g/ml FN and cells are seeded at 50 % confluency in 1 ml growth medium for 4 – 6 h. Immediately before acquisition medium was changed to 1 ml imaging medium.

Stock solution for 15 kPa PAA gel

1000 μ l	40 % acrylamide
450 μ l	2 % bis-acrylamide
3.00 ml	ddH ₂ O

adding up to a total of 4.450 ml

Table 4.30: PAA 15kPa

4.5 Microscopy methods

4.5.1 Characterization and spectra of used fluorophores

Our genetically encoded tension sensors use either the FRET-pair venusA206K/mCherry or YPet/mCherry. The spectra of these fluorophores overlap (see Fig. 4.2) leading to an efficient energy transfer and a theoretical Förster radius of about 5.8 nm. To enable parallel observation of other expressed constructs, we utilized an EBFP-tag which allows spectral separation of signal and thus does not interfere with FRET measurements. For fluorescent beads and membrane dyes the far-red range of the spectrum above 600 nm was the appropriate choice (CellMask Deep Red Plasma Membrane Stains, Invitrogen Cat. No. C10046). Dyes from the Alexa series were best suited for immunostainings and were excited and detected as shown in Tab. 4.31.

Fluorophore	Excitation	Emission
venus	512 nm	525 – 565 nm
YPet	509 nm	525 – 565 nm
mCherry	587 nm	600 – 640 nm
EBFP	405 nm	475 – 515 nm
Alexa568	568 nm	580 – 620 nm
Alexa647	647 nm	660 – 700 nm
Cell Mask Orange	554 nm	565 – 595 nm
Cell Mask Deep Red	649 nm	660 – 700 nm
Fluospheres Crimson	633 nm	645 – 695 nm
Fluospheres Dark Red	660 nm	670 – 700 nm

Table 4.31: Microscope settings for used fluorophores and dyes

4.5.2 Preparation of dishes and handling of cells for live cell microscopy

For live cell microscopy glass cover slips (#1.5, 25 mm, Menzel, Cat. No. CBoo250RA1) were glued into holed (15 mm - 20 mm) plastic dishes using Picodent Twinsil at a ratio of 1 : 1

and incubated with $10\ \mu\text{g}/\text{ml}$ FN for $1\ \text{h}$ at RT or o/n at 4° . To allow cell adhesion but not spreading, dishes were incubated for $2\ \text{h}$ with $0.01\ \%$ PLL and $1\ \text{h}$ with $1\ \%$ BSA. For sterilization UV-light was applied for at least $20\ \text{min}$.

4.5.3 Time-correlated single photon counting (TCSPC)-fluorescence lifetime imaging microscopy (FLIM)

Fluorescence lifetimes was measured using a confocal microscope (Leica TCS SP5 X) running the LAS AF Litesoftware equipped with a pulsed white light laser (WLL) (NKT Photonics) with a repetition rate of $80\ \text{MHz}$ at $50\ \%$ of full power. Single photons were detected using FLIM X16 $78\ \text{MHz}$ TCSPC detector (LaVision Biotech, Germany) running the Inspector software (Fig. 4.2 B). I used a bandpass filter $545/30$ (AHF Analysentechnik, Germany) to measure lifetimes of venus or YPet. Images were acquired at a scanning velocity of $400\ \text{Hz}$, a spatial resolution of 512×512 pixels and resulting image field coverage of $123.02 \times 123.02\ \mu\text{m}^2$ when using a $63\times$ water objective (HCX PL APO CS, $NA = 1.2$). This lead to a pixel dwell time of $4.8\ \mu\text{s}$ and a total time of $2.64\ \text{s}$ per frame. The detection covered a time window of $12.24\ \text{ns}$ after the excitation pulse with a temporal resolution of $0.08\ \text{ns}$. In a typical experiment, 20 frames were required to collect sufficient amount of photons from a single cells. For each experimental condition 15 – 20 cells were recorded and each experiment was repeated at least 4 – 5 times. On average only one out of several hundred laser pulses led to a detected photon and shot noise statistics could be assumed for photon arrival times. For each experiment, the lifetime of only the donor fluorophore venus was determined and used for the calculation of FRET efficiencies. To visualize the instrument response function (IRF), the lifetime of the fluorophore Rose Bengal ($\tau < 500\ \text{ps}$) was used [127].

4.5.4 Fluorescence recovery after photobleaching (FRAP) on micropatterns

FRAP is a technique to determine turnover rates of molecules by recording recruitment of unbleached molecules to a previously bleached region. Cells expressing fluorescently tagged FA proteins were seeded for $4 - 6\ \text{h}$ on X- or Y-shaped micropatterns as described in 4.4.1 where they formed regular and stable FAs at the corners. Images were acquired on a Leica SP8 confocal laser scanning microscope equipped with a $63\times$ water objective (HCX PL APO, $NA=1.2$) and a 37°C heating chamber. The bleaching region was defined in the LAS AF Lite Software to completely cover half of one corner while the other half was used as a reference to exclude movement. Signal from all non-adjacent FAs was used to

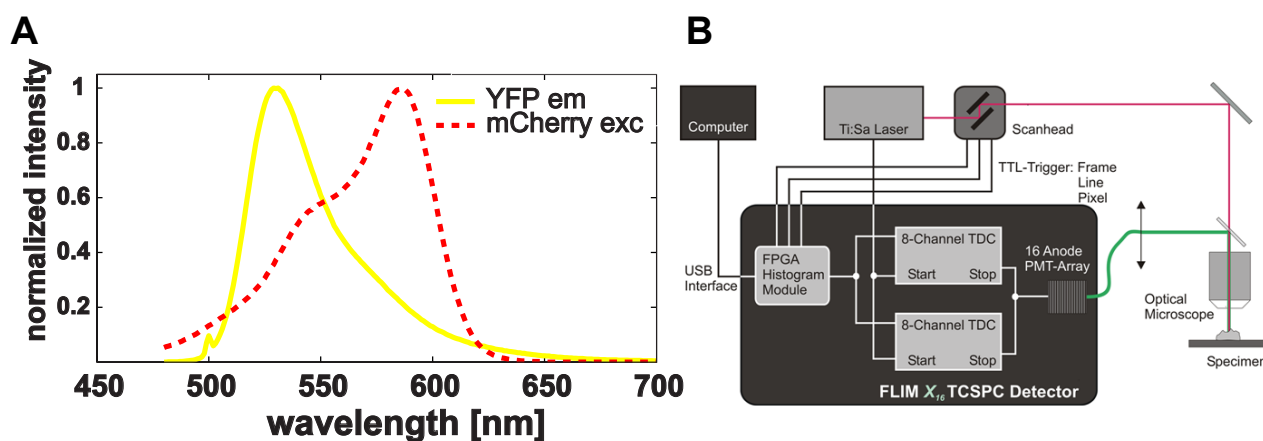


Figure 4.2: Set-up for TCSPC-FLIM measurements **A.** Example spectra for a FRET pair consisting of YFP and mCherry. The emission spectrum of YFPs (yellow) like venus and YPet overlaps with the excitation spectrum of mCherry (dashed red line). Therefore energy transfer occurs between both fluorophores and they are a suited FRET pair. **B.** Schematic drawing of TCSPC-FLIM detection. The detection system for TCSPC-FLIM consists of a rectangular 4×4 array of 16 PMT detectors which are connected to two parallel 8-channel time-to-digital converters (TDCs). These TDC are triggered by the pulsed laser and lead signals further on to an field programmable gate array (FPGA) histogram counting module and via an USB-2 interface to the computer. Figure taken from <http://www.lavisionbiotec.com/flim-x16-tcspc-detector.html> (September 2016)

correct for photobleaching. Two pre-bleach images were recorded at 2 % of total laser power at 514 nm for venus and 405 nm for EBFP fluorophore before bleaching the ROI with 100 % laser power for about 1 s. Fluorescence recovery was imaged during the next 300 – 500 s with 20 s intervals at 2 % laser power. f

4.5.5 Imaging of substrates for TFM

Imaging of TFM slides took place at a Leica TCS SP 8 confocal laser scanning microscope with a motorized x-y positioning stage and an incubation chamber at 37 °C. The system was connected to a perfusion pump. For better imaging of thick substrates, I used a long distance objective (HC PL APO 40x/1.10 W CORR C S2, working distance 0.65 mm). Data precision was set to 12 bit and the spatial resolution was 60 nm per pixel. For excitation of crimson fluorescent beads (FluoSpheres Carboxylate-Modified Microspheres, life technologies, Cat. No. F8806, diameter 200nm, 625/645 nm) we used the 633 nm laser line at 1 % of its maximum power and recorded the signal with a Leica hybrid detector (HyD) from 645 – 695 nm (pinhole 1 AU).

Cells were handled and seeded as described in section 4.4.2. Control images for VV or MV were taken with the 514 nm laser line at 5 %, the surface of the PAA gel was determined

in the transmission light channel. From the surface, the z-position was shifted $2\ \mu\text{m}$ into the gel and images of PAA gel were acquired at a scan rate of 50 Hz. Beads need to have a gaussian profile of at least 10 pixel width to be tracked by the automated algorithm. When 4 – 5 brightfield, FA, and bead images were recorded, I added 1 ml of killing buffer 4.32 via the perfusion pump. After complete cell lysis, the correct z-position was adjusted for a second gel image; small shifts in x or y were corrected by the analysis program.

Killing buffer for TFM experiments

50 mM	Tris-HCl pH 7.6
150 mM	NaCl
1 %	Triton-X 100
1 %	SDS

Table 4.32: Killing buffer

4.5.6 Immunofluorescence staining

Cover slips for immunofluorescence were treated similar to dishes for live cell microscopy (section 4.5.2), except that instead of gluing them to a plastic dish we placed glass slides of 10 mm into 24-wells. For standard experiments cells were seeded at the required confluency for 120 min, quickly washed with PBS and fixed in 3.7% paraformaldehyde (PFA) for 10 min at RT. Fixation solution was sucked off and washed three times for 5 min with PBS before blocking with 2% BSA and 0.1% Triton-X 100 in PBS for 1 h at RT. In case of fluorescently tagged protein in the sample all incubation steps were performed in the dark. The first antibody was diluted in blocking solution (Tab. 4.33) according to Tab. 10.5 and incubated for 1 h. After three washing steps with PBS (each 5 min) the second antibody was diluted in blocking solution and incubated for 1 h. To stain the actin cytoskeleton, we added phalloidin during this step. The last washing step (three times 5 min with PBS) was followed by mounting in ProLong Gold antifading reagent (Life Technologies, Cat. No. P36934), which were dried o/n at RT. Slides were imaged within a week and kept on 4° for long time storage.

Immunostaining blocking solution

0.1 %	Triton-X 100
2 %	BSA in PBS

Table 4.33: Blocking solution

5 Data analysis

5.1 Image analysis and feature extraction

5.1.1 Analysis of cell and focal adhesion (FA) size and shape

During this project I programmed versions v01-v04 of the FA analysis toolbox. This toolbox is optimized for the fast and easy import and comparison of microscopy data from live cell images and immunostainings. Images were imported into Matlab in the format .tif, .lif, .lsm or as matrices and ROIs were manually set to exclude cytoplasmic background and disturbing signal from adjacent cells. Next, data was blurred by a mean filter with a 3×3 pixel kernel. A three-level multi-Otsu thresholding algorithm was applied to the data (<http://www.biomecardio.com/matlab/otsu.html>). The highest intensities were defined as FA signal and converted into a binary image. After automatic filling of holes connected components were defined on this binary image using the Matlab **bwconncomp()** function. According to biological definitions only objects with a physical size larger than $1 \mu m^2$ are included into the analysis and recognized as FA. Parameters were extracted according to definitions of the Matlab **regionprops()** function and include total FA area per cell, size and orientation of single FA, number of FA per cell, and FA eccentricity.

To determine cell size and eccentricity, we analyzed live cell images from cells treated with a cell-permeable dye (CellMask Deep Red Plasma Membrane Stains, Invitrogen Cat. No. C10046) or immunostainings of the F-actin cytoskeleton with phalloidin (Alexa Fluor 647 Phalloidin, Life Technologies Cat. No. A22287). When only data from FA stainings was available, as in the case of TFM data, cell size was determined manually using ImageJ.

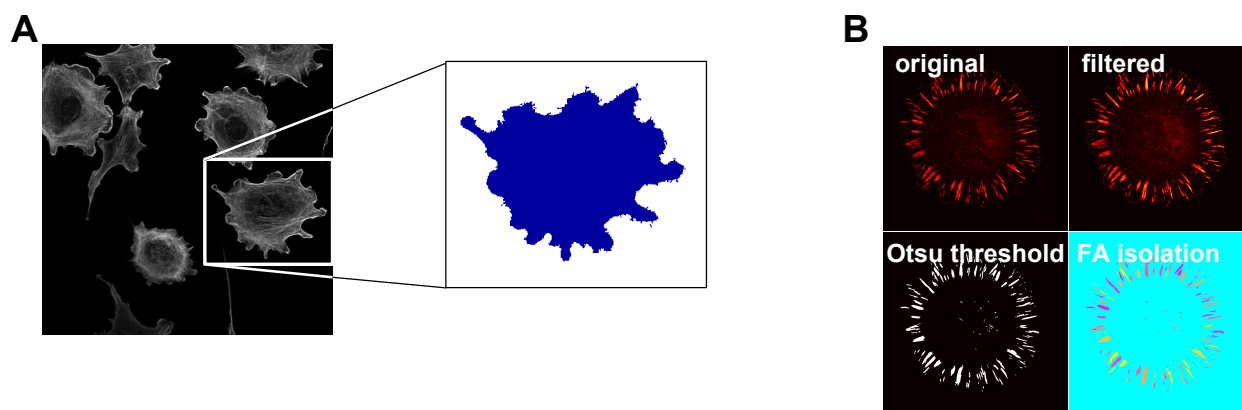


Figure 5.1: Extraction of cell size and eccentricity **A.** Even small features of cell circumference can be extracted from actin immunostainings. **B.** Steps of the FA extraction algorithm: original data is filtered with a mean filter of kernel 3×3 and subjected to a three-level Otsu threshold. After conversion into a binary image the FA isolation takes place. Different colors mark individual FA. For each of them parameters like are, eccentricity and orientation are defined.

5.2 Evaluation of TCSPC-FLIM data

5.2.1 Set-up of import routines and data structure

After recording, time-correlated single photon counting (TCSPC)-fluorescence lifetime imaging microscopy (FLIM) data can be analyzed by the Inspector software, however, the limitations of this program are very obvious as calculation of lifetimes requires multiple steps, has to be done individually for each cell, and does not allow for further options like feature extraction. Therefore I developed a user-friendly platform for data analysis which could be managed without detailed knowledge about programming and allowed for flexible handling of large data amounts in the range of terabyte (TB). Data can be loaded into the program either via a graphical user interface (GUI) or by directly declaring a variable with the paths leading to the data. A standard FLIM experiment, as described in section 4.5.3, contains 20 cells with 15-20 measurement repeats for each cell. The default setting for temporal resolution was 0.08 ns leading to 153 frames per image. Data was stored in the .tif file format and could be accessed via the MATLAB `imread()` function. In a first step, all frames are loaded in and repeats for one cell are merged. The total number of photons for each time step is counted and photons from all time points and repeats are added up. This gives a histogram of the number of photons in each time bin. The loading procedure is robust, but very time consuming and could be optimized by using sparse matrix notation.

5.2.2 Fitting of lifetime curves and definition of FRET efficiency

Prior to fitting, all histograms were aligned by determining the curve maximum for the whole experiment and shifting single traces accordingly. The IRF was measured using Rose Bengal dye, which has a very short lifetime ($\tau < 500$ ps, Fig. 5.2 B) [127]. I also determined the influence of excluded timepoints counted from the minimum of the histogram on the lifetime fit (Fig. 5.2 A). Lifetimes were determined from the photon count histograms by tail-fit using the Matlab `fit()` function with the non-linear least square method with equal weight for all data points. The equation reads

$$f(t) = a e^{-t/\tau} + b \quad (5.1)$$

with amplitude a , lifetime τ and background b . To evaluate the goodness of fit, we calculated the coefficient of determination R^2 and excluded data with $R^2 < 0.98$. Fitting of bi-exponential decays was implemented, but introduced additional degrees of freedom and complicated the interpretation of data. To describe relative differences in FRET fitting of a monoexponential decay is sufficient as there should be a monotonic relation between energy transfer and lifetime. The absolute FRET efficiency E is defined as

$$E = 1 - \frac{\tau_{DA}}{\tau_D} \quad (5.2)$$

with donor lifetime τ_D and lifetime of donor in presence of the acceptor τ_{DA} . The function `expMERGE()` can be used to compare and combine FRET efficiencies from various experiments, constructs and analysis steps described in 5.2.3.

5.2.3 Analysis of FLIM data

For interpretation of biological data the separation of fluorescent signal from different spatial regions is important. In the first step of data import a fluorescence image is generated from all photons which arrived during the measurement, independent of their arrival time. This image was used as an input for our thresholding routines and features were extracted.

The resulting binary mask from the FA analysis program was multiplied with the imported FLIM image and all further calculations of lifetime used photons from this area. In general, we restricted our data analysis to photon counts from FAs which were defined according to section 5.1.1. The user could further restrict the analysis to FA of a special size, shape or intensity value. For projects from other group members and collaboration partners I

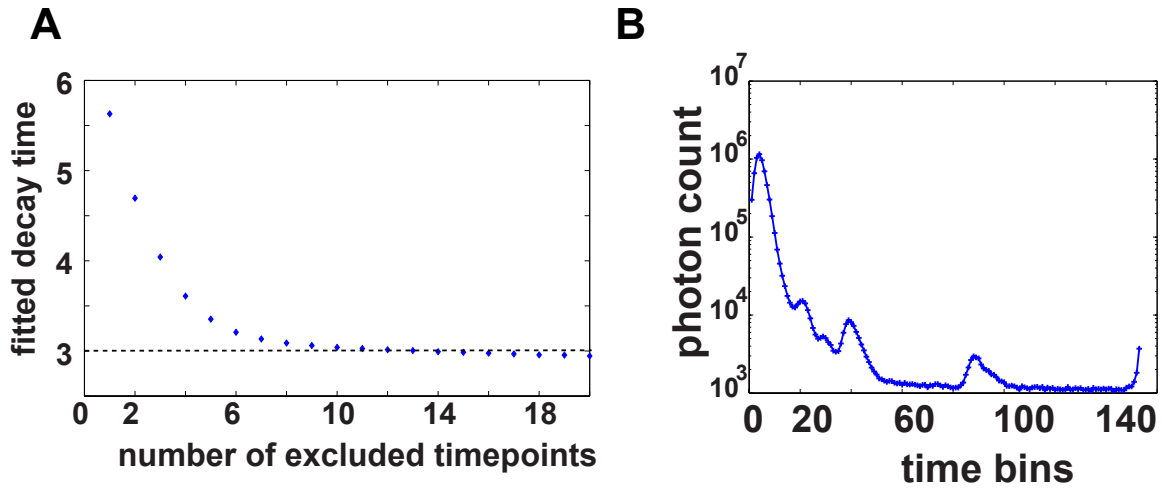


Figure 5.2: Cut-off value for monoexponential tail fit **A.** Dependence of fitted lifetime on number of time points from the minimum of the photon count histogram for a typical venus control measurement. **B.** Signal from Rose Bengal dye representing the IRF (logarithmic scale). After the first peak, the signal strongly decays and oscillations occur at around 40 and 90 time bins (logarithmic scale).

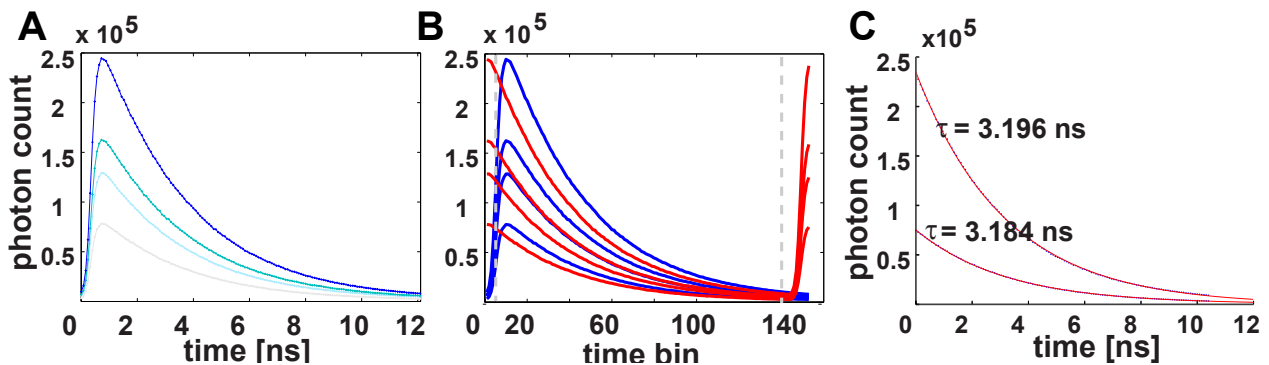


Figure 5.3: Fitting of lifetime **A.** Example raw data from venus lysates of different concentrations. **B.** Histogram traces (blue) are shifted (red) to the maximum of the mean of all traces. For the tail fit only signal 5 bins away from the maximum until bin 135 are taken, as indicated by the dashed gray bars. **C.** Monoexponential fit of curve with highest and lowest photon count. One advantage of the TCSPC-FLIM method is its independence from signal intensity.

adjusted for the analysis to biological structures like kinetochores, hemidesmosomes, or signal from *Drosophila* larvae.

To produce images of spatial distribution of lifetimes they were determined by a non-fitting based approach through calculation of the mean photon arrival time. For this analysis photons from 4×4 pixel regions were combined.

5.2.4 Statistical testing and considerations of measurement errors

Data for TS measurements is presented as boxplots indicating the 25 % and 75 % percentile. The median is visualized by a red bar and whiskers reach to 2.7 times the standard deviation σ . In the text, mean FRET values \pm the variance are given. Bar plots show the mean value and indicate variance by a red whisker. In some cases which are explicitly stated, the SEM is shown instead of the variance.

The following tests were implemented to test statistical significance, the null-hypothesis are:

Kolmogorow-Smirnov-Test [kstest2()]: both data vectors are from the same continuous distribution.

Two-sample t-test [ttest2()]: both data vectors are from a normal distribution with same mean but can have different variances.

For all tests a significance level of $\alpha = 0.05$ was used. I decided to use the Kolmogorow-Smirnov test as a default because it does not require normality of the distribution. In my opinion, the t-test is not an appropriate choice, because the variance needs to be taken into account when comparing FRET data from TS constructs. Data for the same construct from at least 3 – 4 independent repeats was pooled. The lifetime of a protein tagged with only the venus fluorophore served as a control that donor lifetime does not change between measurement days.

Independent of the measurement precision, photon count statistics are limited by shot noise. A simulation of theoretical expected data precision was done by generating random numbers from a Poisson distribution with a mean value defined by a monoexponential decay with lifetimes and amplitudes comparable to experimental values. The detection range is limited to 12.4 ns and measurement precision is higher for shorter lifetimes. Indeed, the theoretical variance could already explain half of the variance for VV and vinculin head tension sensor (VHTS). As we expected, variations of TS constructs were significantly higher

than the shot noise, indicating that this sensor responds to biological factors and experiences varying forces across cells (Fig. 5.4 B,C).

5.3 Analysis of biophysical data

5.3.1 Fitting of FRAP curves

Fluorescence intensity data and regions of interest (ROI) were imported into ImageJ as .lsm or .lif files. The MacBiophotonics ImageJ plugin **FRAP profiler** performed automated analysis of the data and generated raw and normalized recovery curves. Data was imported into Matlab for further analysis. All traces that did not show bleaching to less than 20% of the initial fluorescence intensity were removed from the analysis, as well as movies showing a drift in the focus plane or movement of cells. Using the FA analysis algorithm, I tested that mean initial intensity levels of cells were not significantly different. Next, mean and variance of the normalized data was calculated and plotted against time after bleaching. I assumed a reaction-dominated model [64, 128] for the recovery and fitted the equation

$$f(t) = A(1 - e^{-k_{off}t}) \quad (5.3)$$

with rate constant k_{off} and mobile fraction A . The rate constant is connected to the half-life $\tau_{1/2}$ which we used to characterize the FRAP recovery curves by $\tau_{1/2} = \ln(2)/k_{off}$.

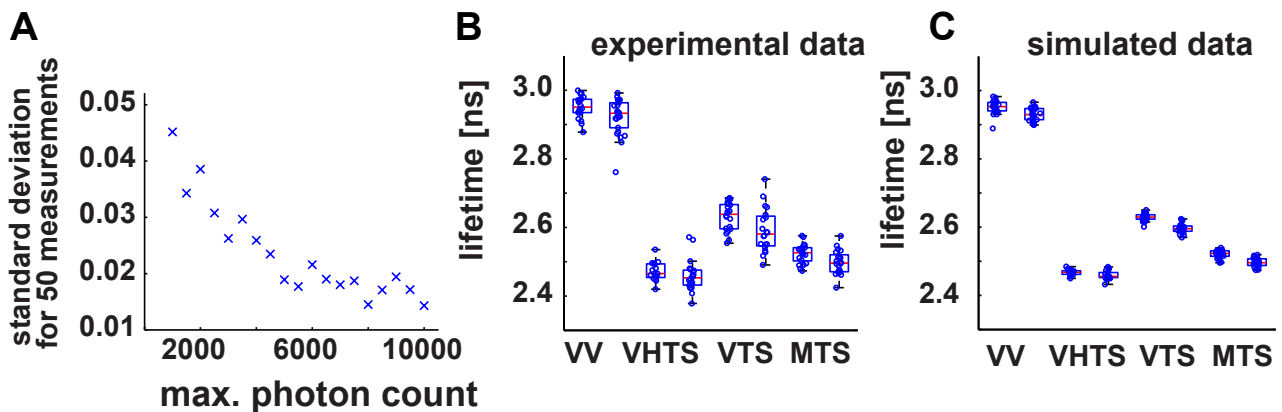


Figure 5.4: Analysis of variance in experimental data **A.** Averaged standard deviation for 50 simulated measurements. The variance shows a linear correlation with intensity and saturates at values of around 6.000 photons per measurement. **B.** Experimental data of fluorescence lifetimes for TS constructs and VV. Two experiments from consecutive days are shown next to each other, each dot corresponds to measurement from a single cell. **C.** Simulated data which takes shot noise into account, shows the theoretical limit of measurement precision.

5.3.2 Particle image velocimetry (PIV) and Fourier transform traction cytometry (FTTC)

Here, I will describe analysis of an experimental method, which determines the displacement field $\mathbf{u}(\mathbf{x})$ by tracking the position of fluorescent beads in compliant PAA gels before and after removal of cells using a particle image velocimetry (PIV) plugin for ImageJ. Bead images recorded before and after removal of cells were aligned using a template matching tool which calculates the normalized 2D cross-correlation coefficient (Fig. 5.5 A.- C.). Knowledge of the experimentally determined displacement field $\mathbf{u} = \mathbf{x}' - \mathbf{x}$ and the Green's function $\mathbf{G}(\mathbf{x}, \mathbf{x}') = \mathbf{G}(\mathbf{x} - \mathbf{x}')$ leads to an equation for traction forces $t(\mathbf{x})$.

$$\mathbf{u}(\mathbf{x}) = \int \mathbf{G}(\mathbf{x}, \mathbf{x}')t(\mathbf{x}')d\mathbf{x}' \quad (5.4)$$

This convolution integral can be inverted in Fourier space where it reads [108]

$$\tilde{\mathbf{t}}(\mathbf{k}) = \mathbf{G}(\mathbf{k})^{-1}\tilde{\mathbf{u}}(\mathbf{k}) \quad (5.5)$$

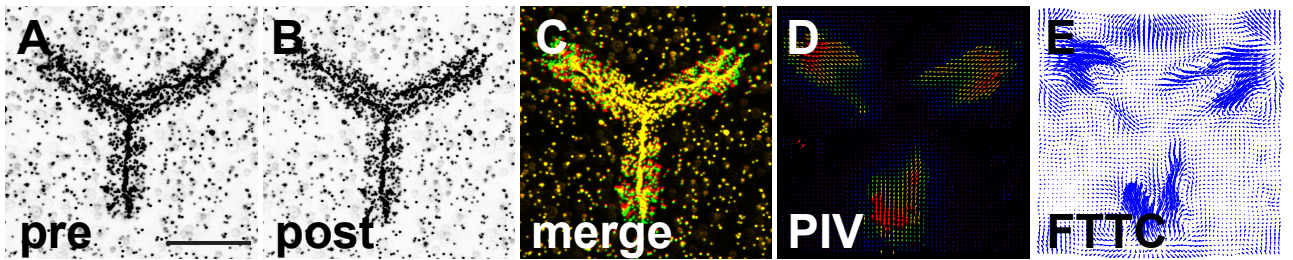


Figure 5.5: Traction force microscopy (TFM) analysis by FTTC **A.** Image of beads embedded in an elastic PAA gel. A cell is seeded on top of the Y-shaped micropattern leading to deformations of the gel. **B.** Bead image after releasing the cell-generated stress by addition of killing buffer. **C.** Aligned bead images (pre: red, post: green), showing areas of large overlap (yellow) and shifted beads. **D.** Displacement field $\mathbf{u}(\mathbf{x})$ determined from experimental data by PIV. **E.** Vector representation of the traction force field $\mathbf{t}(\mathbf{x})$ calculated by FTTC. Scale bar: $20 \mu\text{m}$

To solve equation 5.5, an algorithm from Benedikt Sabass [112] called Fourier transform traction cytometry (FTTC) was used. The experimental displacement field $\mathbf{u}(\mathbf{x})$ was smoothed and interpolated to a regular grid using a frequency cut-off rule. Next, a Fast Fourier transform (FFT) was applied and $\tilde{\mathbf{u}}(\mathbf{k})$ could be directly multiplied with the inverse Green's function $\mathbf{G}(\mathbf{k})^{-1}$. Determination of the Green's function is possible for the geometrical constraints of problem and more details are given in [112]. The resulting force field $\tilde{\mathbf{t}}(\mathbf{k})$ was back-transformed into real space.

The total strain energy per cell in pJ was now calculated from the single displacement vectors as [129]

$$U = \frac{l^2}{2} \sum_{n_1, n_2} \sum_{i=1,2} t_i(n_1, n_2) u_i(n_1, n_2). \quad (5.6)$$

I used the traction force reconstruction tool programmed by Benedikt Sabass [112] to calculate strain energies and traction forces from image data. For the analysis an interrogation window size of 128 pixels for PIV and a smoothing parameter, which determines the frequency cut-off for the FTTC, of $l_{smooth} = 10^{-6}$ were chosen.

6 Results

6.1 Establishment and characterization of vinculin and metavinculin expressing cell lines ($\text{vinc}^{-/-}$)

6.1.1 Stable expression of vinculin and metavinculin in vinculin knockout fibroblasts

The vinculin gene was deleted from $\text{vinc}^{f/f}$ cells as described in section 4.2.2 and I used retroviral infection to generate cells stably expressing vinculin-venus (VV) and metavinculin-venus (MV) constructs (sec. 4.2.4, Fig. 6.1 D). All cell lines adhered to fibronectin (FN) or collagen coated surfaces, however, $\text{vinc}^{-/-}$ proliferation rate was decreased. Western blotting confirmed the lack of vinculin in $\text{vinc}^{-/-}$ cells and re-expression of VV and MV similar to wildtype levels. Other core focal adhesion (FA) proteins like integrin-linked kinase (ILK), paxillin, talin or focal adhesion kinase (FAK) did not show alterations in their expression level (Fig. 6.3 A). The $\text{vinc}^{-/-}$ clone used for this study (clone #2-1, Fig. 6.1 B) does not show reduced size and FA morphology. However, it is important to note that other clones (e.g. clone #2-5, Fig. 6.1 C) with reduced size and even stronger proliferation defects were discarded as they might have accumulated additional mutations during immortalization and gene excision.

6.1.2 Metavinculin localizes to FA and rescues spreading defect caused by vinculin deletion

I analyzed protein localization by live cell imaging and immunostaining and found localization of VV as well as MV to FA, nascent adhesions and dorsal ruffles (Fig. 6.2 A). Size and shape of FAs were not significantly different between both cell lines, however, expression of vinculin-head-venus (VHV) lead to increased FA size (Fig. 6.2 B & Fig. 6.16 A-C). Paxillin staining confirmed the presence of FA in $\text{vinc}^{-/-}$ cells (Fig. 6.3 B). Analysis of cell

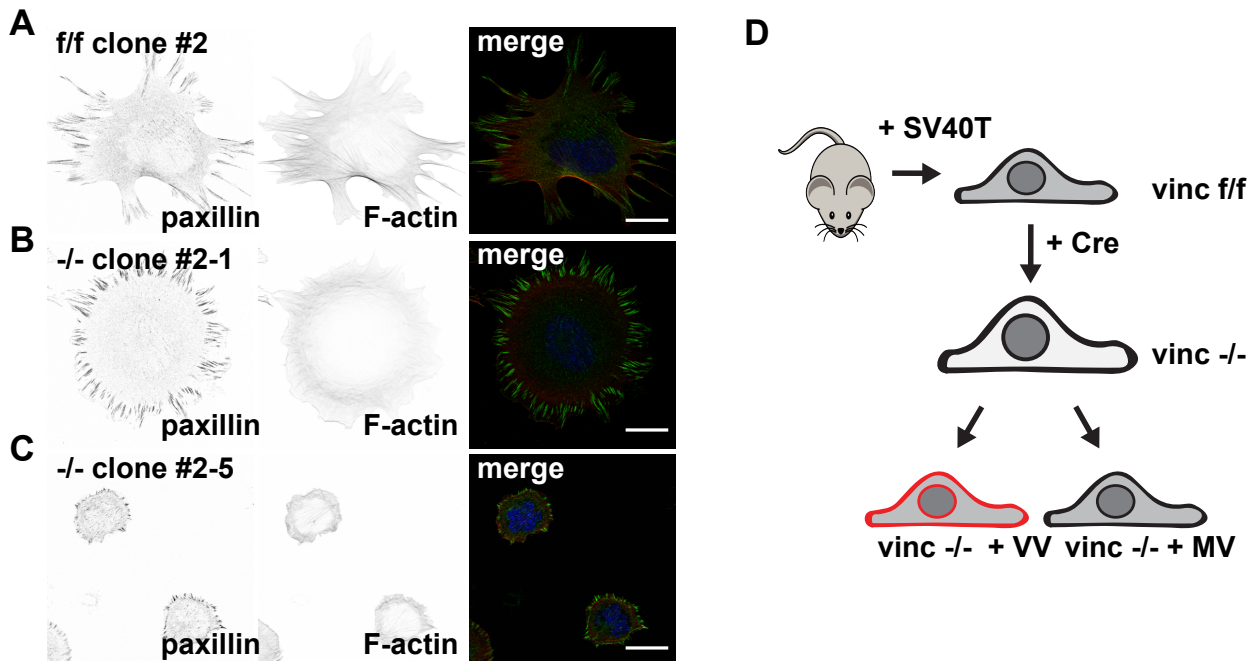


Figure 6.1: Generation of clonal *vinc*^{f/f} and *vinc*^{-/-} cell-lines **A.** Immortalized clonal cell line with a floxed vinculin gene (*vinc*^{f/f}). **B.** Clone from knockout cell line #2-1 which has been generated from *vinc*^{f/f} after addition of Cre and fluorescence-activated cell sorting (FACS). This cell line was used for all following experiments as it does not show impairments in cell or FA size. **C.** Clone #2-5 shows severe growth defects after deletion of vinculin by Cre. Some cells are polynucleated and FA size as well as proliferation is decreased. **D.** Schematic illustration of cell line generation. Cells are immortalized by SV40-T, treated with Cre and sorted. Constructs with a fluorescent tag are then introduced by stable or transient transfection. **A.-C.** All cells were seeded on 10 $\mu\text{g/ml}$ FN for 120 *min* and stained against F-actin (red) and paxillin (green), scale bar: 20 μm

morphology at different time points showed a delayed spreading of *vinc*^{-/-} cells, which is most prominent after 120 *min* and can be rescued by both VV and MV expression (Fig. 6.3 C). After several weeks in cell culture, the spreading defect of *vinc*^{-/-} decreased significantly. All measurements performed for this thesis use cells from early passages. These observations demonstrate that metavinculin can localize to FA in the absence of vinculin and can compensate the lack of vinculin with regard to cell spreading and adhesion.

To determine whether vinculin and metavinculin localization depends on actomyosin contractility, I treated cells with blebbistatin and Rho-associated protein kinase (ROCK) inhibitor Y-27632, which both lead to reduced FA size and VV or MV intensity (Fig. 6.4).

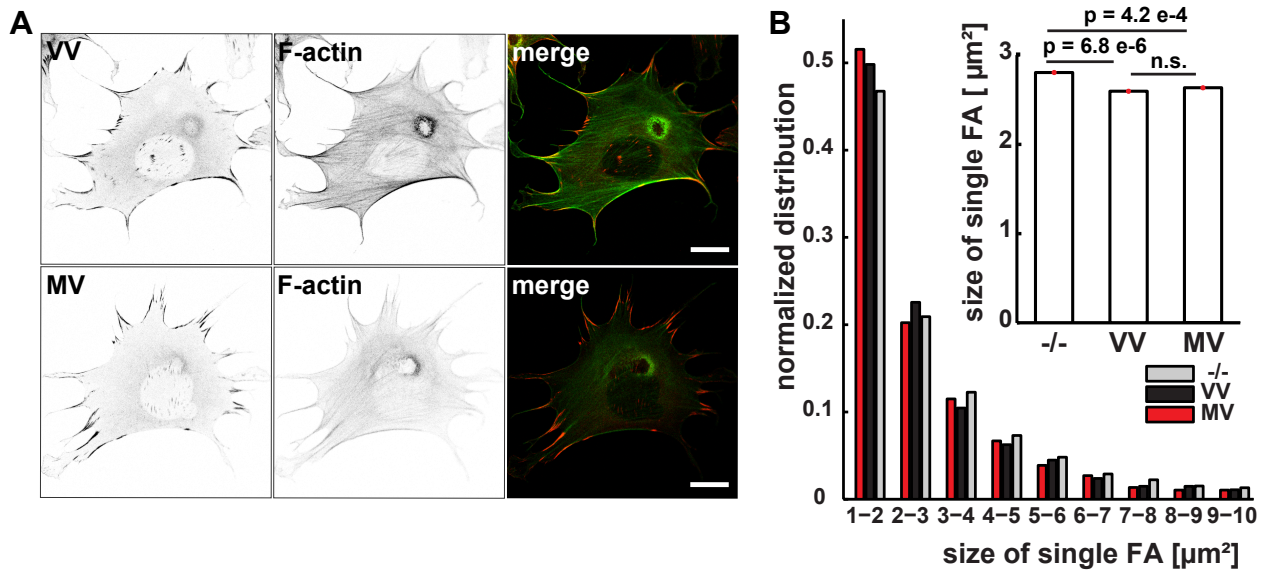


Figure 6.2: Localization of VV and MV constructs **A.** Immunostaining shows that both VV and MV localize to FAs, dorsal ruffles and nascent adhesions. F-actin: green, venus-tagged constructs: red, scale bars: 20 μm , cells seeded for 120 min on 10 $\mu\text{g}/\text{ml}$ FN. **B.** Detailed analysis of FA size in vinculin knockout (*vinc*^{-/-}) cells and rescue with VV and MV after 120 min on 10 $\mu\text{g}/\text{ml}$ FN. Histogram shows distribution of FA sizes in μm^2 . No difference between mean FA size of VV and MV is observed ($2.595 \pm 0.0006 \mu\text{m}^2$ vs. $2.634 \pm 0.0006 \mu\text{m}^2$) and sizes were slightly smaller compared to *vinc*^{-/-} which showed a higher amount of large FA $> 5 \mu\text{m}^2$ ($2.805 \pm 0.0006 \mu\text{m}^2$). Error is shown as SEM.

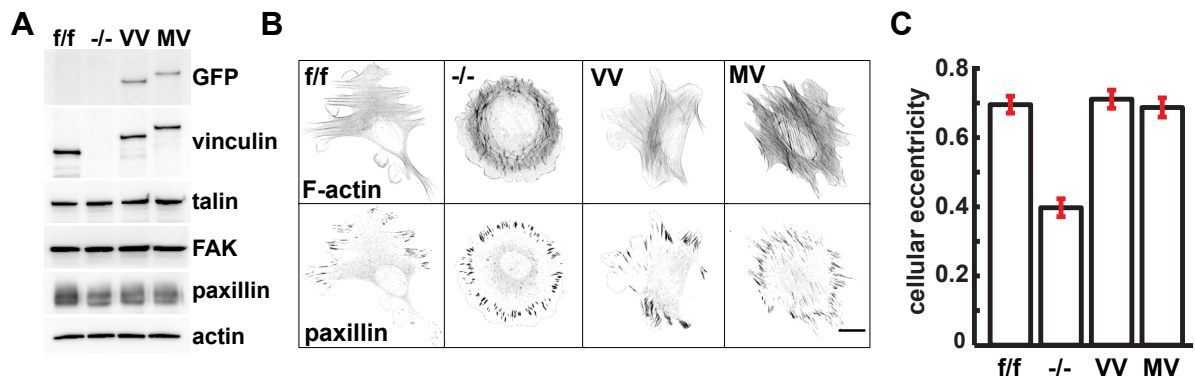


Figure 6.3: Rescue of spreading defect by VV and MV constructs **A.** Western blot of *vinc*^{*f/f*}, *vinc*^{-/-} cells and rescues with VV and MV against typical FA proteins. A monoclonal green fluorescent protein (GFP) antibody shows expression of fluorescent constructs and antibody against total vinculin confers expression levels similar to wildtype. No differences in the expression of talin, FAK, paxillin and actin are observed. **B.** Representative immunostainings after 120 min on 10 $\mu\text{g}/\text{ml}$ FN show rescue of the spreading defect in *vinc*^{-/-}. F-actin (upper row) and paxillin (lower row) signal, scale bar: 20 μm . **C.** Quantification of cellular eccentricity (*vinc*^{*f/f*}: 0.69 ± 0.24 , *vinc*^{-/-}: 0.39 ± 0.26 , VV: 0.71 ± 0.26 , MV: 0.68 ± 0.27) from three independent experiments with at least 20 cells per cell line.

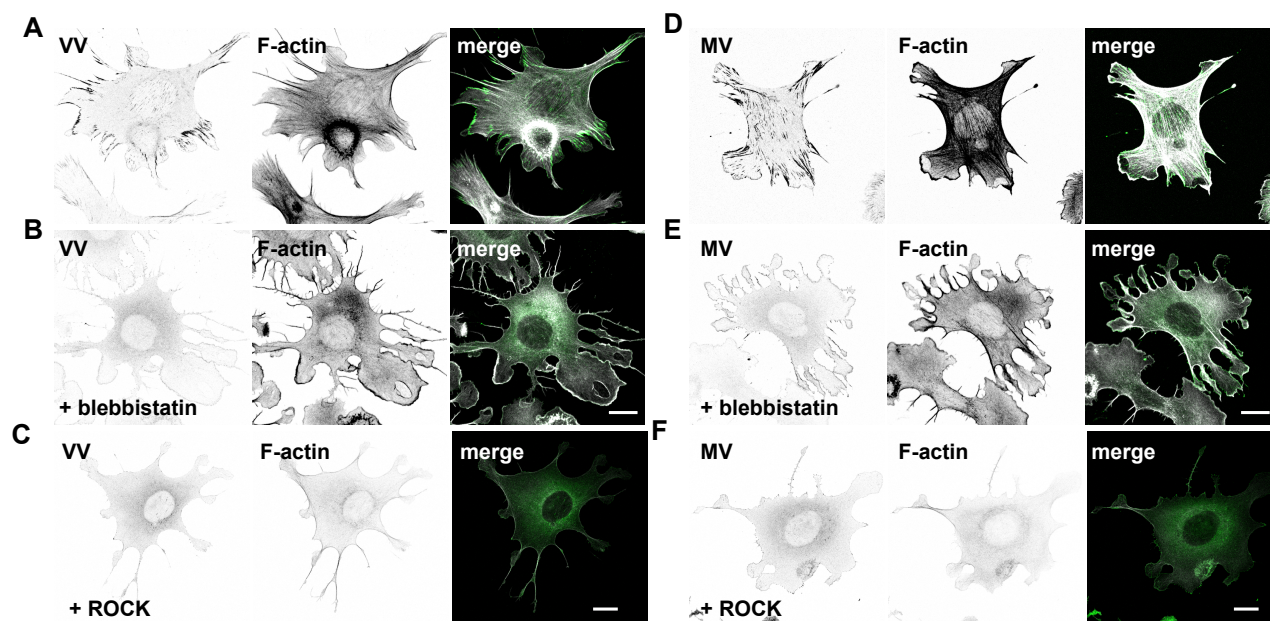


Figure 6.4: Treatment of cells with blebbistatin and ROCK inhibitor A. VV and D. MV control without blebbistatin. B. VV and E. MV treated with 30 μ M blebbistatin for 10 min. C. VV and F. MV cells treated with Y-27632 10 μ M for 10 min. Cells were seeded for 120 min on 10 μ g/ml FN, scale bar: 20 μ m

6.1.3 Fluorescence recovery after photobleaching (FRAP) reveals increased stability of metavinculin in FA

Protein turnover rates can be accessed by fluorescence recovery after photobleaching (FRAP) (see section 4.5.4). Vinculin turnover depends on FA size and subcellular position [130]. I seeded cells on X- or Y-shaped micropatterns to exclude these effects and ensure regular FAs with comparable sizes that do not change during the measurement (see section 4.4.1, Fig. 6.6 C). Bleaching of areas in the cytoplasm verified that the timescale of diffusion was much faster than for protein incorporated in FA and we controlled for comparable FA size and fluorescence intensities (Fig. 6.6 C).

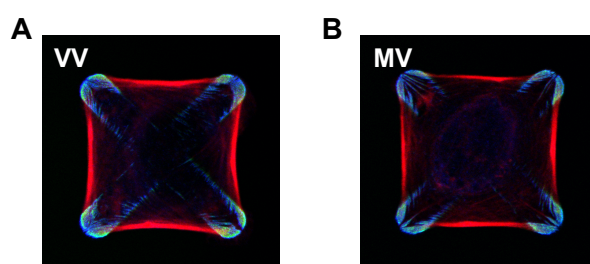


Figure 6.5: Immunostainings of cells on X-shaped micropatterns A. Vinculin knock-out cells expressing VV B. or MV. Both cell lines were seeded on X-shaped FN-coated micropatterns of 40 μm side length fabricated by Julien Polleux. The F-actin cytoskeleton is shown in red, FAs are indicated by signal of Venus tag (blue).

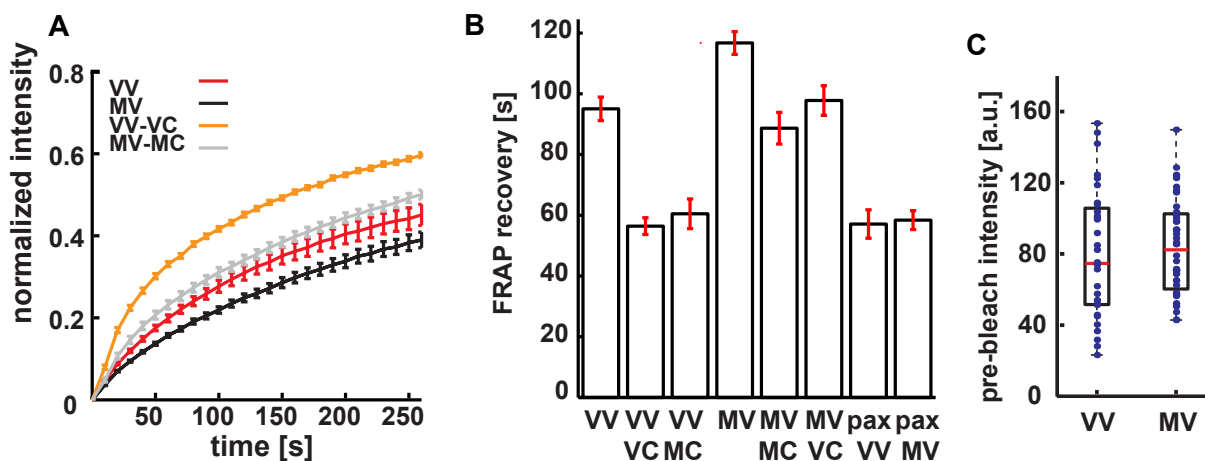


Figure 6.6: FRAP experiments on X-shaped micropatterns A. Fit of recovery curves for VV (red), MV (black), VV in presence of vinculin-mCherry (VC) (orange), MV in presence of metavinculin-mCherry (MC) (gray). B. Recovery rates τ_1 show faster turnover of VV compared to MV and no changes for paxillin turnover. C. Comparison of pre-bleach intensity from live cell images of FA show no significant differences between VV and MV.

Measurement of VV and MV expressing cells on X-shaped micropatterns revealed a slower turnover rate ($95.1 \pm 3.87 \text{ s}$ vs. $116.7 \pm 3.75 \text{ s}$) and decreased mobile fraction ($73 \pm 1.6 \%$ vs.

60 ± 1.7%) for metavinculin as compared to vinculin (Fig. 6.6 B). Co-expression of the same amount of vinculin or metavinculin protein with mCherry tag (VC and MC) resulted in faster turnover and even more pronounced difference between VV-VC and MV-MC cell lines (57.75 ± 2.55 s vs. 88.67 ± 5.22 s) (Fig. 6.6 A & B). Next, I measured VV in the presence of MC (and MV in the presence of VC), which resulted in turnover similar to VV-VC and MV-MC (VV-MC: 69.73 ± 5.58 s and MV-VC: 97.79 ± 4.89 s) (Fig. 6.6 A & B).

To confirm these observation, I repeated experiments with VV and MV expressing cell lines on commercial Y-shaped micropatterns (Cytoo) using a microscope with more sensitive detection and better temperature control, which enabled us to increase measurement time to 500 s. Again, metavinculin turnover was characterized by reduced turnover rates and the mobile fraction was significantly decreased (VV: 75.58 ± 4.33 s and 73.5 ± 1.3%, MV: 100.8 ± 8.26 s and 58.16 ± 1.25%) (Fig. 6.7 B). Increasing the degree of freedom by fitting a stretched exponential $f(x) = A \cdot (1 - \exp(-(t/\tau)^\beta))$ lead to a higher variance of both mobile fraction and lifetime. Assumption of two lifetimes $f(x) = A_1 \cdot \exp(-t/\tau_1) + A_2 \cdot \exp(-t/\tau_2)$ did not yield consistent results and only moderately influenced fit quality compared to fitting one effective lifetime.

To test the effect on other FA proteins, turnover of overexpressed paxillin-mCherry and talin-1-EBFP was measured in presence of VV or MV. No significant alterations in the respective lifetimes or mobile fractions were observed (paxillin VV: 57.1 ± 4.7 s or MV: 58.5 ± 3.12 s (Fig. 6.6) and talin-1 VV: 102.1 ± 4.7 s or MV: 94.97 ± 11.13 s, $p = 0.68$ (Fig. 6.7)). Together, the data indicate that metavinculin has significantly reduced turnover rates in FAs.

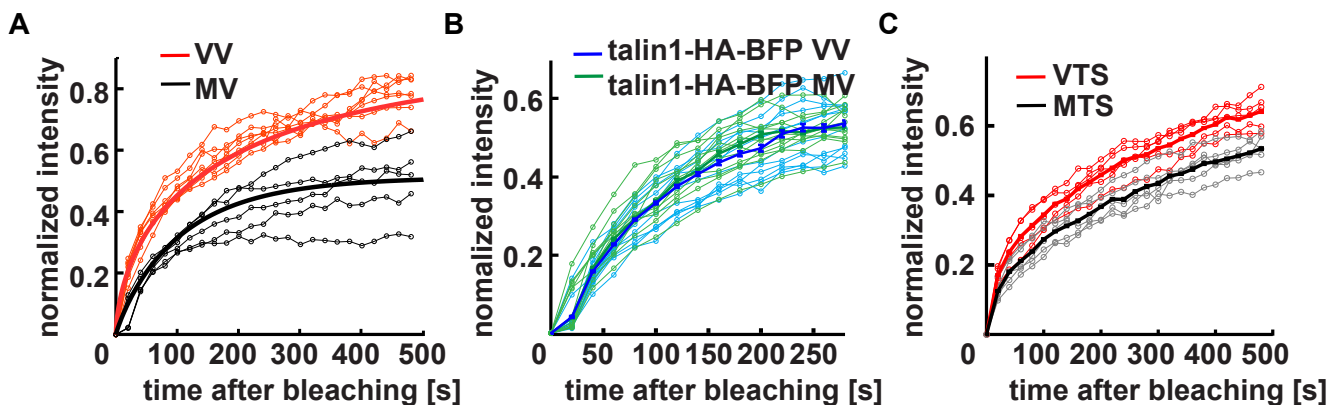


Figure 6.7: FRAP experiments on Y-shaped micropatterns **A.** Recovery curves for VV (red) and MV (black) show higher mobile fraction and faster turnover for vinculin. **B.** Turnover and mobile fractions for talin1-HA-EBFP do not depend on co-expression of VV (blue) or MV (green). **C.** Control experiments for tension sensor (TS) constructs reveal slower turnover for metavinculin tension sensor (MTS) (black) than for vinculin tension sensor (VTS) (red) and decreased mobile fraction of MTS.

6.2 Analysis of metavinculin interaction partners

6.2.1 Mass-spectrometry identifies changes in interaction with talin

To explain the decreased turnover rates of metavinculin in FA, I searched for changes in binding or interaction partners which could explain the enhanced stability of metavinculin. A first screen of the interactome was performed in cooperation with the group of Prof. Matthias Mann from Max Planck Institute (MPI) of Biochemistry, Martinsried, using quantitative co-immunoprecipitation mass spectrometry. Tagged constructs were pulled down using a GFP antibody which also recognizes the yellow fluorescent protein (YFP) venus. Untransfected *vinc*^{-/-} cells served as negative control. Interestingly, an increased interaction (about 5-fold) of talin-1 with metavinculin was observed (Fig. 6.8 B). Other proteins enriched in the metavinculin sample were structural maintenance of chromosomes 1A (SMC-1A) and protein LLP homolog (Lph) (Fig. 6.8 C), which were not further analyzed because they have been not described to localize to FAs.

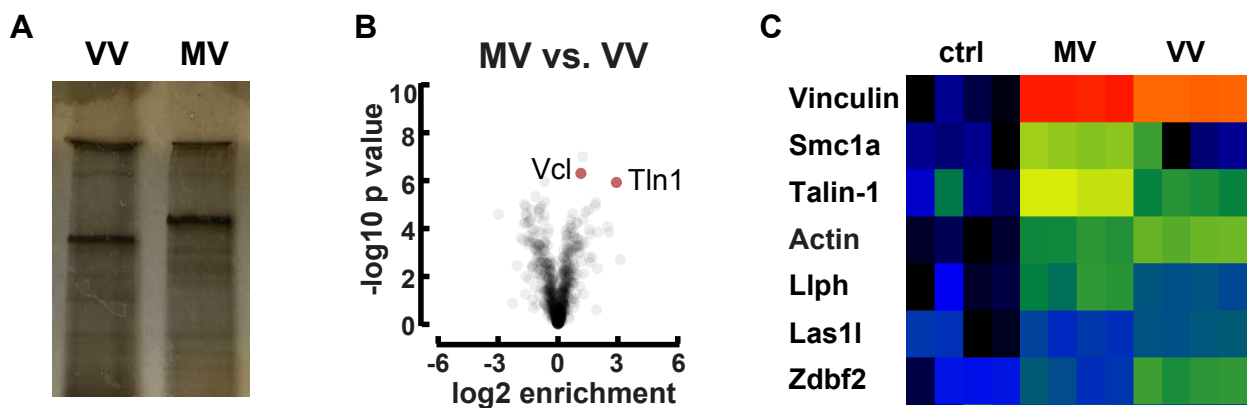


Figure 6.8: Analysis of (meta)vinculin binding partners by mass spectrometry **A.** Silver staining from a pull-down experiment of VV and MV using α -GFP beads. **B.** Volcano plot of results from co-IP mass spectrometry showing a 5-fold increase of interaction between MV and talin-1. **C.** Cluster analysis of the most significantly enhanced proteins pulled down with VV or MV. A negative control was provided by analysis of *vinc*^{-/-} cells. $n = 4$ independent repeats for each cell line.

6.2.2 Co-immunoprecipitation confirms increased affinity of metavinculin for talin

To confirm results from mass spectrometry, I performed a manual pull-down of VV and MV transfected cell lysates using magnetic beads and stained immunoblots with an antibody against talin (details in 4.1.2). Binding of talin to vinculin was enhanced in accordance with the 5-fold increase we observed in mass spectrometry results (Fig. 6.9 A). To confirm the specificity of the interaction, I stably transfected talin-HA-EBFP and performed co-immunoprecipitation by pulling on the HA-tag and evaluation with an α -vinculin antibody recognizing both isoforms. Again, a higher amount of metavinculin interacted with talin (Fig. 6.9 B).

The talin binding site is located within the vinculin and metavinculin head domain, which is identical for both isoform. Increased interaction of metavinculin with talin therefore can not be explained by a change in affinity between both binding partners, but needs to involve other factors like changed head-tail interaction (HTI) for metavinculin, stabilization by other FA proteins or interaction with F-actin.

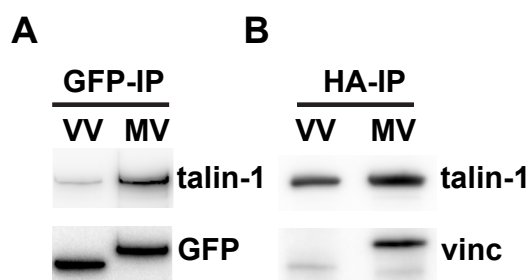


Figure 6.9: Immunoprecipitation data indicating increased interaction of MV with talin **A.** Manual pull-down experiments of VV and MV using magnetic beads coated with α -GFP and **B.** of talin-1-HA-enhanced blue fluorescent protein (EBFP) using α -HA beads. Antibodies against vinculin, talin-1 and GFP were used as indicated. A higher amount of talin is co-immunoprecipitated with talin-1 and vice versa.

6.2.3 Actin binding upon activation by *Shigella* invasin (IpaA) is similar for vinculin and metavinculin

Ultracentrifugation pull-down assays can be used to study whether proteins are co-pelleted with F-actin. Full-length vinculin needs to be activated, e.g. by the bacterial invasin protein IpaA, before it can bind to F-actin. I purified IpaA and added it to hypotonic cell lysates of VV and MV cells together with polymerized actin as described in section 4.1.4 and 4.1.5 (Fig. 6.10 B). After the centrifugation step supernatant (S) and pellet (P) were stained with α -vinculin antibody and compared with the amount of vinculin in the total control (T).

Only after addition of IpaA, vinculin and metavinculin could be observed in the pellet, however, there was no difference in the respective amount being pulled down, indicating similar binding affinity to F-actin (Fig. 6.10 D). This result is in accordance with experiments using only the vinculin tail domain (Vt) or metavinculin tail domain (MVt) domain [54]. However, I know from previous work that binding affinity is not enough to characterize the interaction of proteins with the F-actin cytoskeleton (see section 1.3.3).

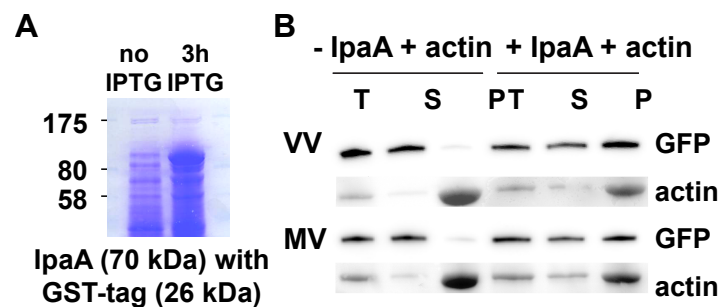


Figure 6.10: Probing of interaction of VV and MV with F-actin A. Coomassie staining showing expression of IpaA with a GST-tag after induction with isopropyl- β -D-thiogalactopyranosid (IPTG). B. Actin ultra-centrifugation assay of VV and MV in the presence of absence of IpaA. Only after addition of the bacterial entry protein both VV and MV can be seen in the pelleted fraction (P) which indicates binding to F-actin. T: total lysate, S: supernatant, P: pellet

Next, I wanted to confirm that vinculin and metavinculin indeed undergo a conformational change upon binding to IpaA. A biosensor measuring vinculin activation has first been introduced by [57] for both *in vitro* and live cell measurement and was adapted for use in metavinculin (for cloning strategy please refer to 4.3.5). I analysed the lifetime of hypotonic lysates (sec. 4.1.5) from cells stably transfected with vinculin activation sensor (VAS) or metavinculin activation sensor (MAS) before and after addition of IpaA (sec. 4.1.4) and in presence of F-actin. Sample preparation was identical to ultracentrifugation assays (Tab. 4.13 & 4.14). The expected decrease in Förster resonance energy transfer (FRET) efficiency (VAS $22.89 \pm 0.22\%$ to $8.89 \pm 1.29\%$, MAS $11.98 \pm 0.43\%$ to $7.1 \pm 0.12\%$) was observed and, as

anticipated, MAS showed a lower initial FRET as the fluorophores are separated by a longer tail domain (Fig. 6.11 A).

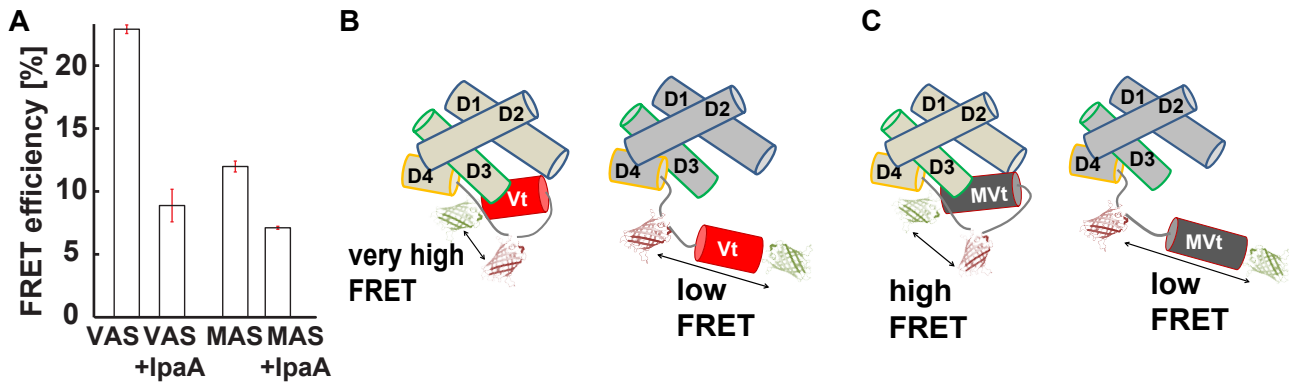


Figure 6.11: *In vitro* measurement of vinculin and metavinculin activation sensors (ASs) **A.** The FRET efficiency of hypotonic lysates mixed with actin was measured before and after addition of IpaA. Conformational changes are reported by a decreased FRET efficiency for both vinculin activation sensor (VAS) and metavinculin activation sensor (MAS) after addition of IpaA. **B.** Vinculin activation sensor (AS) consists of an internal mCherry fluorophore which was inserted between amino acids (aa) 883-884 of the unstructured linker region, a venus tag is positioned at the N-terminus. In the closed or autoinhibited conformation fluorophores are closer together, leading to higher FRET than in the open or active conformation. **C.** Fluorophore position for metavinculin is identical, however, the distances between the fluorophores are altered due to the 68 aa long insert.

6.2.4 Summary of biological characterization of cell lines

In the last section we learned that metavinculin can localize to FA even in the absence of vinculin and rescues the spreading defect caused by vinculin deletion. Interestingly, metavinculin exhibits higher stability in FA and its interaction with talin-1 is increased as compared to vinculin. However, standard methods from cell biology and biochemistry have limited insights with respect to the molecular function of metavinculin.

It has been shown that vinculin is a mechanotransducer and can bear piconewton ($10^{-12}N$) (pN) forces at sites of FA [10], but whether and how metavinculin transduces force remains unclear. Thus, I decided to use FRET based biosensor constructs to compare forces across both proteins in living cells.

6.3 Establishment and characterization of FRET-based biosensor constructs in living cells

Here, I introduce time-correlated single photon counting (TCSPC)-fluorescence lifetime imaging microscopy (FLIM) as a robust method to access the fluorescence lifetime of FRET constructs in FA of living cells. First, I confirm the reliability of the system and show that insertion into proteins does not influence fluorophore lifetimes. Next, I present cell lines expressing proteins with a tension sensor and prove that their functionality is not affected by the linker module. In the last part, effects of protein expression level and point mutations will be analyzed.

6.3.1 Control probes for lifetime measurements in living cells

Fluorophore lifetimes depend on their surrounding and might be influenced by the insertion site. Therefore, I measured lifetimes of venus and monomeric Cherry (mCherry) at internal and C-terminal positions in vinculin and metavinculin (Fig. 6.12). For the donor fluorophore venus lifetime was $\tau_D = 2.96 \pm 0.04 \text{ ns}$ and the acceptor mCherry was measured to decay in $\tau_A = 1.41 \pm 0.03 \text{ ns}$. Position inside the protein did not change fluorescence lifetime and I could not observe differences between vinculin and metavinculin (Fig. 6.13 B). Obtained values for the fluorescence lifetime were highly reproducible over a time period of three years and in good accordance with the literature [131], as well as experiments by other group members [20].

Next, I measured whether intermolecular energy transfer occurs between adjacent molecules. Therefore I co-expressed internal or C-terminal constructs of vinculin and metavinculin with both venus and mCherry tags (Fig. 6.12 A & B). Intermolecular FRET was highest for internal VV-VC measured inside FA ($5.16 \pm 0.1\%$) and disappeared for C-terminally tagged VV-VC ($0.43 \pm 0.05\%$). Values for all other combinations were around 3% (Fig. 6.14 A). When signal from the whole cell was analyzed, values for intermolecular FRET dropped by around 2%, indicating that a large contribution for intermolecular FRET is specific to signal from FA.

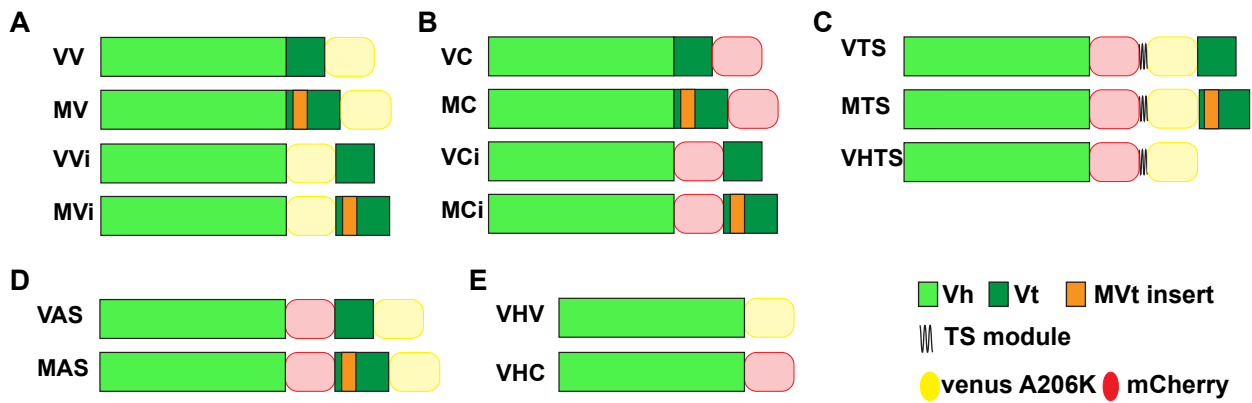


Figure 6.12: Schematic overview of fluorescently tagged vinculin and metavinculin constructs **A.** Vinculin and metavinculin with C-terminal venus fluorophore (VV & MV) or internal fluorescence tag (vinculin-venus(internal) (VVi) & metavinculin-venus(internal) (MVi)). **B.** Same constructs as shown in **A.**, using mCherry instead of venus (VC, MC, vinculin-mCherry(internal) (VCi), metavinculin-mCherry(internal) (MCi)). **C.** Insertion of the tension sensor (TS) module into vinculin (VTS) or metavinculin (MTS) after the vinculin head domain (Vh) at position 883. **D.** Activation sensors (ASs) consist of an internal mCherry tag between aa 883-884 and a C-terminal venus inserted into vinculin (VAS) or metavinculin (MAS). **E.** vinculin head domain (Vh) constructs tagged with C-terminal venus (VHV) and mCherry (vinculin-head-mCherry (VHC)). All constructs are depicted to scale in units of amino acids.

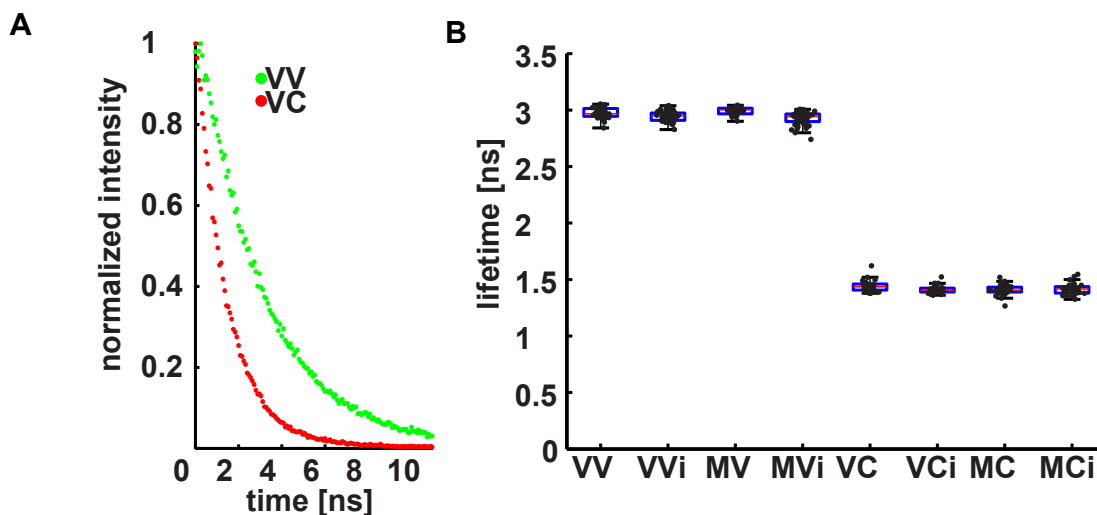


Figure 6.13: Lifetime measurement of single fluorophores **A.** Representative normalized photon count measurements of two cells expressing either VV or VC. **B.** Lifetime measurement for fluorophores venus and mCherry at internal or C-terminal position in vinculin or metavinculin (n = 47, 59, 30, 58, 32, 29, 32, 32).

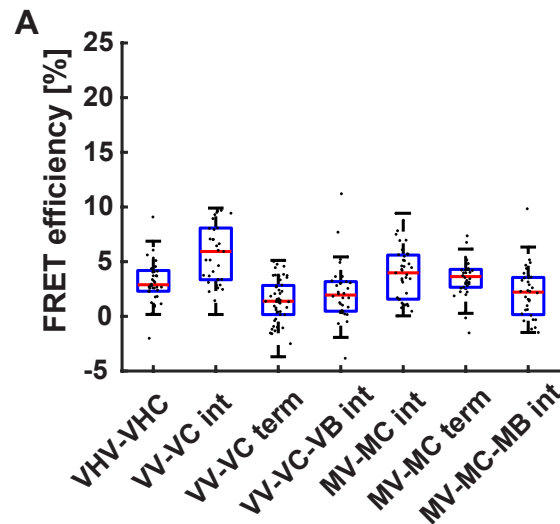


Figure 6.14: Intermolecular controls A. Co-expression of internal or C-terminal tagged venus and mCherry constructs in vinculin, metavinculin or Vh. Intermolecular FRET is highest for internal vinculin fluorophores and negligible for C-terminally tagged vinculin. All other constructs yield values around 3%. Additional expression of EBFP-tagged protein (VB, MB) further reduces intermolecular FRET observed between venus and mCherry tagged constructs ($n = 40, 35, 52, 34, 39, 38, 36$).

6.3.2 Size and dynamics of FA is not affected by insertion of TS module

Ensuring that insertion of linker peptides does not disturb protein function is crucial for all biosensor experiments [101]. Even though the VTS has been well studied and characterized in the past using a different FRET pair [10], we repeated all control experiments for both VTS and MTS. Full-length TS constructs could rescue the spreading defect of $\text{vinc}^{-/-}$ cells, whereas expression of only vinculin head tension sensor (VHTS) showed impaired spreading after 120 *min* and increased total FA size for all time-points (Fig. 6.15 A & B). Total adhesion size per cell after 120 *min* on FN coated glass was determined from accumulated fluorescence data of FLIM images. Cell lines expressing C-terminal fluorophores or flagelliform peptide (F40) linker peptides did not show differences in total FA area per cell (Fig. 6.16 A & B).

I performed FRAP experiments for VTS and MTS expressing cells and found increased stability of MTS compared to VTS at FA (VTS: 93.1 ± 12.9 s; MTS: 108.2 ± 9.48 s) (Fig. 6.7 C), however, the difference was not as pronounced as for VV and MV only (Fig. 6.7 A).

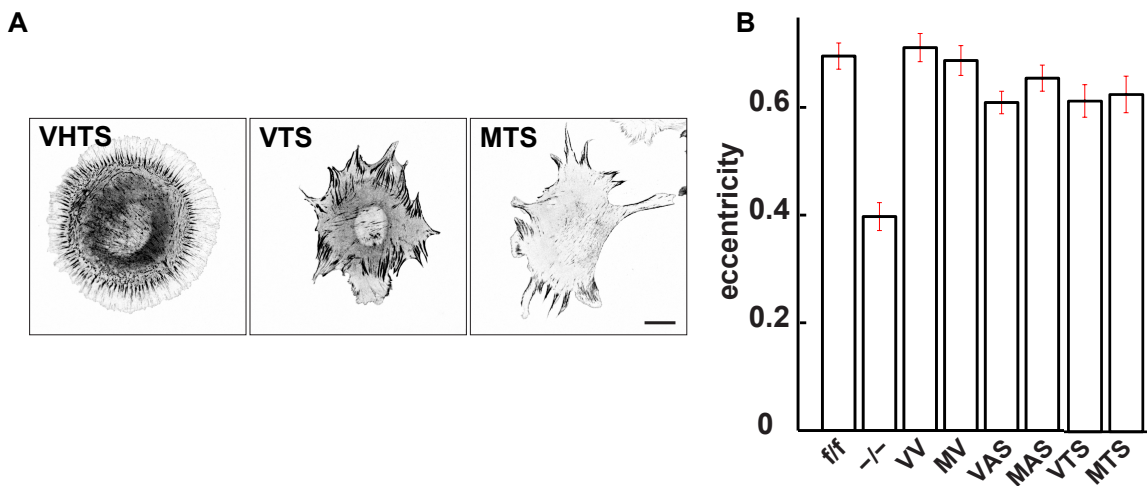


Figure 6.15: Expression of TS and AS constructs in $\text{vinc}^{-/-}$ cells A. Immunostaining of VHTS, VTS and MTS constructs expressed in $\text{vinc}^{-/-}$ cells after 120 min on FN, scale bar 20 μm . B. Eccentricity of cells transfected with TS and AS constructs show rescue of the knockout spreading defect. Cell Mask staining of live cells after 120 min on 10 $\mu\text{g/ml}$ FN.

6.3.3 Mean force across MTS is decreased on glass and ESS

The TCSPC-FLIM setup measures bulk fluorescence from all FA inside a cell and yields a mean value for all molecules. As expected from previous studies [10] seeding cells on FN coated glass dishes (see 4.5.2) reduced FRET across VTS ($14.17 \pm 0.99\%$) compared to the VHTS control ($18.05 \pm 0.68\%$). For this study, the most important result was, how tension is affected by TS insertion into metavinculin. Interestingly, I observed a significant increase of FRET from MTS ($16.26 \pm 0.48\%$) compared to VTS, suggesting diminished force across metavinculin (Fig. 6.17 A).

I repeated measurements using the HP35 linker and found a significant reduction of FRET for both VTS ($30.41 \pm 0.19\%$) and MTS ($31.08 \pm 0.09\%$) compared to VHTS ($35.5 \pm 0.31\%$) (Fig. 6.17 B). Due to properties of the TS module, which has a shorter length and consists of the FRET pair YPet/mCherry, overall FRET values are increased leading to a higher dynamic range and larger absolute differences between measured FRET efficiencies. This data also shows that a fraction of vinculin and metavinculin molecules are under high enough force to open up the 6 – 8 pNHP35 linker. More measurements and controls using the HP35 and its stable variant will be needed before this data can finally be interpreted.

To test more physiological conditions of substrate stiffness I seeded VTS and MTS expressing cells on commercial FN coated ESS with stiffness of 1.5 kPa and 15 kPa, where they exhibited larger and more elongated FA (see 6.3.2). I observed higher forces across VTS on 1.5 kPa ($10.54 \pm 0.04\%$) and 15 kPa ($11.54 \pm 0.04\%$), whereas MTS remained unchanged (1.5 kPa : $15.59 \pm 0.04\%$, 15 kPa : $16.21 \pm 0.02\%$) (Fig. 6.18 A).

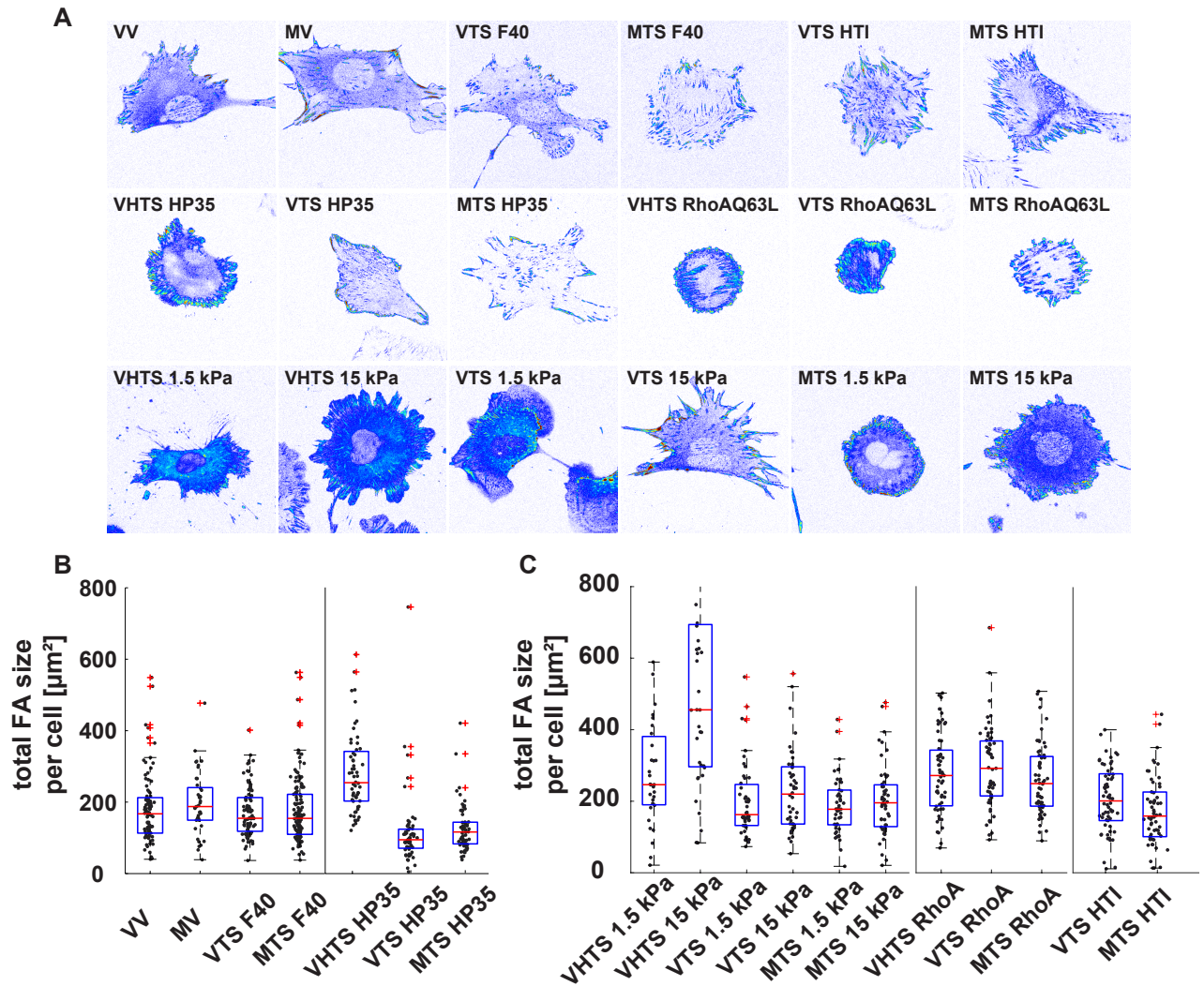


Figure 6.16: Determination of FA size from live cell images used for FLIM microscopy **A.** Representative images of TS constructs used for FLIM measurements from living cells seeded on $10 \mu\text{g/ml}$ FN on glass or elastic soft substrates (ESS) of 1.5 kPa and 15 kPa stiffness as indicated. **B.** Total size of FA per cell remained constant for expression of VV or MV constructs as compared to TS with either the F₄₀ or villin headpiece (HP₃₅) linker. An increase in cumulative FA size can be seen for all constructs expressing only the Vh. Size is significantly increased for co-expression of constitutively active RhoAQ63L and a higher spread is observed for TS with a HTI mutation.

6.3.4 Control measurements show functionality of TS constructs

To test whether the differences in FRET efficiencies between vinculin and metavinculin were indeed caused by differences in tension, TS constructs were expressed in a cell line lacking both talin-1 and talin-2 isoform (talin2xko). As integrins are not activated, these cells are rounded up and can adhere, but not spread on FN. Due to lower photon counts, the overall noise level was increased in these measurements; pinhole and magnification were adjusted to the smaller area of round cells. Differences between FRET efficiencies for TS and control constructs decreased (VHTS: $15.40 \pm 0.25 \%$, VTS: $13.70 \pm 0.12 \%$, MTS: $15.46 \pm 0.12 \%$) (Fig. 6.19 C). As the variance in this experiment was high, I repeated measurements of VTS and

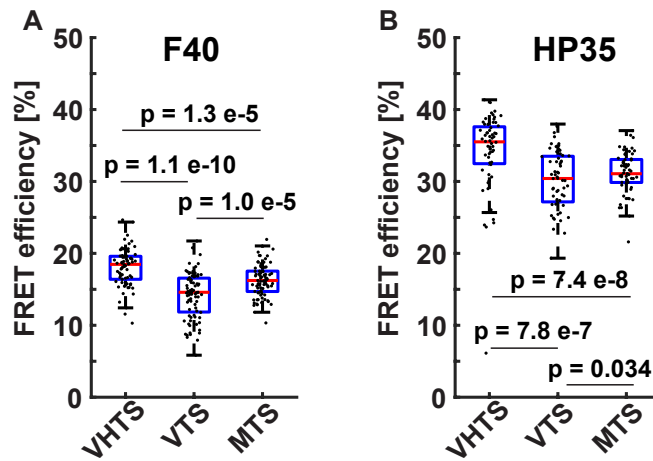


Figure 6.17: Analysis of VTS and MTS with F40 and HP35 linkers A. FRET efficiency for TS constructs with a F40 linker. VHTS serves as a no-force control and shows highest FRET efficiency. Force is increased for VTS cells seeded on FN and slightly lower for MTS ($n = 74, 83, 86$ from 4 days). B. Results of TS measurements using a HP35 peptide as a linker. Again, force is higher for VTS and MTS than for VHTS. The value for the donor fluorophore YPets was fixed to $\tau_D = 3.02 \text{ ns}$ ($n = 60, 60, 61$ from 3 days)

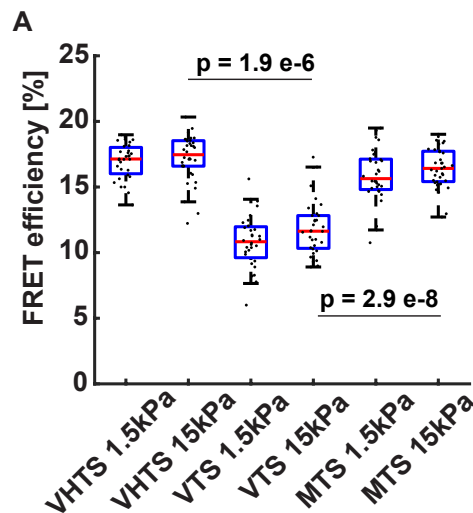


Figure 6.18: Measurement of TS with F40 linker on ESSs A. Physiological stiffness was achieved by seeding of cells on FN coated soft substrates with 1.5 kPa and 15 kPa stiffness. Force across VTS increased under these conditions, whereas VHTS and MTS did not show changes ($n = 31, 36, 32, 32, 32, 35$ from 3 days)

MTS in talin2xko cells which were treated with ROCK inhibitor Y-27632 and increased acquisition time (Fig. 6.22 B).

As a second control measurement, I introduced a single point mutation (I997A), which has been shown to disrupt the actin binding surface of vinculin [27]. The result was an increase of FRET efficiency for VTS-I997A ($18.87 \pm 0.01 \%$) comparable to control levels of VHTS, showing that defective actin interaction leads to drop in forces across vinculin (Fig. 6.19 B).

Together, these control experiments suggest that indeed the engagement with talin on one side and the F-actin cytoskeleton on the other, is producing the forces measured across TS

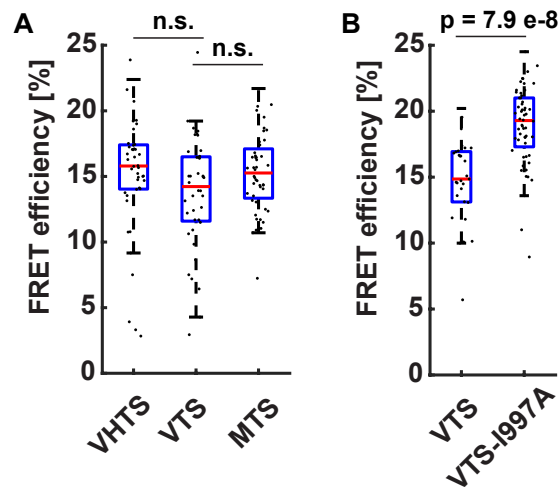


Figure 6.19: Control measurements for tension sensor constructs **A.** Measurements of F₄₀ TS constructs in talin2xko cells. Due to the lack of talin no force is sensed across vinculin or metavinculin. Cells remained rounded and no FA were detected (n = 44, 40, 48 from 3 days). **B.** Disturbing the actin binding surface of vinculin by mutating I997A leads to reduced force transduction across VTS-I997A (n = 29, 56 from 3 days).

constructs.

6.3.5 Force across VTS can be increased by additional vinculin or metavinculin protein

In muscles of the human body, vinculin and metavinculin are co-expressed and it has been proposed that metavinculin needs to dimerize with vinculin before it can be functional [44]. Therefore, I wanted to determine whether vinculin affects force transduction across metavinculin and vice versa.

I co-expressed EBFP-tagged vinculin or metavinculin, which does not spectrally disturb our measurements, with TS constructs of the other isoform (Fig. 6.20 A & B). Force transduction was aggravated across VTS in the presence of metavinculin-EBFP (MB) ($9.04 \pm 0.15\%$), whereas MTS did not show increased levels of force upon expression of vinculin-EBFP (VB) ($14.43 \pm 0.06\%$). As expected, the control probe VHTS, did not exhibit statistically significant changes and only slightly reduced FRET ($16.74 \pm 0.03\%$), which can be explained by a drop in intermolecular FRET (Fig. 6.14 A).

From this data, the question arises, whether increasing the total amount of protein has an influence on tension. When EBFP-tagged vinculin or metavinculin was co-expressed with the corresponding TS construct, I could again observe increased force across VTS with additional vinculin ($9.75 \pm 0.10\%$), while MTS with additional metavinculin remained unchanged ($14.77 \pm 0.05\%$).

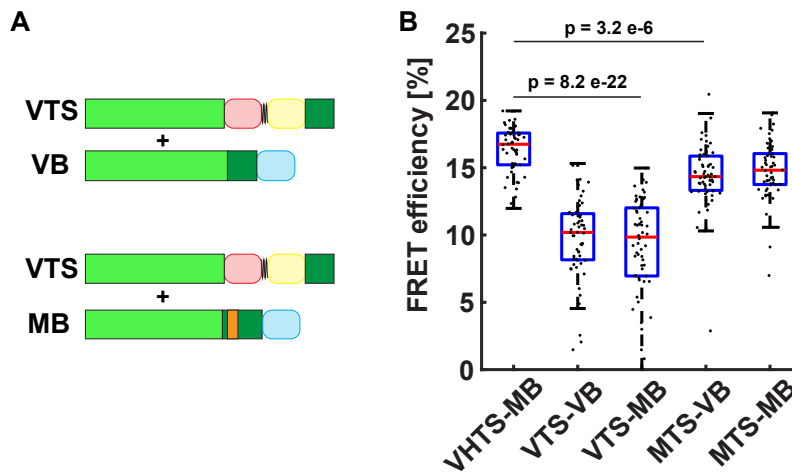


Figure 6.20: Effect of protein stoichiometry **A.** Proteins tagged with EBFP can be co-expressed with TS constructs without interfering with the FLIM measurements as they are spectrally separated. Expression of VTS with either VB or MB is shown as an example. Measurements were also performed for MTS and VHTS together with VB or MB. **B.** Expressing additional protein significantly increases force across VTS but not MTS ($n = 60, 56, 60, 59, 58$ from 3 days).

6.3.6 Affinity between head and tail regulates tension across vinculin and metavinculin

From the characterization studies of the cell line, I hypothesized that reduced affinity of the head domain for MVt leads to its increased interaction with talin-1. The working hypothesis was that force can be shared between multiple active metavinculin molecules binding to talin-1. Therefore I wanted to increase the proportion of vinculin and metavinculin molecules in the active states and study, whether lowered HTI has an effect on tension across VTS or MTS.

A double mutation in the vinculin head (N773A, E775A), which decreases affinity between head and tail and leads to hypertrophic FA has been described [56]. Upon expression of TS constructs with HTI mutations, differences in cellular morphology increased and I observed very small and some extensively large cells and irregularly shaped FAs. In some cells, I also observed bright protein accumulations, which were excluded from the analysis (see 6.1.2).

Force across VTS-HTI significantly increased and FRET efficiencies for some cells were even below 5% (VTS-HTI: $7.63 \pm 0.14\%$ vs. VTS: $13.37 \pm 0.03\%$). For the first time, I also observed lowered FRET across MTS-HTI, however, the effect was not as pronounced as for VTS-HTI (MTS-HTI: $14.26 \pm 0.10\%$ vs. MTS: $16.69 \pm 0.10\%$) (Fig. 6.21 A). Differences between TS constructs with HTI mutations vanished upon expression in talin2xko cells (VTS-HTI: $12.72 \pm 0.20\%$, MTS-HTI: $13.97 \pm 0.05\%$) (Fig. 6.21 B).

This result shows that force transduction is inherently coupled with HTI interaction of

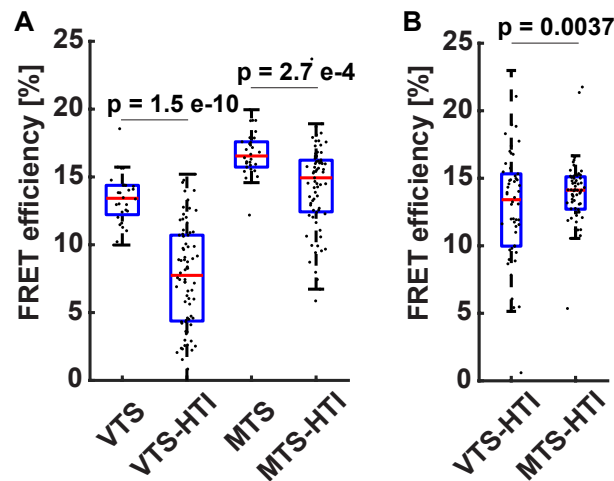


Figure 6.21: Analysis of VTS and MTS with HTI mutations **A.** Introducing a HTI mutation lead to an inhomogeneous population of cells. This was reflected in the FLIM measurements which revealed higher spread of FRET efficiencies for both VTS-HTI and MTS-HTI. Mean FRET efficiency was decreased for both constructs, with a higher effect on VTS ($n = 28,76,30,71$ from 3 days). **B.** Control measurements in talin2xko cells were not significantly different for VTS-HTI and MTS-HTI ($n = 54, 64$ from 3 days).

vinculin or metavinculin. However, it also indicates that reduced HTI is not sufficient to explain decreased force across MTS, as higher activation caused by lower HTI leads to increased force.

6.3.7 Mutation of the gelsolin homology motif in the metavinculin insert increases force across MTS

As co-expression of vinculin did not lead to increased forces across MTS and lowering the HTI did not explain the observed reduction of force across MTS, the next step was to analyze how interaction with F-actin influences force transduction across metavinculin. Therefore, I tested a hypothesis from Janssen et al. [79], who proposed that a gelsolin homology motif in the metavinculin tail is essential for its interaction with actin.

Residues 936-950 of MVt were compared to the actin binding sequence contained in a gelsolin peptide (AAIVQLDDYL) [132]. I decided to exchange the putative motif for actin severing DDY into an aa sequence NTL from the gelsolin like capping actin protein (CapG) protein which has been shown to gain severing function upon mutation to DDY [133]. It was exciting to see that the mutated form of MTS indeed bears more tension than before. Under the same experimental conditions the MTS-gelsolin like capping actin protein (CapG) mutant ($15.96 \pm 0.04\%$) showed lower FRET than MTS ($17.53 \pm 0.01\%$), but higher FRET than VTS ($14.29 \pm 0.01\%$) (Fig. 6.22 A). Again, expression in talin2xko cells and treatment

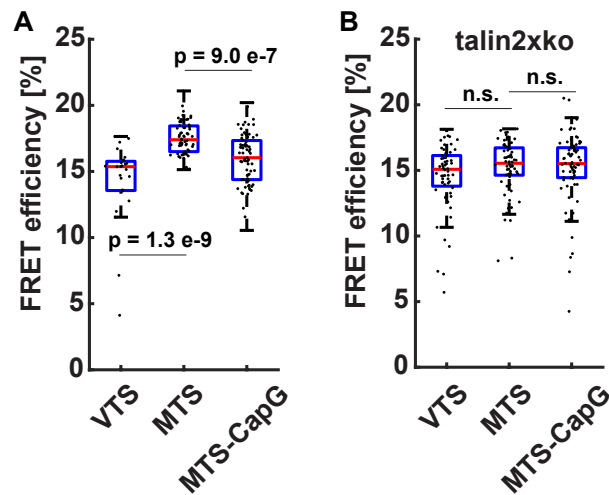


Figure 6.22: Analysis of MTS with actin interaction mutation **A.** The CapG mutation DDY₉₄₇NTL increases force across MTS-CapG compared to MTS (n = 24, 63, 79). **B.** Control experiments of MTS-CapG in talin2xko cells treated with ROCK inhibitor Y-27632 (n = 60, 68, 77 from 3 days).

with ROCK inhibitor or seeding on poly-L-lysine (PLL) restored the same levels for all three constructs (VTS-ctrl: 14.5 ± 0.06 %, MTS-ctrl: 15.21 ± 0.04 %, MTS-CapG-ctrl: 15.18 ± 0.07 %) (Fig. 6.22 B).

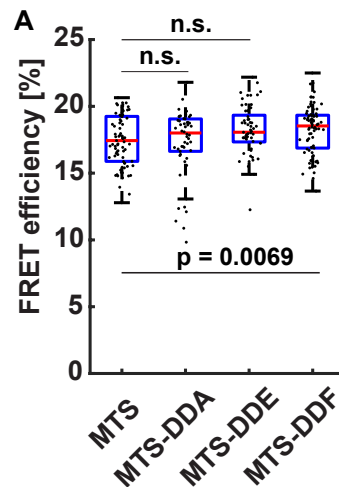


Figure 6.23: Phosphomimicking mutation of the DDY motif in MTS **A.** The tyrosine of the metavinculin DDY motif was mutated to phosphomimicking aa A,E,F. No differences between MTS and MTS-DDA, MTS-DDE or MTS-DDF could be observed (n = 77, 54, 57, 78).

A consequence of this finding was the search for a possible mechanism mediating the changed force transduction. Early studies on metavinculin proposed a role of the single additional tyrosine at aa 949 in the MVt insert [134]. Unfortunately, I was not able to confirm phosphorylation by mass spectrometry as the sequence covering for this region is very poor due to the low amount of arginine and lysine and high amount of aspartic and glutamic acid. Mass spectrometry analysis only indicated ubiquitinylation of metavinculin and

serine phosphorylation at aa S754. Therefore, I mutated Y949 to alanine, phenylalanine and glutamic acid and expressed TS of these phosphomimicking mutants in cells. However, all constructs localized normally and no differences in force transduction were observed (MTS: $17.43 \pm 0.04\%$, MTS-DDA: $17.49 \pm 0.09\%$, MTS-DDE: $18.20 \pm 0.04\%$, MTS-DDF: $18.24 \pm 0.03\%$) (Fig. 6.23). Therefore, I conclude that mutation of only Y949 is not sufficient to disrupt the mechanism by which force across MTS is decreased and the whole DDY motif needs to be exchanged.

6.3.8 Summary of tension sensor measurements

On FN coated glass and soft substrates the mean force in FA is reduced for metavinculin as compared to vinculin. Mean force across VTS increases for co-expression of vinculin or metavinculin, while MTS is not affected by additional protein. Contrary to the expectation that force can be shared between multiple active vinculin or metavinculin proteins, lowering the HTI interaction leads to an increase in force across both VTS and MTS.

Force across MTS could be increased by inserting mutations into the part of the metavinculin linker, which is thought to mechanically destabilize F-actin. This finding is surprising and additional experiments will be necessary to understand how the gelsolin homology motif in the metavinculin linker can reduce force across the protein by interaction with F-actin.

6.4 Probing interactions of cells with their mechanical environment

In this last section I want to introduce two biophysical techniques which can be used to study the influence of metavinculin for interaction with the mechanical environment of the cell. First, I analyzed the effect of expression of metavinculin on the amount of traction a cell can actively transduce to an elastic surface. Finally, I performed initial experiments to combine TCSPC-FLIM with uniaxial cell stretching to measure the influence of an externally applied mechanical stimulus on TS constructs.

6.4.1 Traction force microscopy (TFM) of vinculin and metavinculin expressing cells

I measured the amount of deformation which cells generated on an elastic substrate by Fourier transform traction cytometry (FTTC)-TFM (see sections 2.3.2 & 4.4.2). As TFM has not been established in the lab before, I needed to optimize parameters like bead size and color, scan speed and resolution, handling of micropatterns and coating procedure, as well as seeding and detachment of cells. During this process and for the analysis I received help from Benedikt Sabass, who had previously published his methods in [112].

The question was, whether metavinculin expression has an influence on the amount of traction generated by a cell. First measurements on 8 kPa substrates with a low concentration FN coating (10 $\mu\text{g/ml}$) lead to a large spread in strain energy values (Fig. 6.25 A). Therefore, we increased the polyacrylamide (PAA) substrate stiffness to 15 kPa and used 1 mg/ml FN during the sulfo SANPAH photoactivation step, to enhance the attachment and spreading of cells. Two independent sets of experiments (each at least 15 cells from three different days) showed that there is no difference in strain energy or traction between VV and MV expressing cells (median values for traction force VV: 0.435 pJ and 0.427 pJ, MV: 0.519 pJ and 0.449 pJ, Fig. 6.24 B & Fig. 6.25 B).

For knockout ($\text{vinc}^{-/-}$) and control cells ($\text{vinc}^{f/f}$) we could not use fluorescence signal to determine the distance from the FA to the gel and systematically underestimated the distance from the substrate, which was determined using transmission light in the brightfield channel. Total strain energies per cell were lower than for VV or MV cells ($\text{vinc}^{f/f}$: 0.283 pJ, $n = 33$ cells, $\text{vinc}^{-/-}$: 0.278 pJ, $n = 28$ cells), but there was no significant difference between both cell lines.

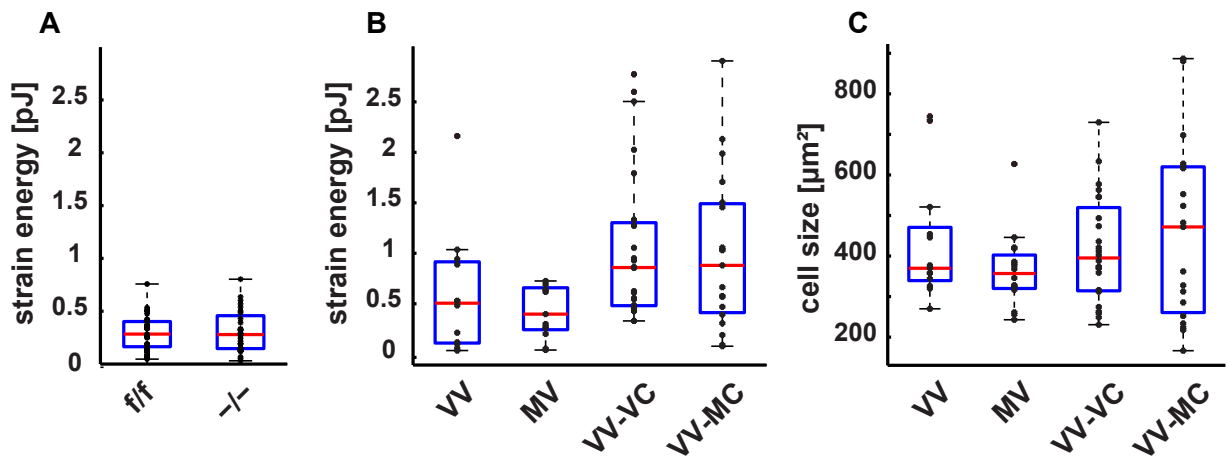


Figure 6.24: Results of TFM experiments on 15 kPa substrates A. Total strain energy per cell for *vinc^{f/f}* and *vinc^{-/-}* on 15 kPa substrates. Black circles mark single cells B. Comparison of *vinc^{-/-}* cells which were stably transfected with different fluorescently tagged vinculin and metavinculin constructs. C. Cell sizes for data shown in B., determined by manual tracking of brightfield images.

Next, I wanted to analyze whether metavinculin can alter traction forces in presence of vinculin and studied cells co-expressing either VV and VC or VV and MC. Overall strain energy was increased and showed larger variance (VV-VC: 0.858 pJ, n=24 cells, VV-MC: 0.880 pJ, n=19 cells) (Fig. 6.24 B & C).

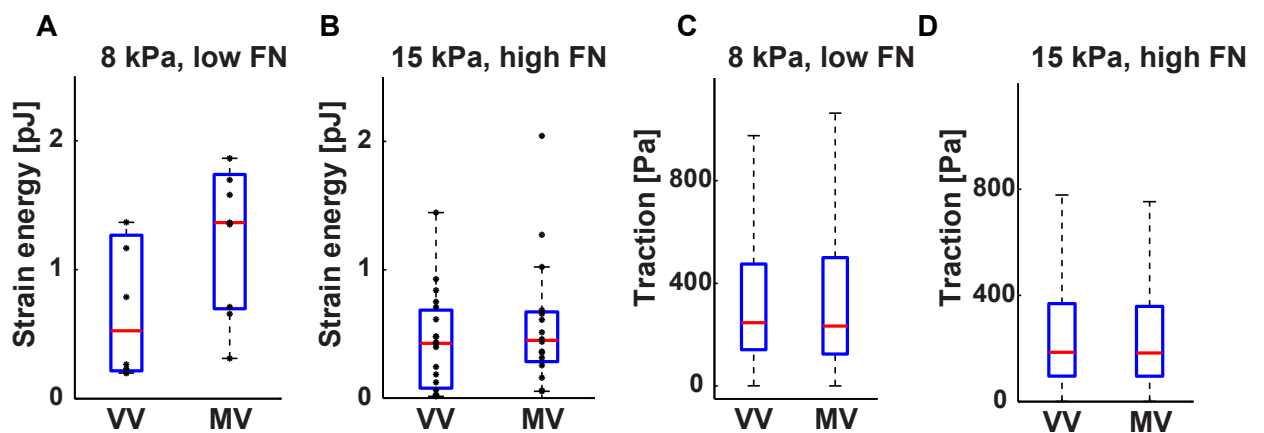


Figure 6.25: Comparison of TFM experiments on 15 kPa and 8 kPa substrates A.-B. Strain energy of VV and MV expressing cells for two different substrate stiffnesses (A.: 8 kPa, B.: 15 kPa) and FN concentrations during coating. Spread is significantly higher for cells with lower adherence on soft substrates (A.). Dots show single measurements of individual cells. C.-D. Traction calculated from individual displacement vectors shows no differences between VV and MV expressing cell lines.

6.4.2 Combining TCSPC-FLIM with uniaxial cell stretching

To gain further insight about the correlation between intracellular force and externally applied stretch, I mounted a uniaxial cell-stretching device, which has been built by Prof. Merkel and colleagues at Forschungszentrum Jülich [110], onto the microscope stage used for TCSPC-FLIM experiments. Imaging through the bottom of stretch-chambers was only possible with a long-distance objective (for details of stretch-chamber preparation please refer to section 4.4.3). I seeded VTS and MTS expressing cells on pre-stretched chambers and measured around 10 cells for this condition. Next, a stretch of 3 mm was applied using an electronically controlled motor. After re-focusing, I again measured 10 cells and noted time-points of measurement. To my surprise both VTS and MTS showed an increase in FRET after the stretching process (VTS: $10.7 \pm 0.3\%$ to $13.4 \pm 0.25\%$ and MTS: $13.5 \pm 0.17\%$ to $15.1 \pm 0.05\%$) (Fig. 6.26 A).

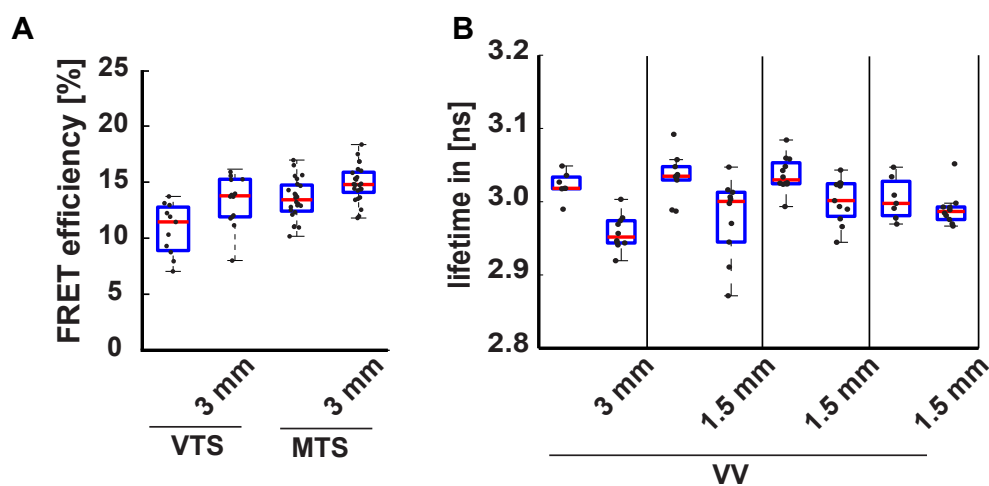


Figure 6.26: Preliminary results from cell stretching **A.** FLIM measurement of TS constructs with F40 linker on polydimethylsiloxane (PDMS) stretch chambers. A linear elastic stretch of 3 mm was applied to the stretch chambers using a motorized stage. Both, VTS and MTS showed an increase in FRET efficiency after 3 mm stretch compared to the unstretched cells. Merged data from three experiments. **B.** Fluorescence lifetimes for VV from FA of stretched and unstretched cells. A decrease in lifetime of about 0.1 ns could be seen for a stretch of 3 mm while stretching by 1.5 mm lead to a slightly smaller effect. Data from four independent experiments.

To test for confounding factors during the stretching procedure, I seeded cells expressing only VV and not the TS module and measured lifetime before and after 3 mm and 1.5 mm stretch. Even in this control experiment a decrease of donor fluorophore lifetime was seen (Fig. 6.26 B). Therefore I concluded that substrate stretch induces changes in the fluorescence lifetime independent of FRET. Further experiments will be required to analyze, which effect is responsible for the change in lifetime upon stretch and to find methods to calibrate the system, e.g. by correcting for differences in the donor lifetime.

7 Discussion

7.1 The role of vinculin and metavinculin in focal adhesions (FAs)

7.1.1 Generation and characterization of new vinculin knockout cells

Over the years, various vinculin knockout cell lines have been established and provide an indispensable tool to understand its function. Nevertheless, we did not rely on published cell lines, but generated clonal control and knockout cells ($\text{vinc}^{f/f}$ and $\text{vinc}^{-/-}$) from isolated mouse embryonic fibroblasts (MEFs) with a floxed vinculin gene to exclude adaptation effects or side effects of the knockout and ensure a homogeneous population. While I observed previously described features of $\text{vinc}^{-/-}$ cells, like the delayed spreading phenotype, our cell line maintained their size and formed FAs comparable to $\text{vinc}^{f/f}$. This was not surprising, as I took the clonal cell line with the least severe phenotype (clone $\text{vinc}^{-/-}$ #2-1, Fig. 6.1 B) instead of another clone with decreased size ($\text{vinc}^{-/-}$ #2-5, Fig. 6.1 C). The effect of vinculin depletion might be more severe for other cell types and I observed a large variation in cell size and morphology, even for clonal cell lines.

7.1.2 Comparison of metavinculin localization to predictions from *in vitro* studies

In mammalian tissue metavinculin is always co-expressed with ubiquitously expressed vinculin. It has been proposed that vinculin activated by phosphatidylinositol 4,5-bisphosphate (PIP₂) serves as a co-activator for metavinculin [44, 54]. From the observation that vinculin tail domain (Vt) and metavinculin tail domain (MVt) form heterodimers, the authors hypothesized that metavinculin can only localize to nascent or mature adhesions in the presence of full-length vinculin [44]. I showed that metavinculin can localize to FAs, nascent adhesions, and dorsal ruffles in the absence of vinculin and even takes over part of its function in cell spreading, adhesion formation, and dynamics. This result shows that insight from truncated

forms of vinculin *in vitro* is limited and cellular models are needed to understand protein function. My results emphasize the role of the tail domain in regulating FA morphology and spreading dynamics as vinculin head domain (Vh) alone is not sufficient for rescue. Knock-in of mutated vinculin constructs, such as the Vh domain or head-tail interaction (HTI) mutations (N773A, E775A), produced more dramatic morphological changes than vinculin depletion.

At least under the experimental conditions I tested, there are no morphological differences between vinculin and metavinculin expressing cell lines. This might not be true for all cell types and it could also be that localization is affected at a scale which is below the resolution limit of standard fluorescence microscopy, e.g. due to different z-position inside the FA plaque.

7.1.3 Changes in metavinculin interaction partners and binding affinities

Actin co-sedimentation assays reproduced the previously described finding that both vinculin and metavinculin need to be activated, e.g. by *Shigella* invasin (IpaA), before they can bind to the actin pellet. I generated a metavinculin activation sensor in analogy to the previously published vinculin activation sensor [57] to confirm the activation upon binding to F-actin. Direct measurement of Förster resonance energy transfer (FRET) efficiency via fluorescence lifetime imaging microscopy (FLIM) from cell lysates provided an elegant way to characterize activation sensors (ASs) *in vitro*, which is more accurate than previously used normalized fluorescence emission spectra [57].

Actin affinities of $K_D \approx 5 \cdot 10^{-7}$ for both vinculin and metavinculin have been reported [80], however there is large evidence for differences concerning mechanical stability and organization of actin by the two isoforms [79, 80]. While earlier studies focused on the importance of MVt interaction with F-actin, I stress the importance of binding between the metavinculin head domain and talin-1. From the quantitative mass spectrometry data, it was estimated that metavinculin binds about 5 fold better to talin-1 than vinculin. This increased interaction with talin-1 was consistent with manual pull-down experiments.

The large difference in binding of talin-1 was rather surprising, as the amino acid sequence and structure of both vinculin and metavinculin head domains, which bind to various vinculin binding sites (VBSs) in the talin rod domain (D1-D4, Fig. 1.4 A-C), are identical. Most likely, changes in the affinity between metavinculin head and tail domains are the cause of altered talin-1 binding.

Surface plasmon resonance measurements of the affinity already reported a lower apparent affinity of MVt for the head domain compared to Vt (Vt: $K_D \approx 5 \cdot 10^{-8}$ vs. MVt: $K_d \approx 3 \cdot 10^{-7}$) due to a change in the association constant (Vt: $k_a \approx 1.3 \cdot 10^5$ vs. MVt: $k_a \approx 1.5 \cdot 10^4$) [44]. This HTI interaction seems to be crucial for regulation of vinculin function and more activated vinculin is found in FA as compared to the cytoplasm [57].

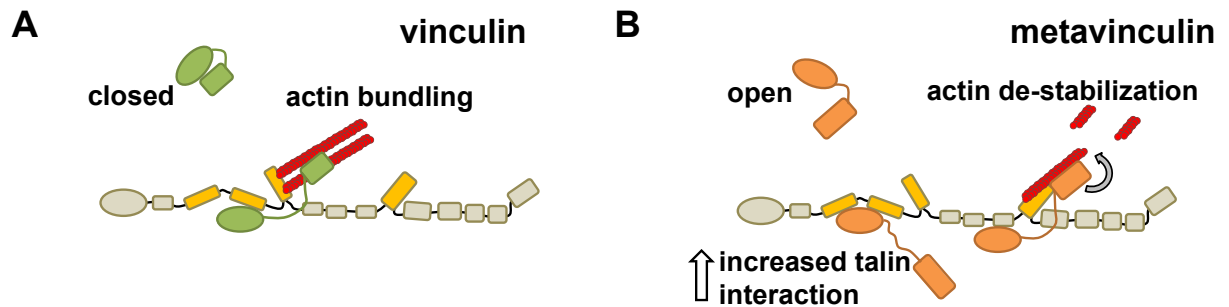


Figure 7.1: Model of binding affinities **A.** Binding of vinculin molecules to talin (gray) and the F-actin cytoskeleton (red). A HTI keeps vinculin (green) in a closed conformation which can be weakened by engagement of the vinculin head with talin. Interaction between the Vt domain and F-actin further stabilizes the open conformation and enables vinculin to be permanently incorporated into the talin-actin linkage where it can transduce mechanical forces. **B.** For metavinculin (orange) I assume a decrease in HTI. This leads to an increased accessibility of the talin binding domain in the metavinculin head. On the other hand, metavinculin might destabilize F-actin and therefore actively disengage the talin-integrin from the cytoskeleton.

7.1.4 Interpreting the decreased turnover of metavinculin at FA

Fluorescence recovery after photobleaching (FRAP) decays can be described as limited by reaction or diffusion rate [128]. In the case of FA molecules I was interested in the reaction rate, which is on a significantly longer timescale ($\tau_{\frac{1}{2}} = 50 - 200$ s) than the movement of molecules diffusing freely inside the cell ($\tau_{\frac{1}{2}} = 5 - 10$ s). As I bleach only FA regions, which are at least 100 times brighter than the surrounding cytoplasm, freely diffusing molecules will only be present at low numbers. Our setting is therefore not comparable to FRAP experiments analyzing either membrane-bound or cytoplasmic proteins.

When I analyzed the recovery rates of overexpressed talin and paxillin in vinculin-venus (VV) or metavinculin-venus (MV) expressing cell lines, there were no effects on turnover (Fig. 6.6 B & Fig. 6.7 B). Interestingly, the turnover of talin-1 is approximately twice as fast as for vinculin. This is not only true for our data but has been previously reported [135]: in contrast to talin, paxillin, focal adhesion kinase (FAK) or zyxin which showed fast turnover, vinculin is stably bound to FA. According to current opinion, multiple vinculin molecules are bound to each talin molecule leading to its stabilization in a cooperative manner [136], which could explain the slower turnover of vinculin compared to talin. Only a small fraction

of talin-1 is stably bound in FA and as I measured talin-1 and paxillin turnover in presence of endogenous protein, the high cytoplasmic signal might mask vinculin or metavinculin induced changes in stability.

FRAP curves for vinculin on micropatterned substrates were more regular than previously reported data, which suffered from large spreads due to the dependence of vinculin turnover on FA size and maturation state [130, 135]. If the amount of protein in the cell is increased, FRAP recovery is faster. This explains why other groups which express tagged vinculin constructs on endogenous background, report significantly shorter recovery times for vinculin [87, 130, 135].

Metavinculin stability was significantly decreased under two different geometrical conditions of the micropatterns (X- and Y-shaped). Measurement for 500 s suggest that not only the initial dynamic is slowed down, but also the immobile fraction is increased. A large fraction of metavinculin molecules seems to be stably bound in the FA. This is in accordance with the idea that metavinculin HTI is lowered and more molecules are in the active state. Vinculin with a T12 mutation, which increases the probability for an open conformation, showed slower recovery and increased immobile fraction [63].

Some months after the observation that turnover rate is decreased for metavinculin, this finding was published independently using C2C12 myoblasts [87]. It was suggested that metavinculin causes stabilization of microfilament anchorage in muscle-specific adhesion, leading to reduced turnover. However, reduced recovery rates do not necessarily reflect engagement with the cytoskeleton, as can be seen by the increased lifetime of Vh only and the actin-binding deficient mutant vinculin- Δ In20/21 [96]. I would rather argue that the link between metavinculin and the F-actin cytoskeleton is weaker than for vinculin and its strong binding to talin leads to a stabilization which is mostly independent of microfilament anchorage.

Various attempts have been made to understand how pre-formed clusters of FA molecules might contribute to their formation and there is evidence that proteins like vinculin, paxillin and FAK leave the adhesion sites in large aggregates during disassembly [137]. To fully understand vinculin and metavinculin turnover, it will therefore be necessary to apply techniques such as correlation spectroscopy and also observe the joint movement with talin or other FA components [138].

It is also important to note that molecular turnover rates do not allow for calculating overall stability of adhesion sites, which need to be calculated from unconfined cells and are best supplemented with information about actin flow [27]. There is a relation between turnover rates of FA molecules and for example intrinsic time-scale τ for cell re-orientation upon

cyclic stretch [123], however, the complexity of the adhesome makes it impossible to predict the effect of a single protein species for the stability of the entire FA.

7.1.5 Influence of posttranslational modifications on metavinculin function

More than 30 years ago at least eight times higher phosphorylation of metavinculin compared to avian vinculin was observed by use of ^{32}P -orthophosphate labeling and x-ray detection [139]. From the sequence of metavinculin we know that there is just one tyrosine (Y949) and four serines which potentially could be phosphorylated. Two of the serines are located in the KWSSK motif flanking the metavinculin insert.

It was not possible to analyse the relevant region in the metavinculin using mass spectrometry. Comparison with mass spectrometry data from other groups on the Phosphosite page (www.phosphosite.org) shows that this region is poorly covered during all screens and only phosphorylation of S972 has been reported.

Phosphomimicking mutant of Y949 did not lead to differences in force (Fig. 6.23), however, the influence of other sites, like the KWSSK motif flanking the metavinculin insert, still need to be tested. Besides the active role in force transduction, phosphorylation of Y949 might also be involved in signaling. I showed that the DDY motif is likely to be involved in the interaction of MVt with F-actin. Accessibility of this site could therefore be a readout for mechanical engagement of metavinculin with the cytoskeleton.

7.2 Evaluation of genetically encoded biosensors using TCSPC-FLIM

7.2.1 Fluorophore calibration measurements and analysis of intermolecular FRET

I did not observe changes in lifetime of internal vs. terminal fluorophores in vinculin or metavinculin on fibronectin (FN) coated glass. This also indicates that fluorophore properties are not affected by forces which act across vinculin or metavinculin. Single molecule calibration ensured the stability of the villin headpiece peptide (HP35) construct as no fluorophore unfolding was observed for forces as high as 24 pN over a time period of 5 min [20].

However, changes in donor lifetime seem to occur for FRET measurements on stretched vs. unstretched polydimethylsiloxane (PDMS) surfaces. Changes of lifetime can occur up to 100 nm distance from a surface [140]. It requires further testing to determine whether this effect is responsible for the change in fluorescence lifetime that we observed in PDMS chambers. Dyes absorbed in PDMS exhibit a big change in lifetime, however, we do not know about the effects of a PDMS surface [141].

FRET can occur between fluorophores from adjacent molecules. For all biosensor measurements it is therefore crucial to perform adequate control measurements and estimate an upper boundary for intermolecular FRET. FRET efficiency E depends on the fluorophore distance as $E \sim \frac{1}{r^6}$ and it is therefore important that control fluorophores are as close to the position of actual fluorophores as possible. Indeed, we observed differences between internal and C-terminally tagged vinculin. Substituting four fluorophores of two adjacent tension sensors by two proteins with an internal fluorophore of the two different colors systematically underestimates intermolecular FRET. On the other hand internal fluorophores might be closer than fluorophores of tension sensor (TS) modules. Therefore our measurements only provide an estimate for intermolecular FRET (Fig. 6.14).

7.2.2 Measurement of FRET signal from FA of living cells

While many other laboratories rely on ratiometric methods to determine FRET efficiencies inside living cells, I decided to establish a lifetime-based approach. FLIM is independent of fluorescence intensity and allows for direct calculation of FRET efficiencies, but provides lower temporal and spatial resolution.

From single molecule calibration, the response of linker peptides to the applied piconewton ($10^{-12}N$) (pN) forces is known, however, bulk measurement of fluorescence signal does not allow to discern between different states. Therefore, I can only determine a mean FRET efficiency without any access to the underlying distribution of states. It is therefore important to measure signal from several (e.g. 20) cells and 3-5 repeats per construct to equal out effects of cell morphology and differences in expression levels. To directly compare two constructs they should be measured on the same day and under exactly the same conditions. It is advisable to always measure a control consisting of only the donor fluorophore to exclude systematic errors in the measurement.

7.3 Factors contributing to force transduction across TS constructs

Force across metavinculin tension sensor (MTS) seems to be less than across vinculin tension sensor (VTS). This effect was especially pronounced on elastic soft substrates (ESS) and vanished upon expression in cell lacking both talin-1 and talin-2 (Fig. 6.18 A & Fig. 6.19 A). Several mechanisms have the potential to modulate force transduction across metavinculin (Fig. 7.2 B-D):

- Metavinculin could bind VBSs on talin independent from engagement with the actin cytoskeleton.
- Insertion of metavinculin molecules could lead to a reduction of force by distributing it across multiple proteins.
- Direct interaction between metavinculin tail domain and F-actin could destabilize filaments.

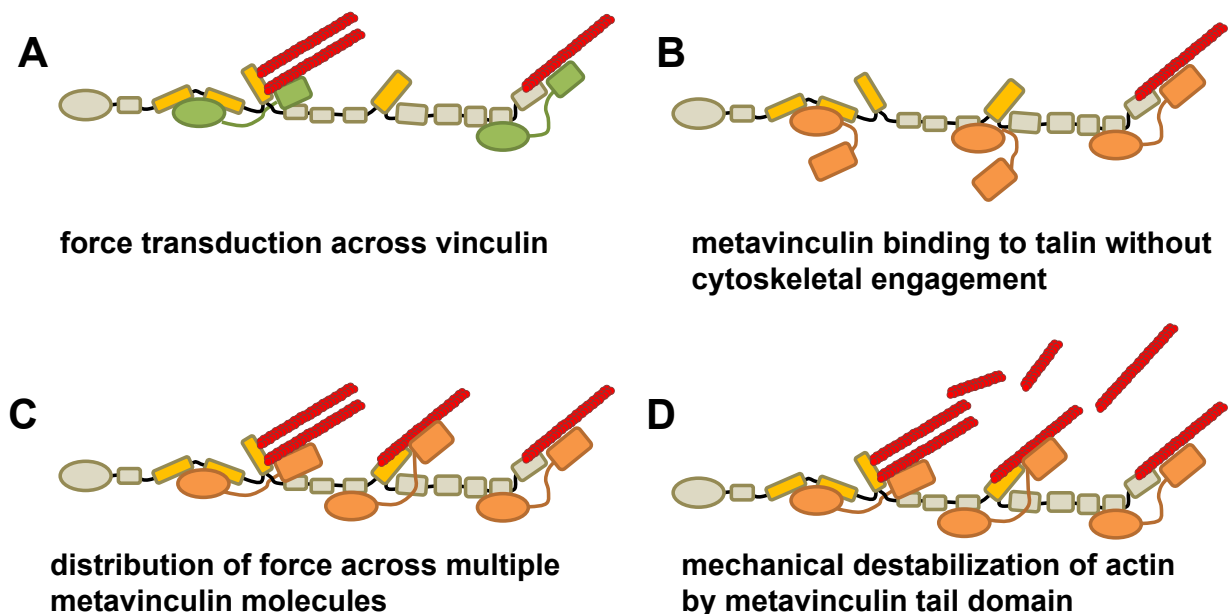


Figure 7.2: Models explaining reduced force across metavinculin A. Vinculin (green) is bound to both talin (gray) and the F-actin cytoskeleton (red). The domains of talin which are reoriented upon binding to vinculin and F-actin are shown in yellow. B.-D. depict models how reduced force across metavinculin (orange) could be explained: B. Metavinculin head domain bind talin without engaging to the F-actin cytoskeleton, thus blocking cytoskeletal linkages and reducing force. C. Parallel insertion of metavinculin molecules leads to a reduced mean force across the proteins. D. The MVt insert affects actin stability and reduces the force which can be beared by the linkage. This mechanism could be mediated by severing as well as changes in actin persistence length or bundling properties.

Using various TS constructs I tried to distinguish between the contribution of different factors to the force transduction across both VTS and MTS. In the following section, I will discuss, how expression of additional protein, engagement with the F-actin cytoskeleton, and altered HTI contribute to the modulation of mechanical force across vinculin and metavinculin.

7.3.1 Total amount of protein and turnover rates

Expression levels of vinculin and metavinculin show complex regulation, which *in vivo* can be modulated by factors as different as development, pregnancy, application of external forces or disease (see 1.3.5). In flies it has also been shown that overexpression of vinculin influences cardiac architecture and increases the life span of animals [97].

In the fibroblast model I mimicked the effect of different amount of protein using co-transfection of constructs in a modified pLPCX (pLPCXmod) expression vector system. Western blots confirmed that the expression level of VV or MV constructs were comparable to vinculin levels of floxed (*vinc^{f/f}*) cells (Fig. 6.3 A).

FRAP experiments show that increasing the amount of protein leads to faster turnover rates and higher mobile fractions for both vinculin and metavinculin but the difference between the isoforms is even more pronounced and the effect on metavinculin turnover is weaker (Fig. 6.6). Faster turnover can be explained by faster re-binding of protein to unoccupied binding sites, e.g. on talin molecules. It is important to keep in mind that talin binding is important for (meta)vinculin localization at FA, but other binding partners like PIP₂ and unbound molecules also contribute to the observed FRAP signal.

The TS experiments show that force across VTS increases upon expression of additional vinculin or metavinculin, whereas force across MTS does not seem to be affected (Fig. 6.20 B). From immunoprecipitation experiments we know that 5-times more metavinculin is bound to talin-1 (Fig. 6.9 A & B). This suggests that there is still a large potential for vinculin to occupy additional binding sites on talin-1.

Data from single-molecule experiments lead to the conclusion that vinculin binds to talin in a cooperative manner and one binding triggers a series of other events [136]. Therefore a relatively moderate increase of vinculin concentration could already have a large effect on protein recruitment. It is also known, that once vinculin binds to talin-1 and is actively engaged with the actin cytoskeleton, previously cryptic VBSs open up [31, 32].

On the other hand, metavinculin binding to talin-1 could already be close to saturation and therefore might not be affected by expression of additional protein. However, it seems

that the presence of metavinculin does not alter the amount of force transduced across VTS compared to additional vinculin.

7.3.2 Association with the F-actin cytoskeleton

Introducing mutations into TS constructs enabled me to further understand how actin binding contributes to force transduction. The actin binding mutation I997A, which has been first described by [27], dramatically decreased force across VTS. An additional experiment to test the effects of F-actin binding on force across VTS would be mutation V1001A, which has been described to have an intermediate affinity [78].

Since the beginning of this thesis, two major contributions have been made by others to our understanding of how the metavinculin tail insert affects F-actin organization: in 2012 Janssen et al. [79] proposed that metavinculin promotes actin severing, however three years later this view was challenged by the observation that actin fragmentation does not occur in real time assays [80]. To date the most convincing conclusion from *in vitro* studies is that metavinculin results in a 2-fold reduced actin persistence length l_p , but does not lead to the sufficient structural changes to sever F-actin [80].

In immunostainings I did not observe changes in the global F-actin structure for cells expressing VV or MV, however, this does not exclude local changes. Measurement of the actin dynamics was beyond the scope of this thesis but in accordance with the molecular clutch hypothesis my prediction is that metavinculin is not able to slow down the retrograde flow of F-actin as much as vinculin does [27].

Comparison to other actin severing proteins reveals a 47% identity between gelsolin and the metavinculin insert from position 936-950 [79]. This region also contains the actin binding motif AAIVQLDDYL [132]. Interestingly, there is a gain of function mutation, which enables the only non-severing member of the gelsolin family CapG to sever actin [133]. I used this information about the CapG amino acid sequence to design my own metavinculin mutant.

Forces across MTS increased upon change of *DDY* to the non-severing *NTL* motif from the CapG amino acid sequence, indicating the importance of this region for mechanotransduction. This mutation of metavinculin has not been described in the literature before and has the potential to contribute to our understanding of fundamental differences between active severing and induction of mechanical discontinuities leading to actin fragmentation. This is also crucial to understand other severing molecules like ADF/cofilin [80]. Cryo-electron microscopy (EM) on the lamellipodia of VV and MV or superresolution microscopy could give insight into the size distribution and bending of actin filaments close to FA. In combination

with actin speckle microscopy, the relevance of metavinculin and especially the DDY motif for F-actin bundling might further be elucidated.

7.3.3 Effects of the HTI on force transduction

The HTI mutations severely affected FA and cell morphology for both vinculin and metavinculin, indicating large scale effects on FA and cytoskeletal organization. I observed hypertrophic FA, which were not able to disassemble and some cells showed protein accumulations.

While it is widely accepted that vinculin activation state is important for its localization and function at FA [25], it was not clear how the HTI interaction affects force transmission. I can state that force increases across both VTS and MTS when HTI is lowered (Fig. 6.21). This is the only experiment in which we observe FRET efficiency values for the MTS between 5 – 10%, which shows that it is indeed possible to increase the mean force across MTS. Similar to vinculin overexpression, increasing the amount of active vinculin protein could lead to a reinforcing effect caused by cooperative binding to talin.

7.3.4 Implications of reduced force transduction across metavinculin

Metavinculin expression could either provide resistance against external mechanical stimuli or uncouple the acto-myosin machinery from adhesion sites. It is stabilized at FA and could therefore also increase the stability of the talin scaffold and thus the remaining adhesion site.

Evidence accumulates that metavinculin indeed uncouples adhesion plaques from the cytoskeleton. This could either prevent high actomyosin generated forces to tear apart the adhesion or limit the size and strength of actin bundles, which could otherwise inhibit disassembling of adhesions and ultimately cause cells to be incapable of remodelling and migration.

8 Outlook

8.1 Future directions in the analysis of molecular biosensors

8.1.1 Measurements using linker peptides with different force regimes

As pointed out in the introduction, calibration of the linker peptide used for the tension sensor is necessary for the quantification of force. The mechanical properties of proteins can be determined using methods like atomic force microscopy (AFM) or optical traps. For this study, I used flagelliform peptide (F40) and HP35 linker, but other linkers can be employed as well. A stable form of the HP35 containing a point mutation shifts the highest force sensitivity to $9 - 11 pN$ [20] is currently tested to determine whether VTS and MTS are under high enough force to open up the stiff sensor. Using sensors with a higher initial FRET ratio should further increase our measurement precision [142].

8.1.2 Extending measurements to three-dimensional substrates

Over the last decades studying cell adhesion predominantly focused on the huge streak-like focal adhesion structures appearing when single cells spread on a solid extracellular matrix (ECM) coated support. This work is no exception and it is valid to generate experimental conditions which allow for sufficient amount of signal and enable the use of techniques such as total internal reflection microscopy (TIRF). However, the morphology which cells acquire under these conditions should not be overestimated as a read-out parameter and may be completely different in tissues, where forces are balanced between neighboring cells. Indeed, it has been shown that the effect of vinculin knockout on cell migration is reversed in three-dimensional collagen matrices with wildtype cells being three times more invasive than $\text{vinc}^{-/-}$ [143]. Vinculin seems to be important for the formation of protrusions and increasing persistence during cell migration in three-dimensional environments [144].

Another aspect which was at least partially addressed in this study, is the influence of substrate stiffness on cell differentiation and growth. I performed control experiments for

our TS measurements on 1.5 *kPa* and 15 *kPa*, however, under normal culture conditions cells were grown on plastic dishes. Future experiments could be optimized by growing cells on surfaces coated with PDMS or a similar elastic support over a longer time before analysis.

8.1.3 From whole cell analysis to force measurements at the adhesion level

Adhesions are dynamic structures with protein compositions depending on their history (nascent or assembling vs. disassembling) and position inside the cell. Within an adhesion proximal, central, and distal parts can be distinguished and a FA belt surrounding the adhesion sites exists. One mechanism, which has been proposed to structure adhesion sites, is the segregation of different integrin subtypes into separate clusters.

Over the past years, the VTS was adapted by various groups to measure how FA position and history influences intramolecular force. The most exhaustive analysis of the relationship between FA size and vinculin tension, including a theoretical model, was performed by [83]. They discovered a complex multi-modal behavior of correlations and distinguished force and size regimes with different properties. For example, force positively correlates with size in mid-sized FA whereas it shows a negative correlation in small and very large adhesions Hernandez-Varas et al. [83].

Compared to ratiometric FRET, lifetime imaging only provides a limited spatial and temporal resolution. Therefore analysis of FLIM data presented here does not take size and position of FA into account but averages over all adhesions.

Based on the observation that tension across MTS shows a lower variance between cells and is not influenced by protein stoichiometry I predict a weaker correlation of FA history and molecular tension. Indeed, comparing VTS, MTS and vinculin head tension sensor (VHTS) using ratiometric FRET and the analysis algorithms of Hernandez-Varras et al. [83] might give us further insight into metavinculin function. It would be interesting to know, whether MTS is independent of increase in FA area for parameter regions in which VTS shows a strong correlation.

8.2 Linking FA mechanotransduction to protein translation and alternative splicing

The story of metavinculin has always been fascinating because of the intriguingly complex expression level, which depends on cell type, mechanical stimulation, and other factors discussed in section 1.3.5. Studying how alternative splicing of the metavinculin isoform is regulated, would therefore greatly contribute to our understanding of the genetic foundation of mechanotransduction. Indeed, various pathways like MAPK, Wnt or MKL1/Srf signaling, link integrin adhesions to nuclear activity and a direct physical connection via the LINC (nesprin and SUN proteins) exists [145].

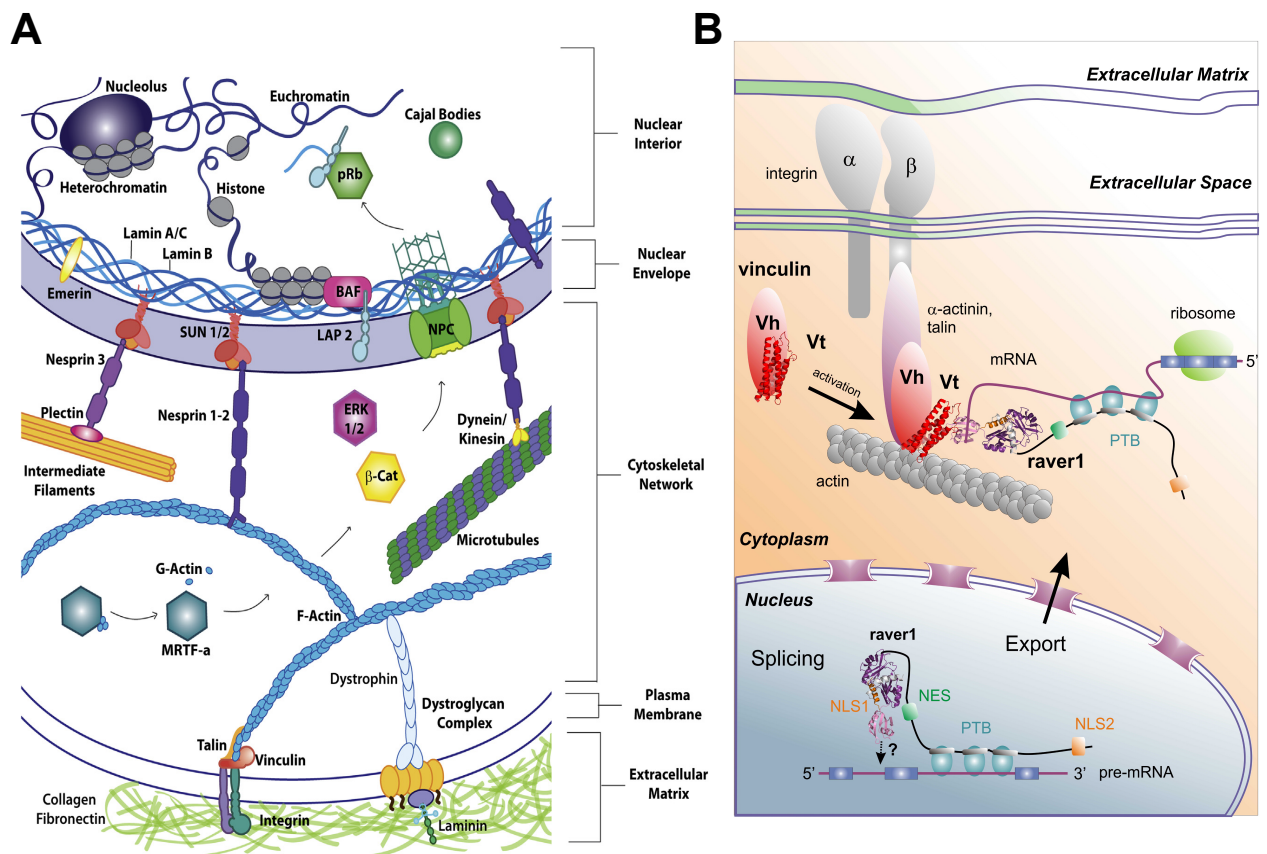


Figure 8.1: The role of vinculin in genetics **A.** Connections between FA sites and the nucleus. A direct physical link between the actin cytoskeleton and the nuclear membrane is mediated by nesprins and SUN proteins. This connection allows mechanical signals to directly reach the nucleus [145]. **B.** Illustration of the predicted role of Raver-1. It is present in the nucleus and the cytoplasm where it binds to activated vinculin which locks it at FA. This vinculin/Raver-1 complex could now bind mRNA and promote localized translation [146].

A second interesting topic is how local mRNA translation might be differentially regulated by vinculin and metavinculin. It was first proposed by Lee et al. [39] that activated vinculin

interacts with Raver-1 which could lead to production of FA components directly at adhesion sites [146]. The same group observed that metavinculin is capable of binding Raver-1 even in its closed state [40], opening up the possibility for an isoform-specific regulation of on-site transcription.

9 Summary

By generating metavinculin expressing cell lines and measuring intracellular forces with tension sensor (TS) constructs, I was able to approach the question how the 68 aa insert in the tail region alters protein function. Metavinculin is indeed able to take over part of vinculin functions at FAs where it localizes and can rescue spreading. I did not observe significant morphological differences between vinculin and metavinculin expressing cell lines, however, fluorescence recovery after photobleaching (FRAP) and mass spectrometry experiments revealed a reduced turnover of metavinculin and higher affinity for talin.

The main experimental challenge of this project was to set-up a pipeline for acquiring and evaluating time-correlated single photon counting (TCSPC)-fluorescence lifetime imaging microscopy (FLIM) data of Förster resonance energy transfer (FRET) constructs. Custom-written programs for analysis of FRET signal from FA are now routinely used by others. A metavinculin tension sensor (MTS) was generated in analogy to the previously published vinculin tension sensor (VTS) [10] and I observed decreased mean force across metavinculin for a range of substrate stiffnesses (fibronectin (FN) coated glass, 1.5 kPa, 15 kPa).

Force across metavinculin does not increase in the presence of vinculin, whereas vinculin force is aggravated upon increased expression of both vinculin and metavinculin. Therefore, I propose, that force is not shared between molecules but a different mechanism needs to reduce force across MTS.

Head-tail interaction (HTI) of metavinculin is lowered and it can therefore be kept in an open conformation and bind to talin, which enhances its stability in FAs. Furthermore, metavinculin seems to actively modulate F-actin binding by inducing mechanical instability through a gelsolin-like homology domain containing a DDY motif. It could therefore be used to reduce but not completely abolish transmission of forces from the cytoskeleton to the FA plaque. Further investigation is needed to reveal, how metavinculin changes actin flow rates and filament structure inside the cell.

To understand the role of metavinculin for the cell's interaction with its environment, I measured traction forces and subjected TS expressing cells to uniaxial stretching. However,

measuring changes in intracellular force upon external stretch will require further calibration measurements.

The main challenge for the future will be to translate our findings *in vivo* and find out more about the physiological role of metavinculin with a focus on its role in the development of disease. On the other hand, single molecule analysis of FRET biosensors in living cells will open up doors for a new understanding of protein dynamics. Molecular TS have proven to be powerful tools to unravel details of mechanotransduction, but only the knowledge of force distribution across individual proteins will unleash its whole strength.

10 Supplementary Material

10.1 Directory of used chemicals and antibodies

Laboratory equipment and pipetting material were supplied by Sarstedt, Schubert & Weiss, Kisker, Eppendorf and VWR. Restriction enzymes and buffers were purchased from New England Biolabs GmbH (NEB) and used according to manufacturers information. Common chemicals were purchased from Roth, Sigma or Life Technologies.

10.1.1 Materials for biochemistry

Product name	Supplier	Cat. No.
μ Columns	Miltenyi	130-042-701
μ MACS GFP Tagged Protein Isolation Kit	Miltenyi	130-091-125
μ MACS HA Tagged Protein Isolation Kit	Miltenyi	130-091-122
BCA Protein Assay Kit	Merck	71285-3
cOmplete ULTRA, mini, EDTA-free EASYpack	Roche	05892791001
Homogenizer 2 ml Dounce	VWR	SCERSP885300-0002
Immobilon Western Chemilumineszenz HRP Substrat	Merck	WBKLS0500
Immobilon-P Rolle	Merck	IPVH00010
Skim milk powder	AppliChem	A0830.0500
Mini-PROTEAN TGX Gels, 4 – 15 %, 30 μ l	Biorad	456-1083
PhosStop	Roche	04906837001
Ponceau S solution for electrophoresis (0.2 %)	Serva	33427.01
Prestained Protein Ladder (10 – 230 kDa)	NEB	P7710S
Prestained Protein Marker, Broad Range, pre-mixed	NEB	P7708L
Restore Plus Western Blot Stripping Buffer	Fisher Scientific	10016433

Table 10.1: Materials for biochemistry

10.1.2 Materials for cell culture

Product name	Supplier	Cat. No.
Blebbistatin	Sigma	B0560
μ -Dish 35 mm, ESS 1.5 kPa	Ibidi	81291
μ -Dish 35 mm, ESS 15 kPa	Ibidi	81391
0.5 % Trypsin-EDTA (10X), no Phenol Red	Life Technologies	15400054
BrdU Cell Proliferation Assay	Merck	QIA58-200TEST
Calyculin A	Sigma	C5552-10UG
Chloroquine diphosphate crystalline	Sigma	C6628
CYTOOchips 20x20 Starter's FN	CYTOO	10-900-10-06
CYTOOchips 20x20 Y-M-FN	CYTOO	10-011-10-06
DMEM, High Glucose, GlutaMAX, Pyruvate	Life Technologies	31966047
DMEM/F-12, GlutaMAX Supplement	Life Technologies	31331028
Fibronectin, Bovine Plasma	Merck	341631-5MG
Lipofectamine 2000 Transfection Reagent	Life Technologies	11668027
Opti-MEM I Reduced Serum Medium, GlutaMAX Supplement	Life Technologies	51985026
PBS Tabletten	Sigma	P4417-100TAB
Penicillin-Streptomycin (10,000 U/mL)	Life Technologies	15140122
Polybrene Infection/Transfection Reagent	Merck	TR-1003-G
Poly-L-Lysine 0.01 % solution mol. wt. 70,000-150,000	Sigma	P4707-50ML
Y-27632	Sigma	Y0505
Zählkammer Neubauer Improved H/1 O.kl.	VWR	630-1509

Table 10.2: Materials for cell culture

10.1.3 Materials for molecular biology

Product name	Supplier	Cat. No.
Alkaline Phosphatase CIP	NEB	M0290L
Ethidium bromide solution 1 %	Roth	2218.1
LB Agar (Luria/Miller), granulated	Roth	6675.2
mi-Plasmid Miniprep Kit	Metabion	mi-PMN250
NucleoBond Xtra Midi Plus	Macherey-Nagel	740412.50
NucleoSpin Gel and PCR Clean-up	Macherey-Nagel	740609.250
PfuUltra (TM) II Fusion HS DNA Polymerase, 200 rxn	Agilent	600672
Quick-Load 1 kb Extend DNA Ladder	NEB	N3239S
QuikChange II Site-Directed Mutagenesis Kit	Agilent	200523
SmartSeq Kit	Eurofins MWG	26000521
T4 DNA Ligase	NEB	M0202L
UltraPure Agarose	Life Technologies	16500500

Table 10.3: Materials for molecular biology

10.1.4 Materials and equipment used for microscopy

Product name	Supplier	Cat. No.
BrightLine HC 514/30	AHF	F37-514
BrightLine HC longpass-filter 593/LP	AHF	F37-594
Bandpass ET 545/30	AHF	F49-545
Bandpass ET 690/50	AHF	F47-690
ProLong Gold antifade reagent	Life Technologies	P36934
Rose Bengal dye	Sigma	R3877

Table 10.4: Materials and equipment used for microscopy

Antigene	Species	Label	Source	Cat No.	IF	WB
α -catenin	rabbit	-	Sigma	C2081	1/500	
α -Tubulin (37B5)	rat	-	Synaptic Systems	302217		1/20.000
β -catenin	mouse	-	Sigma	C 7207	1/500	
DAPI					1/10.000	
desmin					1/200	
FAK	rabbit	-	Milipore	06-543		1/1.000
GAPDH (6C5)	mouse	-	Calbiochem	CB1001		1/10.000
GFP	rabbit	-	abcam	ab290		1/2.000
GFP (GSN149)	mouse	-	Sigma	G1546		1/2.000
HA-Tag (6E2)	mouse	Alexa 647	Cell Sig- naling	3444		
HA-Tag (6E2)	mouse	Alexa 647	Cell Sig- naling	3444		1/2.000
mCherry [1C51]	mouse	-	abcam	ab125096		1/2.000
Metavinculin tail [6E3]	mouse	-	BSBS			1/10
Mouse IgG	chicken	Alexa 488	Invitrogen	A-21200	1/400	
Mouse IgG	goat	HRP	Biorad	170-6516		1/10.000
N-Cadherin	rabbit		Epitomics	2447-1	1/500	
Paxillin	mouse	-	BD	610051	1/400	1/2.000
Phalloidin	toxin	Alexa 488	Invitrogen	A12379	1/400	
Phalloidin	toxin	Alexa 647	Invitrogen	A22287	1/200	
P-Tyrosine [4G10]	mouse	-	Millipore	05-321		1/2.000
Rabbit IgG	chicken	Alexa 488	Invitrogen	A-21441	1/400	
Rabbit IgG	goat	HRP	Biorad	170-6515		1/10.000
Rat IgG	goat	Alexa 568	Invitrogen	A11077	1/400	
sm-actin	mouse	Cy3	Sigma	C6198	1/200	
Talin (8d4)	mouse	-	Sigma	T3287	1/400	1/2.000
Talin-1 [mono]	mouse	-	abcam	ab57758		1/2.000
Tubulin (DM1A)	mouse	-	Sigma	T9026		1/5.000
Vimentin					1/200	
Vinculin	mouse	-	Sigma	V9131	1/400	1/10.000
Vinculin- pY1065	rabbit	-	Invitrogen	44-1078G		1/1.000

Table 10.5: Used antibodies and dilutions

10.1.5 Materials used for biophysical experiments

Product name	Supplier	Cat. No.
Acrylamide 40 % solution	Sigma	A4058-100ML
Acrylamide/Bis Solution, 37.5:1 (30 % w/v)	Serva	10688.03
Dow Corning High-Vacuum Silicone Grease	Sigma	Z273554-1EA
FluoSpheres Carboxylate-Modified Microspheres, 0.04 μ m, red-orange fluorescent (565/580)	Life Technologies	F8794
FluoSpheres Carboxylate-Modified Microspheres, 0.2 μ m, crimson fluorescent (625/645)	Life Technologies	F8806
TEMED	Serva	35930.02
Ph-indicator stripes	VWR	1.09533.0001
Sulfo-SANPAH	Fisher Scientific	10474005
Sylgard 184 Elastomer Kit	VWR	634165S

Table 10.6: Materials used for biophysical experiments

10.2 Directory of oligonucleotides and cloned constructs

10.2.1 Oligonucleotides

No.	description	sequence
C1	vinc PCR primer ApaI forward	ATA GGG CCC ACC ATG CCA GTG TTT CAT ACG CGC ACG ATC G
C2	vinc PCR primer XbaI STOP re- verse	CGC TCT AGA CTA CTG GTA CCA GGG AGT CTT TCT AAC C
C3	vinc PCR primer XbaI noSTOP reverse	CGC TCT AGA CTG GTA CCA GGG AGT CTT TCT AAC C
C30	vinc PCR primer overlap PCR Sall-NotI linker 883	CGC GGC CGC ATA TAT GTC GAC TTC ATC CTT TTC CTC TGG TG
C31	vinc PCR primer overlap PCR Sall-NotI linker 884	ATA GTC GAC ATA TAT GCG GCC GCG GAG TTC CCT GAG CAG AAG GC
C32	vinc PCR primer NotI forward	ATG CGG CCG CGG AGT TCC CTG AGC AGA AGG CCG G
C33	vinc PCR primer NotI STOP for- ward	CAT GCG GCC GCC TAC TGG TAC CAG GGA GTC TTT CTA ACC
C48	vinc PCR primer AvrII forward	CCT CCA CCT AGG CCT CCA CCA CCA GAG GAA
C15	vinc QuikChange L234V for- ward	GAA GCT TTA AAA AAT CGC AAT TTT ACT GTA GAA AAA ATG AGT GCT GAA ATT AAT G
C16	vinc QuikChange L234V reverse	CAT TAA TTT CAG TCA TTT TTT CTA CAG TAA AAT TGC GAT TTT TTA AAG CTT C
C17	vinc QuikChange K142E for- ward	AGA GTT TGC AAA GGA ATT TTG GAA TAT CTT ACA GTG GCA GAG G
C18	vinc QuikChange K142E reverse	CCT CTG CCA CTG TAA GAT ATT CCA AAA TTC CTT TGC AAA CTC T
C34	vinc QuikChange N773A/E775A forward	GCT AAG AGG GAG GTG GAG GCT TCC GCG GAT CCC AAG TTC CGT GAG GCT GT
C35	vinc QuikChange N773A/E775A reverse	ACA GCC TCA CGG AAC TTG GGA TCC GCG GAA GCC TCC ACC TCC CTC TTA GC

No.	description	sequence
C42	vinc QuikChange L277M forward	ATT GGC CTC CAT AGA CTC CAA AAT GAA CCA GGC CAA AGG TTG GCT CCG TG
C43	vinc QuikChange L277M reverse	CAC GGA GCC AAC CTT TGG CCT GGT TCA TTT TGG AGT CTA TGG AGG CCA AT
C46	vinc QuikChange T12 forward	GCC AAG CAG TGC ACA GCT GCA GCG ATT GCA ACC AAC CTC TTA CAG G
C47	vinc QuikChange T12 reverse	CCT GTA AGA GGT TGG TTG CAA TCG CTG CAG CTG TGC ACT GCT TGG C
C73	vinc QuikChange I997A fwd	GCA CCC AGC TCA AAG CCC TGT CCA CAG TGA AGG
C74	vinc QuikChange I997A bkwd	CCT TCA CTG TGG ACA GGG CTT TGA GCT GGG TGC
C20	metavinc QuikChange A934V forward	GAG GCA GAT GCG GTC GAT GCT GCT GGC
C21	metavinc QuikChange A934V reverse	GCC AGC AGC ATC GAC CGC ATC TGC CTC
C24	metavinc QuikChange R975W forward	CGC GGC TCA GTC CTT GCA TTG GGA AGC TAC
C25	metavinc QuikChange R975W reverse	GTA GCT TCC CAA TGC AAG GAC TGA GCC GCG
C66	metavinc QuikChange DDY947DDA forward	GAC ATG GAA GAC GAT GCC GAA CCT GAG CTG CTG
C67	metavinc QuikChange DDY947DDA reverse	CAG CAG CTC AGG TTC GGC ATC GTC TTC CAT GTC
C68	metavinc QuikChange DDY947DDE forward	GAC ATG GAA GAC GAT GAG GAA CCT GAG CTG CTG
C69	metavinc QuikChange DDY947DDE reverse	CAG CAG CTC AGG TTC CTC ATC GTC TTC CAT GTC
C70	metavinc QuikChange DDY947DDF forward	GAC ATG GAA GAC GAT TTC GAA CCT GAG CTG CTG
C71	metavinc QuikChange DDY947DDF reverse	CAG CAG CTC AGG TTC GAA ATC GTC TTC CAT GTC
C62	metavinc primer overlap NotI forward	CTG TAC AAG GCG GCC GCG GAG TTC CCT G
C63	metavinc primer overlap NTL reverse	GGT TCC AAA GTG TTT TCC ATG TCA GGG GGG ACA GGG AAG CCA GCA GCA TCG GCC G
C64	metavinc primer overlap NTL forward	GGA AAA CAC TTT GGA ACC TGA GCT GCT GTT AAT GCC ATC CAA TCA GCC GGT CAA C
C4	vinc sequencing primer 1	CTT GGG CCA GAT TGA CGA G
C36	vinc sequencing primer 2	GCC TGG GCC AGC AAG GAC AC
C6	vinc sequencing primer 3	ACA GTG GAT GAC CGT GGA GT
C7	vinc sequencing primer 4	AGC TGC TTA TGA ACA TTT TGA GA

No.	description	sequence
C8	vinc sequencing primer 5	AGA CCT TGA ACA ACT CCG ACT AAC
C9	vinc sequencing primer 6	CTG CTG ATG GCT GAG ATG TC
C14	vinc sequencing start reverse	CAG AGA GGA TGC CCC TTG ACC C
C59	vinc sequencing VFC	CCC GGC CTT CTG CTC AGG GA
C10	venus PCR primer XbaI forward	GGC TCT AGA GGA GGG ATG GTG AGC AAG GGC GAG GAG C
C11	venus PCR primer NotI STOP reverse	ATA AGC GGC CGC TTA CTT GTA CAG CTC GTC CAT GCC G
C57	venus QuikChange Y66L forward	ACC ACC CTG GGC TTA GGC CTG CAG TGC TTC GC
C58	venus QuikChange Y66L reverse	GCG AAG CAC TGC AGG CCT AAG CCC AGG GTG GT
C19	mCherry Polymerase Chain Reaction (PCR) primer XbaI forward	GGC TCT AGA ATG GTG AGC AAG GGC GAG GAG G
C55	mCherry QuikChange Y71L forward	CCC TCA GTT CAT GTT AGG CTC CAA GGC CTA CG
C56	mCherry QuikChange Y71L reverse	CGT AGG CCT TGG AGC CTA ACA TGA ACT GAG GG
C49	TagBFP PCR primer XbaI forward	ACC AGT CTA GAG GAG GGA TGA GCG AGC TGAT T
C50	TagBFP PCR primer NotI STOP reverse	GCG GTG GGC GGC CGC TTA ATT AAG TTT GTG CC
C28	PCR primer pBSKΔNotI MCS forward	GGC CCG CAC CGC GGT GGT CAC CGC GAG CT
C29	PCR primer pBSKΔNotI MCS reverse	CGC GGT GAC CAC CGC GGT G

10.2.2 Cloned cDNA constructs

No.	plasmid description	abbreviation
156	pBSK + vinculin	
157	pBSK + metavinculin	
161	pBSK + vinculin-venus	
162	pBSK + metavinculin-venus	
167	pLPCXmod + metavinculin-venus.STOP	MV
168	pBSK + metavinculin-mCherry.STOP	
169	pLPCXmod + metavinculin-mCherry.STOP	MC
172	pLPCXmod + vinculin-venus.STOP	VV
177	pLPCXmod + metavinculin (R975W)-venus	MV-RW
178	pLPCXmod + metavinculin (A934V)-venus	MV-AV
199	pBSK +vinculin-mCherry.STOP	
204	pBSK- Δ N + vinculin (head)	
212	pLPCXmod + vinculin-mCherry.STOP	VC
213	pBSK- Δ N + metavinculin with Sall-NotI linker	
214	pBSK- Δ N + vinculin with Sall-NotI linker	
215	pLPCXmod + venus-F40-mCherry.STOP	TS
223	pLPCXmod + vinculin (head)-[venus-F40-mCherry].STOP	VHTS
227	pLPCXmod + vinculin (head)-[venus-F40-mCherry] (NoS-top)	
229	pBSK + metavinculin(R975W)-venus	
234	pLPCXmod + metavinculin-[venus-F40-mCherry] (internal)	MTS
235	pLPCXmod + metavinculin (R975W)-[venus-F40-mCherry] (internal)	RTS
236	pBSK + metavinculin(A934V)-venus	
237	pBSK- Δ N + vinculin-venus (internal)	
238	pBSK- Δ N + vinculin-mCherry (internal)	
250	pLPCXmod + vinculin(front; ApaI-EcoRI)	
254	pLPCXmod + vinculin-[venus-F40-mCherry] (internal)	VTS
255	pLPCXmod + metavinculin (A934V)-[venus-F40-mCherry] (internal)	
263	pLPCXmod + vinculin(head)-venus (NoStop)	
264	pLPCXmod + vinculin(head)-mCherry (NoStop)	
265	pLPCXmod- Δ CMV + metavinculin-[venus-F40-mCherry] (internal)	
267	pLPCXmod + vinculin-venus (internal)	VVi
268	pLPCXmod + vinculin-mCherry (internal)	VCi
287	pLPCXmod + vinculin-mCherry (internal)-venus.STOP	VAS
288	pLPCXmod + metavinculin-mCherry (internal)-venus.STOP	MAS
303	pLPCXmod + metavinculin (R975W)-mCherry (internal)-venus.STOP	RAS

No.	plasmid description	abbreviation
366	pLPCXmod + vinculin (N773A, E775A)-mCherry (internal)- venus.STOP	VAS-HTI
367	pLPCXmod + metavinculin (N773A, E775A)-mCherry (internal)-venus.STOP	MAS-HTI
368	pLPCXmod + metavinculin (R975W, N773A, E775A)- mCherry (internal)-venus.STOP	
389	pLPCXmod + metavinculin-mCherry(internal)	MCi
401	pBSK + vinculin(L277M) (NoStop)	
405	pLPCXmod + vinculin (L277M)-mCherry (internal)- venus.STOP	
406	pLPCXmod + vinculin (N773A, E775A)-[venus-F40- mCherry] (internal)	VTS-HTI
407	pLPCXmod + metavinculin (N773A, E775A)-[venus-F40- mCherry] (internal)	MTS-HTI
420	pLPCXmod + vinculin (N773A, E775A)-venus.STOP	VV-HTI
421	pLPCXmod + metavinculin (N773A, E775A)-venusSTOP	MV-HTI
431	pLPCXmod + metavinculin-venus (internal)	MVi
435	pBSK + vinculin-[venus-F40-mCherry].STOP	
436	pBSK + metavinculin-[venus-F40-mCherry].STOP	
437	pLPCXmod + vinculin-[venus-F40-mCherry].STOP	VTS-term
438	pLPCXmod + metavinculin-[venus-F40-mCherry].STOP	MTS-term
441	pLPCXmod + vinculin(head)-venus.STOP	VHV
442	pLPCXmod + vinculin(head)-mCherry.STOP	VHC
443	pBSK + vinculin-TagBFP.STOP	
444	pBSK + metavinculin-TagBFP.STOP	
445	pLPCXmod + vinculin-TagBFP.STOP	VB
446	pLPCXmod + metavinculin-TagBFP.STOP	MB
447	pBSK-ΔN + vinculin(head)-[YPet(short)-HP35- mCherry].STOP	
448	pBSK-ΔN + vinculin(head)-[YPet(short)-HP35-mCherry] (NoStop)	
449	pLPCXmod + vinculin(head)-[YPet(short)-HP35- mCherry].STOP	VHTS-villin
450	pLPCXmod + vinculin-[YPet(short)-HP35-mCherry] (inter- nal)	VTS-villin
451	pLPCXmod + metavinculin-[YPet(short)-HP35-mCherry] (internal)	MTS-villin
655	pLPCXmod + metavinculin (DDY947NTL)-[Venus-F40- mCherry] (internal)	MTS-CapG
674	pLPCXmod + metavinculin (DDY947DDA)-[Venus-F40- mCherry] (internal)	MTS-DDA
675	pLPCXmod + metavinculin (DDY947DDE)-[Venus-F40- mCherry] (internal)	MTS-DDE
676	pLPCXmod + metavinculin (DDY947DDF)-[Venus-F40- mCherry] (internal)	MTS-DDF
677	pLPCXmod + metavinculin (DDY947DDA)-Venus.STOP	MV-DDA
678	pLPCXmod + metavinculin (DDY947DDE)-Venus.STOP	MV-DDE
679	pLPCXmod + metavinculin (DDY947DDF)-Venus.STOP	MV-DDF
680	pLPCXmod + vinculin (I997A)-[Venus-F40-mCherry] (inter- nal)	VTS-I997A

11 Nomenclature of molecular mechanotransduction

cell mechanics

description of biophysical properties of a cell (e.g. elastic modulus, microrheological properties, mechanics of the cytoskeleton)

mechanotransduction (according to [nature.com/subjects/mechanotransduction](https://www.nature.com/subjects/mechanotransduction))

processes through which cells sense and respond to mechanical stimuli by converting them to biochemical signals that elicit specific cellular responses

active mechanotransduction (or inside-out signalling)

generation of traction forces to probe mechanical properties of the environment

passive mechanotransduction (or outside-in signalling)

detection of external forces and transduction into the cell

mechanotransducer (or molecular force-transmitter, mechano-coupler)

protein which is under mechanical load and directly transmits forces

mechanosensing [12]

the ability of a cell or tissue to detect the imposition of a force

mechanosensor

protein which changes its conformation, binding affinity or post-translational modification due to a direct mechanical stimulus

molecular strain gauge [13]

protein which unfurls binding domains for other proteins or signaling molecules upon force

mechanical signaling

signal transduction pathways which are activated by mechanical stimuli

rigidity sensing

change of cell morphology, migration or activation of signaling pathways in response to changes in substrate stiffness

Abbreviations

aa amino acids

Abl Abelson

ABS actin binding site

AFM atomic force microscopy

AHF AHF Analysentechnik

APS ammonium persulfate

ARL actin regulatory layer

AS activation sensor

ATP adenosine triphosphate

BCA bicinchoninic acid

bis-AA bis-acrylamide

BSA bovine serum albumin

CaCl₂ calcium chloride

CapG gelsolin like capping actin protein

Cat. No. Catalogue Number

cDNA complementary deoxyribonucleotide acid (DNA)

CIP calf-intestinal-phosphatase

CMV cytomegalovirus

CO₂ carbon dioxide

DCM dilated cardiomyopathy

ddH₂O Milli-Q filtered water

dH₂O distilled water

DMEM Dulbecco's Modified Eagle Medium

DMSO dimethylsulfoxide

DNA deoxyribonucleotide acid

dNTP deoxy nucleotide triphosphate

dsDNA double stranded DNA

DTT dithiothreitol

E. Coli *Escherichia Coli*

EBFP enhanced blue fluorescent protein

ECM extracellular matrix

EDTA ethylenediaminetetraacetic acid

EM electron microscopy

ESS elastic soft substrates

ethidium bromide 3,8-diamino-5-ethyl-6-phenylphenanthridiniumbromid

EtOH ethanol

F₄₀ flagelliform peptide

FA focal adhesion

FACS fluorescence-activated cell sorting

FAK focal adhesion kinase

FBS fetal bovine serum

FERM 4.1 protein, ezrin, radixin, moesin

FFT Fast Fourier transform

FLIM fluorescence lifetime imaging microscopy

FN fibronectin

FPGA field programmable gate array

FRAP fluorescence recovery after photobleaching

FRET Förster resonance energy transfer

FTL force transduction layer

FTTC Fourier transform traction cytometry

FX focal complex

GFP green fluorescent protein

GUI graphical user interface

HA human influenza hemagglutinin

HBS Hepes buffered saline

HCM hypertrophic cardiomyopathy

HEK 293 human embryonic kidney 293

Hepes 4-(2-hydroxyethyl)-1-piperazineethanesulfonic acid

HP₃₅ villin headpiece peptide

HTI head-tail interaction

HyD hybrid detector

IF immunofluorescence

ILK integrin-linked kinase

IpaA *Shigella* invasin
iPALM interferometric photoactivation localization microscopy
IPTG isopropyl- β -D-thiogalactopyranosid
IRF instrument response function
ISL integrin signaling layer
KCl potassium chloride
LB lysogeny broth
LBamp lysogeny broth (LB) with 50 $\frac{\mu\text{g}}{\text{ml}}$ ampicillin
Llph protein LLP homolog
LSM laser scanning microscope
MAS metavinculin activation sensor
MB metavinculin-enhanced blue fluorescent protein (EBFP)
MC metavinculin-mCherry
mCherry monomeric Cherry
MCI metavinculin-mCherry(internal)
MCS multiple cloning site
MEF mouse embryonic fibroblast
MPI Max Planck Institute
MTS metavinculin tension sensor
MV metavinculin-venus
MVi metavinculin-venus(internal)
MVt metavinculin tail domain
Na₂HPO₂ × 2 H₂O disodium hydrogen phosphate dihydrate
NaCl sodium chloride
NEB New England Biolabs GmbH
o/n overnight
OD optical density
PAA polyacrylamide
PBS phosphate buffered saline
pBSK pBlueskript
PCR Polymerase Chain Reaction
PDMS polydimethylsiloxane
PEG polyethylenglycol
PFA paraformaldehyde

PIP₂ phosphatidylinositol 4,5-bisphosphate
PIV particle image velocimetry
PKC α protein kinase C alpha
PLL poly-L-lysine
pLPCXmod modified pLPCX
PMSF phenylmethylsulfonyl fluoride
PMT photomultiplier
pN piconewton ($10^{-12}N$)
PTB phosphotyrosine binding
PVDF polyvinylidene difluoride

ROCK Rho-associated protein kinase
ROI region of interest
RT room temperature

s/p streptomycin/penicillin
SDS sodium dodecyl sulfate
SDS-PAGE sodium dodecyl sulfate (SDS)-polyacrylamide gel electrophoresis
SEM standard error of the mean
SMC smooth muscle cell
SMC-1A structural maintenance of chromosomes 1A

TAE tris-acetic acid-EDTA
TB terabyte
TBS tris buffered saline
TBS-T tris buffered saline (TBS) polysorbate 20 (Tween20)
TCSPC time-correlated single photon counting
TDC time-to-digital converter
TEMED N,N,N',N'-tetramethylethylenediamine
TFM traction force microscopy
TIRF total internal reflection microscopy
Tris 2-Amino-2-hydroxymethyl-propane-1,3-diol
TS tension sensor
Tween20 polysorbate 20

UV ultraviolet

VAS vinculin activation sensor
VASP vasodilator-stimulated phosphoprotein
VB vinculin-EBFP

VBS vinculin binding site

VC vinculin-mCherry

VCi vinculin-mCherry(internal)

Vh vinculin head domain

VHC vinculin-head-mCherry

VHTS vinculin head tension sensor

VHV vinculin-head-venus

Vt vinculin tail domain

VTS vinculin tension sensor

VV vinculin-venus

VVi vinculin-venus(internal)

w/o without

WB western blot

WLC worm-like chain

WLL white light laser

YFP yellow fluorescent protein

YPet(s) genetically truncated version of yellow fluorescent protein (YFP)

List of Tables

1.1	(Meta)vinculin expression in muscle	11
2.1	Factors disturbing live cell tension sensor experiments	19
4.1	Lysis buffer	28
4.2	Laemmli buffer	28
4.3	Running buffer	29
4.4	Stacking gel	29
4.5	Separating gel	29
4.6	Blotting buffer	30
4.7	TBS buffer	30
4.8	Mild stripping buffer	31
4.9	Binding buffer	32
4.10	Dialysis buffer	32
4.11	Storage buffer	33
4.12	F-buffer	33
4.13	Lysate without <i>Shigella</i> invasin (IpaA)	33
4.14	Lysate with IpaA	34
4.15	Freezing medium	34
4.16	Phoenix infection mix	36
4.17	HBS	36
4.18	PCR mix	37
4.19	Touchdown PCR	38
4.20	Overlap PCR	39
4.21	QuikChange PCR mix	39
4.22	QuikChange PCR	40
4.23	Digestion mix	40
4.24	TAE buffer	41
4.25	Loading buffer	41
4.26	Ligation mix	41
4.27	LB medium	42

4.28	PAA ratios	46
4.29	PAA 8kPa	46
4.30	PAA 15kPa	47
4.31	Microscope settings for used fluorophores and dyes	47
4.32	Killing buffer	50
4.33	Blocking solution	50
10.1	Materials for biochemistry	99
10.2	Materials for cell culture	100
10.3	Materials for molecular biology	101
10.4	Materials and equipment used for microscopy	101
10.5	Used antibodies and dilutions	102
10.6	Materials used for biophysical experiments	103

Bibliography

- [1] D. E. Jaalouk and J. Lammerding, "Mechanotransduction gone awry," *Nature reviews. Molecular Cell Biology*, vol. 10, pp. 63–73, 2009.
- [2] J. Lammerding, R. D. Kamm, and R. T. Lee, "Mechanotransduction in cardiac myocytes," *Annals of the New York Academy of Sciences*, vol. 00, no. 1, pp. 53–70, 2004.
- [3] V. Sequeira, L. L. M. Nijenkamp, J. Regan, and J. Van Der Velden, "The physiological role of cardiac cytoskeleton and its alterations in heart failure," *Biochimica et Biophysica Acta - Biomembranes*, vol. 1838, no. 2, pp. 700–722, 2014.
- [4] V. C. Vasile, W. D. Edwards, S. R. Ommen, and M. J. Ackerman, "Obstructive hypertrophic cardiomyopathy is associated with reduced expression of vinculin in the intercalated disc," *Biochemical and Biophysical Research Communications*, vol. 349, no. 2, pp. 709–15, 2006.
- [5] V. C. Vasile, S. R. Ommen, W. D. Edwards, and M. J. Ackerman, "A missense mutation in a ubiquitously expressed protein, vinculin, confers susceptibility to hypertrophic cardiomyopathy," *Biochemical and biophysical research communications*, vol. 345, no. 3, pp. 998–1003, 2006.
- [6] Q. S. Wells, N. L. Ausborn, B. H. Funke, J. P. Pfothenauer, J. L. Fredi, S. Baxter, T. G. DiSalvo, and C. C. Hong, "Familial dilated cardiomyopathy associated with congenital defects in the setting of a novel VCL mutation (Lys815Arg) in conjunction with a known MYPBC₃ variant," *Cardiogenetics*, vol. 1, no. 1, 2011.
- [7] T. M. Olson, "Metavinculin mutations alter actin interaction in dilated cardiomyopathy," *Circulation*, vol. 105, no. 4, pp. 431–437, 2002.
- [8] A. E. Zemljic-Harpf, J. C. Miller, S. a. Henderson, A. T. Wright, A. M. Manso, L. Elsherif, N. D. Dalton, A. K. Thor, G. a. Perkins, A. D. McCulloch, and R. S. Ross, "Cardiac-myocyte-specific excision of the vinculin gene disrupts cellular junctions, causing sudden death or dilated cardiomyopathy," *Molecular and Cellular Biology*, vol. 27, no. 21, pp. 7522–37, 2007.

- [9] J. R. Tangney, J. S. Chuang, M. S. Janssen, A. Krishnamurthy, P. Liao, M. Hoshijima, X. Wu, G. a. Meininger, M. Muthuchamy, A. Zemljic-Harpe, R. S. Ross, L. R. Frank, A. D. McCulloch, and J. H. Omens, "Novel role for vinculin in ventricular myocyte mechanics and dysfunction," *Biophysical Journal*, vol. 104, no. 7, pp. 1623–1633, 2013.
- [10] C. Grashoff, B. D. Hoffman, M. D. Brenner, R. Zhou, M. Parsons, M. T. Yang, M. a. McLean, S. G. Sligar, C. S. Chen, T. Ha, and M. a. Schwartz, "Measuring mechanical tension across vinculin reveals regulation of focal adhesion dynamics.," *Nature*, vol. 466, no. 7303, pp. 263–6, 2010.
- [11] J. Eyckmans, T. Boudou, X. Yu, and C. S. Chen, "A Hitchhiker's guide to mechanobiology," *Developmental Cell*, vol. 21, no. 1, pp. 35–47, 2011.
- [12] P. a. Janmey and R. T. Miller, "Mechanisms of mechanical signaling in development and disease.," *Journal of Cell Science*, vol. 124, pp. 9–18, 2011.
- [13] A. W. Holle and A. J. Engler, "More than a feeling: discovering, understanding, and influencing mechanosensing pathways," *Current Opinion in Biotechnology*, vol. 22, no. 5, pp. 648–654, 2011.
- [14] J. D. Humphrey, E. R. Dufresne, and M. Schwartz, "Mechanotransduction and extracellular matrix homeostasis," *Nature Reviews Molecular Cell Biology*, vol. 15, no. 12, pp. 802–812, 2014.
- [15] A. S. LaCroix, K. E. Rothenberg, and B. D. Hoffman, "Molecular-scale tools for studying mechanotransduction," *Annual Review of Biomedical Engineering*, vol. 17, pp. 071114–040531, 2015.
- [16] T. Iskratsch, H. Wolfenson, and M. P. Sheetz, "Appreciating force and shape — the rise of mechanotransduction in cell biology," *Nature Publishing Group*, vol. 15, no. 12, pp. 825–833, 2014.
- [17] S. Na, O. Collin, F. Chowdhury, B. Tay, M. Ouyang, Y. Wang, and N. Wang, "Rapid signal transduction in living cells is a unique feature of mechanotransduction.," *Proceedings of the National Academy of Sciences of the USA*, vol. 105, no. 18, pp. 6626–6631, 2008.
- [18] H. G. Hall and M. J. Bissell, "Characterization murine of the intermediate filament proteins mammary gland epithelial cells of the extracellular matrix (ECM)," vol. 162, pp. 379–389, 1986.
- [19] A. J. Engler, S. Sen, H. L. Sweeney, and D. E. Discher, "Matrix elasticity directs stem cell lineage specification," *Cell*, vol. 126, no. 4, pp. 677–689, 2006.

- [20] K. Austen, P. Ringer, A. Mehlich, A. Chrostek-Grashoff, C. Kluger, C. Klingner, B. Sabass, R. Zent, M. Rief, and C. Grashoff, "Extracellular rigidity sensing by talin isoform-specific mechanical linkages," *Nature Cell Biology*, 2015.
- [21] J. Y. Sim, J. Moeller, K. C. Hart, D. Ramallo, V. Vogel, A. R. Dunn, W. J. Nelson, and B. L. Pruitt, "Spatial distribution of cell-cell and cell-ECM adhesions regulates force balance while maintaining E-cadherin molecular tension in cell pairs," *Molecular Biology of the Cell*, vol. 26, no. 13, pp. 2456–2465, 2015.
- [22] M. Abercrombie and G. A. Dunn, "Adhesions of fibroblasts to substratum during contact inhibition observed by interference reflection microscopy," *Experimental Cell Research*, vol. 92, no. 1, pp. 57–62, 1975.
- [23] B. Alberts, D. Bray, J. Lewis, M. Raff, K. Roberts, and J. Watson, *Molecular Biology of the Cell*. Garland, 4th ed., 2002.
- [24] H. B. Schiller and R. Fässler, "Mechanosensitivity and compositional dynamics of cell–matrix adhesions," *Nature Publishing Group*, vol. 14, no. 6, pp. 509–519, 2013.
- [25] L. B. Case and C. M. Waterman, "Integration of actin dynamics and cell adhesion by a three-dimensional, mechanosensitive molecular clutch," *Nature Cell Biology*, vol. 17, no. 8, pp. 955–963, 2015.
- [26] G. Letort, H. Ennomani, L. Gressin, M. Théry, and L. Blanchoin, "Dynamic reorganization of the actin cytoskeleton," *F1000Research*, vol. 4, pp. 1–10, 2015.
- [27] I. Thievessen, P. M. Thompson, S. Berlemont, K. M. Plevock, S. V. Plotnikov, A. Zemljic-Harpf, R. S. Ross, M. W. Davidson, G. Danuser, S. L. Campbell, and C. M. Waterman, "Vinculin-actin interaction couples actin retrograde flow to focal adhesions, but is dispensable for focal adhesion growth," *Journal of Cell Biology*, vol. 202, no. 1, pp. 163–177, 2013.
- [28] B. D. Hoffman, C. Grashoff, and M. a. Schwartz, "Dynamic molecular processes mediate cellular mechanotransduction," *Nature*, vol. 475, no. 7356, pp. 316–323, 2011.
- [29] A. Banno and M. H. Ginsberg, "Integrin activation," *Thrombosis and Haemostasis*, vol. 86, no. 1, pp. 316–323, 2001.
- [30] P. Atherton, B. Stutchbury, D.-y. Wang, D. Jethwa, R. Tsang, E. Meiler-Rodriguez, P. Wang, N. Bate, R. Zent, I. L. Barsukov, B. T. Goult, D. R. Critchley, and C. Ballestrem, "Vinculin controls talin engagement with the actomyosin machinery," *Nature Communications*, vol. 6, pp. 1–12, 2015.

- [31] M. Yao, W. Qiu, R. Liu, A. K. Efremov, P. Cong, R. Seddiki, M. Payre, C. T. Lim, B. Ladoux, R.-M. Mège, and J. Yan, "Force-dependent conformational switch of α -catenin controls vinculin binding," *Nature communications*, vol. 5, p. 4525, 2014.
- [32] A. del Rio, R. Perez-Jimenez, R. Liu, P. Roca-Cusachs, J. M. Fernandez, and M. P. Sheetz, "Stretching single talin rod molecules activates vinculin binding.," *Science (New York, N.Y.)*, vol. 323, pp. 638–641, 2009.
- [33] C. Ciobanasu, B. Faivre, and C. Le Clainche, "Actomyosin-dependent formation of the mechanosensitive talin-vinculin complex reinforces actin anchoring.," *Nature Communications*, vol. 5, p. 3095, 2014.
- [34] I. Schoen, B. L. Pruitt, and V. Vogel, "The Yin-Yang of rigidity sensing: How forces and mechanical properties regulate the cellular response to materials," *Annual Review of Materials Research*, vol. 43, no. 1, pp. 589–618, 2013.
- [35] B. Geiger, "A 130K protein from chicken gizzard: its localization at the termini of microfilament bundles in cultured chicken cells.," *Cell*, vol. 18, no. 1, pp. 193–205, 1979.
- [36] M. G. Rubashkin, L. Cassereau, R. Bainer, C. C. DuFort, Y. Yui, G. Ou, M. J. Paszek, M. W. Davidson, Y.-Y. Chen, and V. M. Weaver, "Force engages vinculin and promotes tumor progression by enhancing PI3K activation of phosphatidylinositol (3,4,5)-triphosphate.," *Cancer Research*, vol. 74, no. 17, pp. 4597–611, 2014.
- [37] M. C. Subauste, O. Pertz, E. D. Adamson, C. E. Turner, S. Junger, and K. M. Hahn, "Vinculin modulation of paxillin-FAK interactions regulates ERK to control survival and motility," *The Journal of Cell Biology*, vol. 165, no. 3, pp. 371–81, 2004.
- [38] A. W. Holle, X. Tang, D. Vijayraghavan, L. G. Vincent, A. Fuhrmann, Y. S. Choi, J. C. Del Alamo, and Á. J. Engler, "In situ mechanotransduction via vinculin regulates stem cell differentiation," *Stem Cells*, vol. 31, pp. 2467–2477, 2013.
- [39] J. H. Lee, E. S. Rangarajan, S. D. Yogesha, and T. Izard, "Raver1 Interactions with Vinculin and RNA Suggest a Feed-Forward Pathway in Directing mRNA to Focal Adhesions," *Structure*, vol. 17, no. 6, pp. 833–842, 2009.
- [40] J. H. Lee, E. S. Rangarajan, C. Vonrhein, G. Bricogne, and T. Izard, "The metavinculin tail domain directs constitutive interactions with raver1 and vinculin RNA," *Journal of Molecular Biology*, vol. 422, pp. 697–704, 2012.

- [41] T. Izard, G. Tran Van Nhieu, and P. R. J. Bois, "Shigella applies molecular mimicry to subvert vinculin and invade host cells," *Journal of Cell Biology*, vol. 175, no. 3, pp. 465–475, 2006.
- [42] S. Saga, "Expression of metavinculin associated with differentiation of chicken embryonal muscle cells," *Proceedings of the National Academy of Sciences of the USA*, vol. 56, pp. 45–56, 1985.
- [43] J. R. Feramisco, J. E. Smart, K. Burrridge, D. M. Helfman, and G. P. Thomas, "Coexistence of vinculin and a vinculin-like protein of higher molecular weight in smooth muscle.," *Journal of Biological Chemistry*, vol. 257, no. 18, pp. 11024–11031, 1982.
- [44] S. Witt, A. Zieseniss, U. Fock, B. M. Jockusch, and S. Illenberger *The Journal of biological chemistry*.
- [45] X. Peng, E. S. Nelson, J. L. Maiers, and K. a. DeMali, "New insights into vinculin function and regulation," *International review of cell and molecular biology*, vol. 287, pp. 191–231, 2011.
- [46] W. H. Goldmann, "Role of vinculin in cellular mechanotransduction," *Cell Biology International*, vol. 40, no. 3, pp. 241–256, 2016.
- [47] P. M. Thompson, C. E. Tolbert, and S. L. Campbell, "Vinculin and metavinculin: Oligomerization and interactions with F-actin," *FEBS Letters*, vol. 587, pp. 1220–1229, 2013.
- [48] K. Chinthalapudi, E. S. Rangarajan, D. T. Brown, and T. Izard, "Differential lipid binding of vinculin isoforms promotes quasi-equivalent dimerization," *Proceedings of the National Academy of Sciences of the USA*, vol. 113, no. 34, pp. 9539–9544, 2016.
- [49] C. Bakolitsa, D. M. Cohen, L. a. Bankston, A. a. Bobkov, G. W. Cadwell, L. Jennings, D. R. Critchley, S. W. Craig, and R. C. Liddington, "Structural basis for vinculin activation at sites of cell adhesion.," *Nature*, vol. 430, no. 6999, pp. 583–6, 2004.
- [50] L. Molony and K. Burrridge, "Molecular shape and self-association of vinculin and metavinculin.," *Journal of cellular biochemistry*, vol. 29, pp. 31–36, 1985.
- [51] R. a. Borgon, C. Vonrhein, G. Bricogne, P. R. J. Bois, and T. Izard, "Crystal structure of human vinculin," *Structure*, vol. 12, pp. 1189–1197, 2004.
- [52] E. P. Moiseyeva, P. a. Weller, N. I. Zhidkova, E. B. Corben, B. Patel, I. Jasinska, V. E. Koteliansky, and D. R. Critchley, "Organization of the human gene encoding the cytoskeletal protein vinculin and the sequence of the vinculin promoter," *The Journal of Biological Chemistry*, vol. 268, no. 6, pp. 4318–25, 1993.

- [53] V. E. Koteliansky, E. P. Ogryzko, N. I. Zhidkova, P. a. Weller, D. R. Critchley, K. Vancompernelle, J. Vandekerckhove, P. Strasser, M. Way, and M. Gimona, “,” *FEBS Letters*, vol. 204, pp. 767–772, 1992.
- [54] E. S. Rangarajan, J. H. Lee, S. D. Yogesha, and T. Izard, “A helix replacement mechanism directs metavinculin functions,” *PloS One*, vol. 5, no. 5, p. e10679, 2010.
- [55] K. Chinthalapudi, E. S. Rangarajan, D. N. Patil, E. M. George, D. T. Brown, and T. Izard, “Lipid binding promotes oligomerization and focal adhesion activity of vinculin,” *The Journal of Cell Biology*, vol. 207, no. 5, pp. 643–656, 2014.
- [56] D. M. Cohen, H. Chen, R. P. Johnson, B. Choudhury, and S. W. Craig, “Two distinct head-tail interfaces cooperate to suppress activation of vinculin by talin,” *Journal of Biological Chemistry*, vol. 280, no. 17, pp. 17109–17117, 2005.
- [57] H. Chen, D. M. Cohen, D. M. Choudhury, N. Kioka, and S. W. Craig, “Spatial distribution and functional significance of activated vinculin in living cells,” *The Journal of Cell Biology*, vol. 169, no. 3, pp. 459–70, 2005.
- [58] J. L. Bays, X. Peng, C. E. Tolbert, C. Guilluy, A. E. Angell, Y. Pan, R. Superfine, K. Burridge, and K. DeMali, “Vinculin phosphorylation differentially regulates mechanotransduction at cell-cell and cell-matrix adhesions,” *Journal of Cell Biology*, vol. 205, no. 2, pp. 251–263, 2014.
- [59] K. Küpper, N. Lang, C. Möhl, N. Kirchgeßner, S. Born, W. H. Goldmann, R. Merkel, and B. Hoffmann, “Tyrosine phosphorylation of vinculin at position 1065 modifies focal adhesion dynamics and cell tractions,” *Biochemical and Biophysical Research Communications*, vol. 399, pp. 560–564, 2010.
- [60] C. E. Tolbert, P. M. Thompson, R. Super, K. Burridge, and S. L. Campbell, “Phosphorylation at Y1065 in Vinculin Mediates Actin Bundling, Cell Spreading, and Mechanical Responses to Force,” 2015.
- [61] Y. Huang, R. N. Day, and S. J. Gunst, “Vinculin phosphorylation at Tyr1065 regulates vinculin conformation and tension development in airway smooth muscle tissues,” *Journal of Biological Chemistry*, vol. 289, pp. 3677–3688, 2014.
- [62] J. Golji, T. Wendorff, and M. R. K. Mofrad, “Phosphorylation primes vinculin for activation,” *Biophysical Journal*, vol. 102, no. 9, pp. 2022–2030, 2012.
- [63] V. Auernheimer, L. Lautscham, M. Leidenberger, O. Friedrich, B. Kappes, B. Fabry, and W. H. Goldmann, “Vinculin phosphorylation at residues Y100 and Y1065 is required

- for cellular force transmission," *Journal of Cell Science*, vol. 128, no. 18, pp. 3435–3443, 2015.
- [64] A. Carisey and C. Ballestrem, "Vinculin, an adapter protein in control of cell adhesion signalling.," *European journal of Cell Biology*, vol. 90, no. 2-3, pp. 157–63, 2011.
- [65] A. Carisey, R. Tsang, A. M. Greiner, N. Nijenhuis, N. Heath, A. Nazgiewicz, R. Kemkemmer, B. Derby, J. Spatz, and C. Ballestrem, "Vinculin regulates the recruitment and release of core focal adhesion proteins in a force-dependent manner," *Current Biology*, vol. 23, pp. 271–281, 2013.
- [66] W. H. Ziegler, R. C. Liddington, and D. R. Critchley, "The structure and regulation of vinculin.," *Trends in Cell Biology*, vol. 16, no. 9, pp. 453–60, 2006.
- [67] F. Margadant, L. L. Chew, X. Hu, H. Yu, N. Bate, X. Zhang, and M. Sheetz, "Mechanotransduction in vivo by repeated talin stretch-relaxation events depends upon vinculin.," *PLoS Biology*, vol. 9, no. 12, p. e1001223, 2011.
- [68] H. Hirata, H. Tatsumi, C. T. Lim, and M. Sokabe, "Force-dependent vinculin binding to talin in live cells: a crucial step in anchoring the actin cytoskeleton to focal adhesions.," *American Journal of Physiology*, vol. 306, pp. C607–20, 2014.
- [69] I. Chandrasekar, T. E. B. Stradal, M. R. Holt, F. Entschladen, B. M. Jockusch, and W. H. Ziegler, "Vinculin acts as a sensor in lipid regulation of adhesion-site turnover.," *Journal of Cell Science*, vol. 118, pp. 1461–1472, 2005.
- [70] J. J. Otto, "The lack of interaction between vinculin and actin," *Cell Motility and the Cytoskeleton*, vol. 6, pp. 48–55, 1986.
- [71] R. P. Johnson and S. W. Craig, "F-actin binding site masked by the intramolecular association of vinculin head and tail domains.," *Nature*, vol. 373, pp. 261–264, 1995.
- [72] K. K. Wen, P. Rubenstein, and K. DeMali, "Vinculin nucleates actin polymerization and modifies actin filament structure," *Journal of Biological Chemistry*, vol. 284, no. 44, pp. 30463–30473, 2009.
- [73] C. Le Clainche, S. P. Dwivedi, D. Didry, and M. F. Carlier, "Vinculin is a dually regulated actin filament barbed end-capping and side-binding protein," *Journal of Biological Chemistry*, vol. 285, no. 30, pp. 23420–23432, 2010.
- [74] R. Bourdet-Sicard, M. Rüdiger, B. M. Jockusch, P. Gounon, P. J. Sansonetti, and G. T. Van Nhieu, "Binding of the *Shigella* protein IpaA to vinculin induces F-actin depolymerization," *EMBO Journal*, vol. 18, no. 21, pp. 5853–5862, 1999.

- [75] M. Rüdiger, N. K. P, C. S. Q, E. E. Weiss, and B. M. Jockusch, "Differential actin organization by vinculin isoforms : implications for cell type-specific microfilament anchorage," *FEBS Letters*, vol. 431, pp. 49–54, 1998.
- [76] C. E. Tolbert, K. Burridge, and S. L. Campbell, "Vinculin regulation of F-actin bundle formation: What does it mean for the cell?," *Cell Adhesion and Migration*, vol. 7, pp. 219–225, 2013.
- [77] M. E. W. Janssen, E. Kim, H. Liu, L. M. Fujimoto, A. Bobkov, N. Volkmann, and D. Hanein, "Three-dimensional structure of vinculin bound to actin filaments," *Molecular Cell*, vol. 21, pp. 271–281, 2006.
- [78] P. M. Thompson, C. E. Tolbert, K. Shen, P. Kota, S. M. Palmer, K. M. Plevock, A. Orlova, V. E. Galkin, K. Burridge, E. H. Egelman, N. V. Dokholyan, R. Superfine, and S. L. Campbell, "Identification of an actin binding surface on vinculin that mediates mechanical cell and focal adhesion properties," *Structure*, vol. 22, no. 5, pp. 697–706, 2014.
- [79] M. E. W. Janssen, H. J. Liu, N. Volkmann, and D. Hanein, "The C-terminal tail domain of metavinculin, vinculin's splice variant, severs actin filaments," *Journal of Cell Biology*, vol. 197, pp. 585–593, 2012.
- [80] Z. a. Oztug Durer, R. M. McGillivray, H. Kang, W. A. Elam, C. L. Vizcarra, D. Hanein, E. M. De La Cruz, E. Reisler, and M. E. Quinlan, "Metavinculin tunes the flexibility and the architecture of vinculin induced bundles of actin filaments.," *Journal of molecular biology*, vol. 427, no. 17, pp. 2782–2798, 2015.
- [81] G. Diez, V. Auernheimer, B. Fabry, and W. H. Goldmann, "Head/tail interaction of vinculin influences cell mechanical behavior," *Biochemical and Biophysical Research Communications*, vol. 406, no. 1, pp. 85–88, 2011.
- [82] C.-W. Chang and S. Kumar, "Vinculin tension distributions of individual stress fibers within cell-matrix adhesions.," *Journal of Cell Science*, vol. 126, pp. 3021–30, 2013.
- [83] P. Hernández-Varas, U. Berge, J. G. Lock, and S. Strömblad, "A plastic relationship between vinculin-mediated tension and adhesion complex area defines adhesion size and lifetime," *Nature Communications*, vol. 6, p. 7524, 2015.
- [84] K. E. Rothenberg, S. S. Neibart, A. S. LaCroix, and B. D. Hoffman, "Controlling Cell Geometry Affects the Spatial Distribution of Load Across Vinculin," *Cellular and Molecular Bioengineering*, vol. 8, no. 3, pp. 364–382, 2015.

- [85] M. a. Glukhova, a. E. Kabakov, M. G. Frid, O. I. Ornatsky, a. M. Belkin, D. N. Mukhin, a. N. Orekhov, V. E. Koteliansky, and V. N. Smirnov, "Modulation of human aorta smooth muscle cell phenotype: a study of muscle-specific variants of vinculin, caldesmon, and actin expression.," *Proceedings of the National Academy of Sciences of the USA*, vol. 85, no. 24, pp. 9542–6, 1988.
- [86] A. M. Belkin, O. I. Ornatsky, A. E. Kabakov, M. A. Glukhova, and V. E. Kotelianskys, "Expression of muscle specific variants of vinculin in humans," *Biochemistry*, no. 14, pp. 6631–6635, 1988.
- [87] F. Thoss, F. Dietrich, K. Punkt, S. Illenberger, K. Rottner, M. Himmel, and W. H. Ziegler, "Metavinculin: New insights into functional properties of a muscle adhesion protein," *Biochemical and Biophysical Research Communications*, vol. 430, pp. 7–13, 2013.
- [88] A. Chopard, F. Pons, and J.-F. Marini, "Vinculin and meta-vinculin in fast and slow rat skeletal muscle before and after hindlimb suspension," *European Journal of Physiology*, vol. 444, no. 5, pp. 627–33, 2002.
- [89] R. Li, M. V. Narici, R. M. Erskine, O. R. Seynnes, J. Rittweger, R. Pišot, B. Šimunič, and M. Flück, "Costamere remodeling with muscle loading and unloading in healthy young men," *Journal of Anatomy*, vol. 223, pp. 525–536, 2013.
- [90] M. Rezvani and C. M. E. H. H. D. A. Ornatsky, Olga, "Dystrophin, vinculin, and aciculin in skeletal muscle subject to chronic use and disuse," *Medicine & Science in Sports & Exercise*, vol. 28, no. 1, pp. 79–84, 1996.
- [91] M. Girard, F. Dohme-Meier, P. Silacci, S. Ampuero Kragten, M. Kreuzer, and G. Bee, "Forage legumes rich in condensed tannins may increase n-3 fatty acid levels and sensory quality of lamb meat," *Journal of the Science of Food and Agriculture*, 2015.
- [92] K. S. Rehman, S. Yin, B. A. Mayhew, R. A. Word, and W. E. Rainey, "Human myometrial adaptation to pregnancy: cDNA microarray gene expression profiling of myometrium from non-pregnant and pregnant women," *Molecular Human Reproduction*, vol. 9, no. 11, pp. 681–700, 2003.
- [93] S. Klossner, R. Li, S. Ruoss, A.-C. Durieux, and M. Flück, "Quantitative changes in focal adhesion kinase and its inhibitor, FRNK, drive load-dependent expression of costamere components," *American Journal of Physiology*, vol. 305, no. 6, pp. R647–57, 2013.
- [94] W. Xu, J. L. Coll, and E. D. Adamson, "Rescue of the mutant phenotype by reexpression of full-length vinculin in null F9 cells; effects on cell locomotion by domain deleted vinculin," *Journal of Cell Science*, vol. 111, pp. 1535–44, 1998.

- [95] A. E. Zemljic-harpf, S. Ponrartana, R. T. Avalos, M. C. Jordan, K. P. Roos, N. D. Dalton, V. Q. Phan, E. D. Adamson, and R. S. Ross, "Animal model heterozygous inactivation of the vinculin gene," *Microscopy*, vol. 165, no. 3, pp. 1033–1044, 2004.
- [96] S. Marg, U. Winkler, M. Sestu, M. Himmel, M. Schönherr, J. Bär, A. Mann, M. Moser, C. T. Mierke, K. Rottner, M. Blessing, J. Hirrlinger, and W. H. Ziegler, "The vinculin-DeltaIn20/21 mouse: characteristics of a constitutive, actin-binding deficient splice variant of vinculin.," *PloS One*, vol. 5, no. 7, p. 11530, 2010.
- [97] G. Kaushik, A. Spenlehauer, A. O. Sessions, A. S. Trujillo, A. Fuhrmann, Z. Fu, V. Venkatraman, D. Pohl, J. Tuler, M. Wang, E. G. Lakatta, K. Ocorr, R. Bodmer, S. I. Bernstein, J. E. Van Eyk, A. Cammarato, and A. J. Engler, "Vinculin network-mediated cytoskeletal remodeling regulates contractile function in the aging heart," *Science translational medicine*, vol. 7, no. 292, p. 292ra99, 2015.
- [98] T. Meyer, U. Brink, C. Unterberg, S. Stöhr, H. Kreuzer, and a. B. Buchwald, "Expression of meta-vinculin in human coronary arteriosclerosis is related to the histological grade of plaque formation.," *Atherosclerosis*, vol. 111, pp. 111–119, 1994.
- [99] C. P. Metavinculin, "Dilated cardiomyopathy associated with deficiency of the dilated cardiomyopathy," *Cardiology*, pp. 1–6.
- [100] J. R. Lakowicz, *Principles of Fluorescence Spectroscopy*. Springer US, 2006.
- [101] A. L. Cost, P. Ringer, A. Chrostek-Grashoff, and C. Grashoff, "How to measure molecular forces in cells: A guide to evaluating genetically-encoded FRET-based tension sensors," *Cellular and Molecular Bioengineering*, vol. 8, no. 1, pp. 96–105, 2015.
- [102] F. Meng and F. Sachs, "Visualizing dynamic cytoplasmic forces with a compliance-matched FRET sensor," *Journal of Cell Science*, vol. 124, no. Pt 2, pp. 261–269, 2011.
- [103] D. R. Stabley, C. Jurchenko, S. S. Marshall, and K. S. Salaita, "Visualizing mechanical tension across membrane receptors with a fluorescent sensor," *Nature Methods*, vol. 9, no. 1, pp. 64–67, 2011.
- [104] J. Marko, E. Siggia, and S. Smith, "Entropic Elasticity of X-Phage DNA Explicit and Implicit Learning and Maps of Cortical Motor Output," *Science*, vol. 265, no. 5178, pp. 1599–1600, 1994.
- [105] K. Austen, C. Kluger, A. Freikamp, A. Chrostek-Grashoff, and C. Grashoff, *Generation and Analysis of Biosensors to Measure Mechanical Forces Within Cells*, pp. 169–184. Totowa, NJ: Humana Press, 2013.

- [106] P. E. Morton and M. Parsons, "Dissecting cell adhesion architecture using advanced imaging techniques," *Cell Adhesion & Migration*, vol. 5, no. 4, pp. 351–359, 2011.
- [107] S. V. Plotnikov and C. M. Waterman, "Guiding cell migration by tugging," *Current Opinion in Cell Biology*, vol. 25, no. 5, pp. 619–626, 2013.
- [108] U. S. Schwarz and J. R. D. Soiné, "Traction force microscopy on soft elastic substrates: A guide to recent computational advances.," *Biochimica et biophysica acta*, vol. 1853, no. 11, pp. 3095–3104, 2015.
- [109] U. S. Schwarz and S. A. Safran, "Physics of adherent cells," *Reviews of Modern Physics*, vol. 85, no. 3, pp. 1327–1381, 2013.
- [110] U. Faust, N. Hampe, W. Rubner, N. Kirchgeßner, S. Safran, B. Hoffmann, and R. Merkel, "Cyclic stress at mHz frequencies aligns fibroblasts in direction of zero strain," *PLoS One*, vol. 6, no. 12, 2011.
- [111] Y. Aratyn-Schaus, P. W. Oakes, J. Stricker, S. P. Winter, and M. L. Gardel, "Preparation of compliant matrices for quantifying cellular contraction.," *Journal of visualized experiments : JoVE*, no. 46, pp. 1–6, 2010.
- [112] B. Sabass, M. L. Gardel, C. M. Waterman, and U. S. Schwarz *Biophysical journal*.
- [113] N. Q. Balaban, U. S. Schwarz, D. Riveline, P. Goichberg, G. Tzur, I. Sabanay, D. Mahalu, S. Safran, a. Bershadsky, L. Addadi, and B. Geiger, "Force and focal adhesion assembly: a close relationship studied using elastic micropatterned substrates.," *Nature Cell Biology*, vol. 3, no. 5, pp. 466–72, 2001.
- [114] L. Trichet, J. Le Digabel, R. J. Hawkins, S. R. K. Vedula, M. Gupta, C. Ribault, P. Hersen, R. Voituriez, and B. Ladoux, "Evidence of a large-scale mechanosensing mechanism for cellular adaptation to substrate stiffness," *Proceedings of the National Academy of Sciences*, vol. 109, pp. 6933–6938, 2012.
- [115] M. Morimatsu, A. H. Mekhdjian, A. S. Adhikari, and A. R. Dunn
- [116] A. D. Bershadsky, N. Q. Balaban, and B. Geiger, "Adhesion-dependent cell mechanosensitivity.," *Annual review of cell and developmental biology*, vol. 19, pp. 677–695, 2003.
- [117] P. W. Oakes and M. L. Gardel, "Stressing the limits of focal adhesion mechanosensitivity," *Current Opinion in Cell Biology*, vol. 30, pp. 68–73, 2014.
- [118] M. Théry, "Micropatterning as a tool to decipher cell morphogenesis and functions," *Journal of Cell Science*, vol. 123, pp. 4201–13, 2010.

- [119] E. A. Cavalcanti-Adam, T. Volberg, A. Micoulet, H. Kessler, B. Geiger, and J. P. Spatz, "Cell spreading and focal adhesion dynamics are regulated by spacing of integrin ligands," *Biophysical journal*, vol. 92, no. 8, pp. 2964–74, 2007.
- [120] D. E. Discher, P. Janmey, and Y.-L. Wang, "Tissue cells feel and respond to the stiffness of their substrate," *Science (New York, N.Y.)*, vol. 310, no. 5751, pp. 1139–43, 2005.
- [121] A. Elosegui-Artola, E. Bazellières, M. D. Allen, I. Andreu, R. Oria, R. Sunyer, J. J. Gomm, J. F. Marshall, J. L. Jones, X. Trepata, and P. Roca-Cusachs, "Rigidity sensing and adaptation through regulation of integrin types," *Nature Materials*, vol. 13, pp. 631–637, 2014.
- [122] Y. Chen, A. A. M. Pasapera, A. P. Koretsky, and C. M. Waterman, "Orientation-specific responses to sustained uniaxial stretching in focal adhesion growth and turnover," *Proceedings of the National Academy of Sciences of the USA*, vol. 110, pp. E2352–61, 2013.
- [123] A. Livne, E. Bouchbinder, and B. Geiger, "Cell reorientation under cyclic stretching," *Nature Communications*, vol. 5, p. 3938, 2014.
- [124] N. Bonakdar, J. Luczak, L. Lautscham, M. Czonstke, T. M. Koch, A. Mainka, T. Jungbauer, W. H. Goldmann, R. Schröder, and B. Fabry, "Biomechanical characterization of a desminopathy in primary human myoblasts," *Biochemical and Biophysical Research Communications*, vol. 419, no. 4, pp. 703–707, 2012.
- [125] D. Tambe, C. Hardin, T. Angelini, K. Rajendran, C. Park, X. Serra-Picamal, E. Zhou, M. Zaman, J. Butler, D. Weitz, J. Fredberg, and X. Trepata, "Collective cell guidance by cooperative intercellular forces," *Nature Materials*, vol. 10(6), pp. 469–75, 2011.
- [126] S. Swift, J. Lorens, P. Achacoso, and G. P. Nolan, "Rapid production of retroviruses for efficient gene delivery to mammalian cells using 293T cell-based systems," *Current protocols in immunology / edited by John E. Coligan ... [et al.]*, vol. Chapter 10, p. Unit 10.17C, 2001.
- [127] M. Szabelski, R. Luchowski, Z. Gryczynski, P. Kapusta, U. Ortmann, and I. Gryczynski, "Evaluation of instrument response functions for lifetime imaging detectors using quenched Rose Bengal solutions," *Chemical Physics Letters*, vol. 471, no. 1-3, pp. 153–159, 2009.
- [128] B. L. Sprague, R. L. Pego, D. a. Stavreva, and J. G. McNally *Biophysical journal*.
- [129] S. V. Plotnikov, B. Sabass, U. S. Schwarz, and C. M. Waterman, "High-resolution traction force microscopy," vol. 123, pp. 367–394, 2014.

- [130] C. Möhl, N. Kirchgeßner, C. Schäfer, K. Küpper, S. Born, G. Diez, W. H. Goldmann, R. Merkel, and B. Hoffmann, "Becoming stable and strong: The interplay between vinculin exchange dynamics and adhesion strength during adhesion site maturation," *Cell Motility and the Cytoskeleton*, vol. 66, pp. 350–364, 2009.
- [131] B. Seefeldt, R. Kasper, T. Seidel, P. Tinnefeld, K. J. Dietz, M. Heilemann, and M. Sauer, "Fluorescent proteins for single-molecule fluorescence applications," *Journal of Biophotonics*, vol. 1, no. 1, pp. 74–82, 2008.
- [132] G. S. Withers, "Structure of gelsolin segment 1-actin complex and the mechanism of filament severing," *Nature*, vol. 363, 1993.
- [133] Y. Zhang, S. M. Vorobiev, B. G. Gibson, B. Hao, G. S. Sidhu, V. S. Mishra, E. G. Yarmola, M. R. Bubb, S. C. Almo, and F. S. Southwick, "A CapG gain-of-function mutant reveals critical structural and functional determinants for actin filament severing," *The EMBO journal*, vol. 25, no. 19, pp. 4458–67, 2006.
- [134] M. Gimona, J. V. Small, M. Moeremans, J. van Damme, M. Puype, and J. Vandekerckhove, "Molecular domain structure of porcine vinculin and metavinculin," *Protoplasma*, vol. 145, no. 2, pp. 133–140, 1988.
- [135] A. M. Pasapera, I. C. Schneider, E. Rericha, D. D. Schlaepfer, and C. M. Waterman, "Myosin II activity regulates vinculin recruitment to focal adhesions through FAK-mediated paxillin phosphorylation," *Journal of Cell Biology*, vol. 188, no. 6, pp. 877–890, 2010.
- [136] X. Hu, C. Jing, X. Xu, N. Nakazawa, V. W. Cornish, F. M. Margadant, and M. P. Sheetz, "Cooperative vinculin binding to talin mapped by time-resolved super resolution microscopy," *Nano Letters*, vol. 16, no. 7, pp. 4062–4068, 2016.
- [137] M. a. Digman, P. W. Wiseman, C. Choi, A. R. Horwitz, and E. Gratton, "Stoichiometry of molecular complexes at adhesions in living cells," *Proceedings of the National Academy of Sciences of the USA*, vol. 106, no. 7, pp. 2170–2175, 2009.
- [138] M. a. Digman, C. M. Brown, A. R. Horwitz, W. W. Mantulin, and E. Gratton, "Paxillin dynamics measured during adhesion assembly and disassembly by correlation spectroscopy," *Biophysical journal*, vol. 94, no. 7, pp. 2819–2831, 2008.
- [139] J. D. Siliciano and S. W. Craig, "Properties of smooth muscle meta-vinculin.," *The Journal of Cell Biology*, vol. 104, no. 3, pp. 473–482, 1987.

- [140] A. Benda, V. Fagul'ová, A. Deyneka, J. Enderlein, and M. Hof, "Fluorescence lifetime correlation spectroscopy combined with lifetime tuning: New perspectives in supported phospholipid bilayer research," *Langmuir*, vol. 22, no. 033106, pp. 9580–9585, 2006.
- [141] T. Robinson, Y. Schaerli, R. Wootton, F. Hollfelder, C. Dunsby, G. Baldwin, M. Neil, P. French, and A. DeMello, "Removal of background signals from fluorescence thermometry measurements in PDMS microchannels using fluorescence lifetime imaging," *Lab on a chip*, vol. 9, pp. 3437–3441, 2009.
- [142] J. Fang, A. Mehlich, N. Koga, J. Huang, R. Koga, X. Gao, C. Hu, C. Jin, M. Rief, J. Kast, D. Baker, and H. Li, "Forced protein unfolding leads to highly elastic and tough protein hydrogels," *Nature communications*, vol. 4, p. 2974, 2013.
- [143] C. T. Mierke, P. Kollmannsberger, D. P. Zitterbart, G. Diez, T. M. Koch, S. Marg, W. H. Ziegler, W. H. Goldmann, and B. Fabry, "Vinculin facilitates cell invasion into three-dimensional collagen matrices," *The Journal of Biological Chemistry*, vol. 285, no. 17, pp. 13121–30, 2010.
- [144] I. Thievensen, N. Fakhri, J. Steinwachs, V. Kraus, R. S. McIsaac, L. Gao, B.-C. Chen, M. Baird, M. W. Davidson, E. Betzig, R. Oldenbourg, C. M. Waterman, and B. Fabry, "Vinculin is required for cell polarization, migration, and extracellular matrix remodeling in 3D collagen," *The FASEB Journal*, pp. 1–13, 2015.
- [145] G. R. Fedorchak, A. Kaminski, and J. Lammerding, "Cellular mechanosensing: Getting to the nucleus of it all," *Progress in Biophysics and Molecular Biology*, vol. 115, no. 2-3, pp. 76–92, 2014.
- [146] T. Madl and M. Sattler, "Adhesion Dance with Raver," *Structure*, vol. 17, no. 6, pp. 781–783, 2009.

Publications

Austen, K.*; **Kluger, C.***; Freikamp, A*.; Chrostek-Grashoff, A.; Grashoff, C. (2013)

“Generation and analysis of biosensors to measure mechanical forces within cells.”

Methods in molecular biology 1066, 169-184

* equal contribution

Austen, K.; Ringer, P.; Mehlich, A.; Chrostek-Grashoff, A.; **Kluger, C.**; Klingner, C.; Sabass, B.; Zent, R.; Rief, M.; Grashoff, C. (2015)

“Extracellular rigidity sensing by talin isoform-specific mechanical linkages.”

Nature cell biology, 17,1597–1606

Acknowledgments

Many people have been involved in this Phd thesis, either by direct contribution to the project or by creating a perfect environment to do science. The most important person was without a doubt Dr. Carsten Grashoff, who not only designed and supervised the project, but also greatly influenced my personal development during the last years. Thank you for many hours of intense scientific discussion, during which you tried to guide me into the right direction and helped me to distinguish solid experiments and indispensable controls from time-consuming side projects.

I am very grateful that Prof. Hermann Gaub agreed to supervise and examine my thesis and would like to thank him and the other members of the thesis examination committee for their time and effort. Together with Dr. Martin Benoit, Prof. Steffen Massberg and Prof. Thorsten Hugel he was also part of the Thesis Advisory Committee (TAC), which regularly controlled the progress of my work. Preparing these TAC meetings was never a burden and I really appreciated the new and fresh ideas as well as the critical questions on the project. Prof. Reinhard Fässler was very generous in providing our group with access to all facilities of his department and it was always interesting to exchange thoughts and ideas with members of his group and participate in the department seminars.

During this project I received a lot of help from our external collaborators: Dr. Benedikt Sabass performed the analysis of the traction force data and guided me to set up the TFM experiments, Nico Hampe from the group of Prof. Rudi Merkel helped me to fabricate chambers for cell stretching and Prof. David Boettiger introduced me to cell adhesion measurements.

For our mass spectrometry analysis it was great to receive help directly from the MPI: Dr. Marco Hein from the group of Prof. Matthias Mann and Dr. Nagaraj Nagarjuna from the Core Facility performed experiments as well as data analysis. I also would like to thank Dr. Julien Polleux for help with micropatterning and fruitful discussions about a large variety of scientific topics.

I will really miss the great atmosphere in the lab and all the people who contributed so largely to my knowledge of biochemistry and transformed me from a physicist to a real

biophysicist.

First, I would like to thank Dr. Anna Chrostek-Grashoff for her structured way to organize a lab in which everything is always available and at the right position (with the right label on top (in the right color)). Thank you for your patience and help with all issues of daily lab work and beyond.

In chronological order of their appearance the following people joined the lab as a graduate student or postdoc: Dr. Katharina Austen, Pia Ringer, Andrea Freikamp, Anna-Lena Cost, Christoph Klingner and finally Verena Kanoldt. Matthias Morasch, Robert Cohen and Gerrit Huy all worked for some time on smaller projects. I want to thank all of them for their continuous support, advice and cheerfulness. It was great to work among people from so many different scientific backgrounds and each new person added even more spirit to our discussions.

From the very beginning, Kathi was the "talin" bridging between our groups and the neighboring labs. Thank you for trying to teach us volleyball, there will always be a direct connection in my brain linking you to this sport. The great thing about Pia is that she never stops to ask questions - and never stops trying to answer them. Thank you for your really genuine curiosity and your liveliness which always impressed me. Andrea has been the perfect person to share a hot cup of coffee and talk about everything, no matter how much or little science involved. Thank you for sometimes looking at things in exactly the opposite way I do and teaching me so many small tricks and facts about lab work. When Christoph joined the lab as a postdoc I was not only happy that he was a physicist but also that it was him. Thank you for lengthy, twisting, serious and not so serious discussions on all kinds of "side projects" and sharing worldly wisdom as well as workarounds for Matlab problems. Verena only joined the lab during the last months and I would have really liked to spend more time around her. Thank you for bringing new ideas into the group and all the best for the future work on metavinculin.

No, I didn't forget about Anna-Lena. Thank you for supervising me during your master's thesis and also during your Phd thesis. I could always count on your advice and help - especially during the pregnancies. I do not only talk about handling Ethidium bromide and methanol for me, but about the confidence and your unique way of taking care and feeling responsible. You also took the big effort to correct even the smallest orthographic, style and formatting detail in my thesis.

It was great to have people next door who helped to look "beyond the edge of the plate" during scientific discussions and onto the plate during lunch time. I think the best idea is to thank all people from AG Schnorrer and AG von Blume with a good-bye cake in the

kitchen - please remind me if I don't keep this promise. I also want to thank the people at the MPI of Biochemistry whose daily business it is to provide the administrative and logistic infrastructure to do science.

The last part of this acknowledgement is reserved for the people who enabled me to finish my thesis and take care of two small children at the same time. The financial support from the Christiane-Nüsslein-Volhard foundation and the aid of Prof. Reinhard Fässler and Dr. Carsten Grashoff ensured that I could continue experiments and lab work directly after the official maternity leave. Thanks to the optimal day-care at "Die Klopferspitzchen e.V." it was possible for me to continue working. I want to thank Serap Hanli for taking care of my younger daughter while I was finishing writing this thesis.

One of the most important people behind this project was my mother Sabine Kluger. Without her continuous help and support I would have finished my Phd thesis at least two years later - or maybe not at all. I also would like to thank Josef Kluger and the rest of my family for encouraging and supporting me to take this challenge. During the last years, my friends were a source of great strength and I would especially like to thank my conference-babysitter Jennifer Heiß.

In the last sentence of my master thesis I expressed the hope, that Pablo Nahuel Dominguez would still be there to correct my Phd thesis - and there he is! Right here at my side, helping me to manage all small and big, scientific and non-scientific challenges of daily life and beyond. Two small persons joined us and fill our lifes with laughter, chaos and joy.

Franka and Katja - both of you worked with me in the lab long before you were born. Thank you for giving me company in the dark microscope room and while pipetting at the bench. I am really proud of both of you and it is no coincidence that Katja started to walk now, right at the moment when it is also time for me to take the next step.

